



Small and High-Temperature Electrical Machine for Vehicle Applications

Roziah Aziz

**School of Electrical and Electronic Engineering
Newcastle University**

**A thesis submitted for the degree of
Doctor of Philosophy**

September 2020

Abstract

Interior permanent magnet (IPM) motors are a very promising design alternative in comparison with other types of electrical motors. Even though the price of rare-earth magnets has become a severe concern, IPM motors are gaining increasing attention due to their high torque density and excellent field weakening performance. Therefore, researchers have attempted to reduce the use of magnet materials but, at the same time, maintain the output performance of IPM motors. One solution is to reduce the size of the machine, which will also reduce the amounts of all materials used. Generally, a small scale is a profound advantage. Still, it may constitute a deficiency from the thermal point of view by contributing to higher loss density and problems operating at a higher temperature. An IPM motor may fail due to winding failure or the demagnetization of permanent magnets. It is crucial to make sure that these motors can run safely.

The purpose of this study is to develop a new electrical machine for automotive applications that is smaller in size with minimised use of magnets and which meets all requirements. The focus is on design alterations to reduce the size of the motor. Furthermore, high-temperature materials are used to ensure that the motor can work safely, even in hotter conditions.

A comparison is conducted on the performance of different sizes of the motor using finite element analysis in attempting to reduce the usage of the magnet material. Then, the temperature and heat transfer exposure of IPM motors are predicted by applying thermal modelling. Research is also conducted to find the most suitable material for smaller IPM motors to run at higher temperatures. Besides using neodymium-iron-boron as magnet material for an existing IPM motor, this study also analyses an IPM motor with samarium-cobalt, which has advantages in terms of higher temperature operation. The characteristics of IPM motors equipped with distributed and concentrated winding for automotive applications are also considered, and a proper motor winding is proposed. Two prototype IPM motors with different sizes and magnet materials are built and tested to validate the finite element analysis results. The first machine is developed using the same materials as in the existing Nissan Leaf machine, while the second is designed using high-temperature materials.

The most suitable size of a smaller IPM motor is ultimately determined, which can reduce the usage of permanent magnet and other material, but which maintains the output

performance of existing IPM motors. The design allows significant weight and size reductions in comparison with existing PM motors due to the use of high-temperature materials, which makes this electrical motor the right candidate for traction drive applications. The motor also satisfies all safety requirements.

Acknowledgements

I am very thankful to God for His grace and blessing gave me for the successful completion of my PhD studies.

I would like to express my sincere gratitude to my supervisor, Dr Glynn J Atkinson, for all his kindness, encouragement, and guidance throughout my PhD journey. Many thanks to technicians and friends, especially Jack, Tahany, Sanaa, Iago, Dave, and Pedros, in PEDM.

I would like to say thanks to my parents; Aziz, and Rogayah, my siblings; Rozana, and Hafeni, for their support.

Finally, I would like to give my heartfelt gratitude to my husband and kids, Shahrizal, Balqish, Arryan, and Luth Fareeq. Thank you for being there when I need someone and sacrifice a lot of things.

Table of Contents

Abstract.....	iii
Acknowledgments	v
Table of Content	vi
List of Figures	x
List of Tables	xiv
Acronyms and Symbols.....	xvi
Chapter 1 Introduction.....	1
1.1 Background	1
1.2 Statement of the problem	4
1.3 Objectives and scope of the thesis.....	6
1.4 Methodology	7
1.5 Outline of the Thesis	8
1.6 Contribution to knowledge.....	9
1.7 List of Publications.....	10
Chapter 2 Literature Review	11
2.1 Electric Machines	12
2.2 Electric Motors.....	14
2.3 Electric Motors for Electrical Vehicles (EVs)	15
2.4 Permanent Magnet (PM) Synchronous Motors.....	19
2.4.1 Interior Permanent Magnet (IPM) Motor Topologies	20
2.4.2 The Nissan LEAF.....	253
2.4.3 Stator Winding Topologies	25
2.5 Permanent Magnet Materials and Characteristics	27
2.5.1 Price of rare-earth magnet.....	30
2.5.2 B-H Loop and Demagnetisation Characteristics	31
2.6 Torque Production.....	33
2.7 Losses and Efficiency.....	36
2.8 High-Temperature Machine and Its Applications.....	39
2.8.1 Principle operation of switched reluctance motor (SRM).....	40
2.9 Thermal Analysis	43
2.9.1 Heat Transfer.....	45

2.9.2	<i>Conduction Heat Transfer</i>	46
2.9.3	<i>Convection Heat Transfer</i>	47
2.9.4	<i>Radiation Heat Transfer</i>	49
2.10	Cooling Methods	50
2.11	Summary	52
Chapter 3 Thermal Modelling		54
3.1	Lumped Parameter Thermal Model	55
3.1.1	<i>Conduction Resistances</i>	55
3.1.2	<i>Lumped Parameter with MotorCAD</i>	56
3.2	Finite Element Analysis Thermal Model	58
3.2.1	<i>3D Transient Magnetic Analysis</i>	61
3.2.2	<i>Transient thermal analysis</i>	65
3.2.3	<i>Convection heat transfer coefficient at the motor outer surface</i>	65
3.2.4	<i>Convection heat transfer coefficient in the air gap</i>	66
3.3	Summary	67
Chapter 4 Analysis of Motor Performance		69
4.1	Design Methodology	70
4.2	The Nissan LEAF	72
4.3	Proposed Motor Parameters and Characteristics	74
4.4	Electromagnetic Performance	75
4.4.1	<i>Magneto-motive Force (MMF)</i>	75
4.4.2	<i>Flux Linkage and Magnetic Flux Density</i>	77
4.4.3	<i>Cogging Torque</i>	79
4.4.4	<i>Back EMF</i>	80
4.4.5	<i>Torque Vs Armature current density, J_A</i>	81
4.4.6	<i>Magnet Mass</i>	82
4.5	Thermal analysis on Motor A	83
4.6	IPM Motor Adopted Concentrated Winding	85
4.6.1	<i>Slot dimensions</i>	86
4.6.2	<i>Winding Layout and Connection</i>	87
4.6.3	<i>Back EMF</i>	87
4.6.4	<i>Cogging Torque</i>	89
4.6.5	<i>Load Test Comparison</i>	90
4.6.6	<i>Peak electromagnetic torque with different current densities</i>	92

4.6.7	<i>Flux Linkage and flux distribution.....</i>	92
4.6.8	<i>Torque and Power vs. Speed at Various Armature Current Density, JA ...</i>	94
4.7	Summary	96
Chapter 5 Development and Optimisation of a Smaller Machine Running at Higher Temperature		97
5.1	Introduction	97
5.2	Alternative higher temperature materials	98
5.2.1	<i>Rotor and stator lamination.....</i>	98
5.2.2	<i>Permanent Magnets</i>	99
5.2.3	<i>Coils insulation</i>	103
5.3	Comparative study of the IPM motors	106
5.3.1	<i>Samarium Cobalt as permanent magnets</i>	106
5.3.2	<i>Effect of using different rotor and stator laminations</i>	108
5.3.5	<i>Thermal analysis on motor C with Hiperco50</i>	111
5.4	Cogging torque reduction.....	113
5.5	Material cost.....	116
5.6	Summary	117
Chapter 6 Machine Construction and Test Rig Description		118
6.1	Introduction	118
6.2	Stator construction.....	120
6.3	Rotor Construction	121
6.3.1	<i>Permanent Magnet Materials</i>	122
6.4	Windings	123
6.4.1	<i>Insulation life expectancy</i>	124
6.4.2	<i>Thermocouple</i>	125
6.5	Water cooling jacket.....	126
6.6	Test rig description.....	127
6.7	Summary	129
Chapter 7 Testing and Performance Analysis of Prototype Machines		130
7.1	Static at no load	130
7.2	Static torque for the machine I	133
7.3	Static torque for the machine II.....	137
7.4	Thermal characteristics	140
7.4.1	<i>Thermal behaviour of machine I</i>	142

7.4.2 <i>Thermal behaviour for machine II</i>	144
7.5 Summary	147
Chapter 8 Conclusions and Recommendations for Future Research	148
8.1 Effects of size reduction	150
8.2 Effect with a different permanent magnet material.....	151
8.3 Effects of using different lamination materials	151
8.4 Effect of different winding configuration	152
8.5 Performance comparison of the prototype machines	152
8.6 Recommendations for future research.....	153
8.6.1 <i>Rotor and stator topologies</i>	153
8.6.2 <i>Possible Emerging High-Temperature Materials</i>	154
8.6.3 <i>Improve the cooling method</i>	154
References:	156
Appendix 1 PM machine drawings.....	161

List of Figures

Figure 1. 1 Different rotor topologies for permanent magnet motor [4].....	2
Figure 1. 2 General flow chart of the research.....	7
Figure 2. 1 Types of electric vehicles	11
Figure 2. 2 Electric machine as an energy converter [9].....	12
Figure 2. 3 Structure of an electric machines.....	12
Figure 2. 4 Classification of Electric Motor	14
Figure 2. 5 Typical performance of electrical motor in industrial applications (A), and desired output characteristics of electric motor in electric vehicles (B).....	15
Figure 2. 6 Equivalent circuit for interior PM motor: (a) d-axis equivalent circuit; (b) q-axis equivalent circuit [4]	21
Figure 2. 7 Different types of IPM motors: a) V-shape , b) double magnet shape and c) delta shape with a bar magnet in V shape.....	23
Figure 2. 8 Feature of Nissan LEAF 2010	23
Figure 2. 9 Distributed winding stator	25
Figure 2. 10 Concentrated winding stator	26
Figure 2. 11 Magnet characterisation B-H curve for NdFeB [47]	32
Figure 2. 12 Magnet characterisation B-H curve for SmCo [48].....	32
Figure 2. 13 Torque at load condition.....	35
Figure 2. 14 The SRM structure [61]	40
Figure 2. 15 Housing jacket cooling type rotor [62].....	41
Figure 3. 1 Axial Section of the IPM Machine	57
Figure 3. 2 Schematic circuit	57
Figure 3. 3 Flow chart for 3D transient magnetic analysis	59
Figure 3. 4 Flow chart for transient thermal analysis.....	60
Figure 3. 5 3D IPM motor.....	61
Figure 3. 6 2D winding configuration: (a) Phase U, (b) Phase V, and (c) Phase W	62
Figure 3. 7 3D distributed winding coil geometry	62
Figure 3. 8 Current flow direction for each coil; (a) Phase U, (b) Phase V, and	63
Figure 3. 9 Mesh element for the motor.....	64
Figure 3. 10 Heat transfer circuit diagram	65
Figure 3. 11 Heat transfer rotor to air	65

Figure 3. 12 Heat transfer stator to air	66
Figure 3. 13 Heat transfer coil to air	66
Figure 3. 14 Heat transfer rotor to air gap.....	67
Figure 3. 15 Heat transfer stator to air gap	67
Figure 4. 1 Flow chart of motor design.....	71
Figure 4. 2 Nissan LEAF	73
Figure 4. 3 Different sizes of IPM motor.....	74
Figure 4. 4 Circuit current for each IPM motor	76
Figure 4. 5 Flux linkage for motor A.....	77
Figure 4. 6 Magnetic Flux density: (a) Motor A, and (b) Motor B.....	78
Figure 4. 7 Magnetic Flux density for motor C	78
Figure 4. 8 Cogging torque for each IPM motor: (a) Motor A, (b) Motor B, and (c) Motor.....	79
Figure 4. 9 No-load back-EMF: (a) Motor A, (b) Motor B, and (c) Motor C	80
Figure 4. 10 Torque for various J_A for Motor A and B.....	81
Figure 4. 11 Torque at various J_A for Motor C	81
Figure 4. 12 Rotor topologies of IPM machines.....	82
Figure 4. 13 Losses for IPM motors	84
Figure 4. 14 Temperature variations in Motor A.	84
Figure 4. 15 FEA configurations CW IPM motors (8 poles 12 slots): (a) open slots; b) semi- opened slots.....	85
Figure 4. 16 Slot dimension for (a) open slot CW IPM motor and (b) semi-closed CW IPM motor	86
Figure 4. 17 Winding Layout for CW IPM motor phase 1 (U)	87
Figure 4. 18 Back EMF for open slot CW IPM Motor	88
Figure 4. 19 Back EMF for semi-closed slot CW IPM motor	88
Figure 4. 20 Waveform of cogging torque for the open slot CW IPM motor.....	89
Figure 4. 21 Waveform of cogging torque for the semi-closed slot CW IPM motor	90
Figure 4. 22 Various current density, J_A for CW open slot IPM motor	91
Figure 4. 23 Various current density, J_A for CW semi closed slot IPM motor	91
Figure 4. 24 Torque at various J_A	92
Figure 4. 25 Flux density distribution for distributed winding machine.....	93
Figure 4. 26 Flux density distribution for concentrated open slot winding machine.....	93
Figure 4. 27 Flux density distribution for concentrated semi-closed winding machine	94

Figure 4. 28 Torque speed graph open slot CW IPM motor	95
Figure 4. 29 Torque speed graph semi closed slot CW IPM motor	95
Figure 5. 1 Flux density: (a) Motor A + NdFeB, (b) Motor A + SmCo	101
Figure 5. 2 Coil flux linkage for the motor with NdFeB	101
Figure 5. 3 Coil flux linkage for IPM motor with SmCo.....	102
Figure 5. 4 Electromagnetic torque comparison with the various value of J_A	102
Figure 5. 5 Magnet characterisation B-H curve for SmCo[48].....	103
Figure 5. 6 End-winding temperatures for Motor A, B and C	106
Figure 5. 7 Permanent magnets in IPM motor	106
Figure 5. 8 Magnet mass of permanent magnets.....	107
Figure 5. 9 Cogging torque: (a) Motor A with NdFeB, (b) Motor A with SmCo.....	107
Figure 5. 10 Torque for various J_A	108
Figure 5. 11 Flux line : (a) Motor C with M270-35A, (b) Motor C with Hiperco50.....	109
Figure 5. 12 Magnetic flux density: (a) Motor C with M270-35A, (b) Motor C with Hiperco50.....	109
Figure 5. 13 Cogging torque: (a) Motor C with M270-35A, (b) Motor C with Hiperco50	110
Figure 5. 14 Location of the probes	111
Figure 5. 15 Temperature variations in motor C with Hiperco50.....	111
Figure 5. 16 Temperature variations in motor C.....	112
Figure 5. 17 Magnetic flux density in motor C with Hiperco50.....	112
Figure 5. 18 Slot opening width for motor C.....	113
Figure 5. 19 New slot opening width.....	114
Figure 5. 20 Back EMF waveform: (a) before the slot opening width modification, (b) after the slot opening width modification	114
Figure 5. 21 The cogging torque after the slot opening width modification.....	115
Figure 5. 22 Torque value with various J_A	115
Figure 5. 23 Torque and power versus speed.....	116
Figure 6. 1 Stator construction.....	120
Figure 6. 2 Rotor with shaft	121
Figure 6. 3 Permanent magnets: (a) N42UH, (b) $\text{Sm}_2\text{Co}_{17}$	122
Figure 6. 4 Winding diagram	123
Figure 6. 5 Stator winding for motor I.....	124
Figure 6. 6 Nomex type 410	125
Figure 6. 7 Location of thermocouple sensor	125

Figure 6. 8 Water Jacket	126
Figure 6. 9 Test rig.....	127
Figure 6. 10 Full test rig of static torque test	128
Figure 6. 11 Digital flow meter.....	129
Figure 6. 12 Test rig for thermal testing	129
Figure 7. 1: (a) Inductance, L_q for machine I and II, (b) Inductance, L_d for machine I and II ...	132
Figure 7. 2 Connection of the power supply to the winding	133
Figure 7. 3 Static torque for machine I (FEA)	134
Figure 7. 4 Static torque for machine I (measured)	134
Figure 7. 5 Maximum torque for machine I at electrical angle 32°	135
Figure 7. 6 Static torque for machine I at 14A DC current.....	136
Figure 7. 7 Static torque for machine II	138
Figure 7. 8 Temperature rise for machine II without coolant	141
Figure 7. 9 Temperature rise for machine II with coolant	141
Figure 7. 10 Temperature at end-winding for machine I	142
Figure 7. 11 Effect of pumping different flow rate of water coolant	143
Figure 7. 12 Temperature at end-winding for machine I with water coolant.....	143
Figure 7. 13 Predicted temperature rise for a current of 7 amps (FEA).....	143
Figure 7. 14 Temperature rise at end-winding for machine II	144
Figure 7. 15 Temperature rise at the end-winding for machine B at 12.5 amps	145
Figure 7. 16 Simulation results for machine II	145
Figure 7. 17 Cool down temperature at the end-winding for machine II.....	147

List of Tables

Table 2. 1 List of electric vehicles model	16
Table 2. 2 Difference between SPM and IPM motors	20
Table 2. 3 Specifications of Nissan LEAF (2010) [15]	24
Table 2. 4 Characteristics of Permanent Magnet Materials [41]	29
Table 2. 5 The PM flux density.....	33
Table 2. 6 Materials used	42
Table 2. 7 Types of thermal model	44
Table 2. 8 Thermal Conductivity	46
Table 2. 9 Typical values of the convection heat transfer coefficient.....	48
Table 2. 10 Physical properties of fluids [76]	52
Table 3. 1 Material Properties [79].....	56
Table 3. 2 Element size for each part of the motor	64
Table 4. 2 Specifications of Nissan LEAF.....	72
Table 4. 3 Motor topology and major dimensions	73
Table 4. 4 Parameters of the IPM motors	75
Table 4. 5 Number of turns for each IPM motor	76
Table 4. 6 Dimensions of permanent magnets (NdFeB).....	83
Table 4. 7 Parameters of the CW IPM Motors	85
Table 4. 8 Slots Dimensions	86
Table 5. 1 Material used for Nissan LEAF	97
Table 5. 2 Material Properties of Hiperco50.....	99
Table 5. 3 Material properties of permanent magnet	100
Table 5. 4 Maximum Temperature Rise, $\Delta\theta$, for different winding classes [83].....	104
Table 5. 5 List of wires with ranges of temperature	105
Table 5. 6 Cost of permanent magnet	116
Table 6. 1 Main Parameters of Prototype Motors	118
Table 6. 2 Materials Used for Prototype Motors	119
Table 6. 3 Material Properties.....	119
Table 6. 4 Dimensions of the permanent magnets	123
Table 7. 1 Predicted and measured resistance values in different phases	131
Table 7. 2 Torque value for machine I.....	135
Table 7. 3 Torque value for machine II	137

Table 7. 4 Torque value for both machines	139
---	-----

Acronyms and Symbols

EV	Electric vehicles	BLDC	Brushless Direct Current
MMF	Magnetomotive force	CAD	Computer-Aided Design
SPP	Slot per pole per phase	PM	Permanent Magnet
EMF	Electromotive force	IM	Induction machines
FE	Finite element	SRM	Switch reluctance machine
HEV	Hybrid electric vehicles	AFM	Axial flux machines
PM	Permanent magnet	RFM	Radial flux machines
SPM	Surface permanent magnet	NdFeB	Neodymium-iron-boron
IPM	Interior permanent magnet	SmCo	Samarium Cobalt
kp	Pitch factor	d	diameter
kd	Distribution factor	σ	Electrical conductivity
kw	Winding factor	k	Thermal conductivity
m	Harmonic number	θ	Temperature rise
n	Coils per phase	J	Current density
α	Pitch angle, angle of road inclination	L	Inductance
δ	Distribution angle	Ψ	Flux linkage
β	Field weakening angle	i, I	Phase current
X_d, X_q	d- and q- axis inductance	Φ	flux
I_d, I_q	d- and q- axis current	N	Number of turns
V_d, V_q	d- and q- voltage	ω	Electrical angular speed
mv	Vehicle mass	R	Resistance
ρ	Density, resistivity	C	Capacitance
E	Electromotive force	T	Torque
H	Magnetic field strength	N_{slot}	Number of slots

μ permeability

B Flux density

l_a Axial Length

A Electric loading

*To my dearest husband, Shahrizal
my parents, Aziz and Rogayah
and my kids, Balqish, Arryan, and Luth.*

Chapter 1 Introduction

The electric vehicle is not a recent development but has been around for over 100 years. The first nation to develop such vehicles in the late 1800s were France and England. In 1895, Americans also began to devote attention to electric vehicles. Many innovations followed, and interest in motor vehicles increased considerably in the late 1890s and early 1900s.

Compared to gasoline vehicles, the maintenance requirements for electric vehicles are fewer. Therefore, maintenance costs are lower. The electric motor has only one moving part, the shaft, which is very reliable and requires little or no maintenance. The controller and charger are electronic devices with no moving parts, and require little or no maintenance. Not only are electric vehicles easier and cheaper to maintain, but they are also more efficient than gasoline engines and, therefore, more economical to operate. Electric vehicles use two types of electric motors to provide power to the wheels: direct current (DC) motor and the alternating current (AC) motors. Both types of electric motors have advantages and disadvantages. While the AC motor is less expensive and lighter in weight, the DC motor has a more straightforward controller, which lowers the cost of the DC motor/controller combination. The main disadvantage of the AC motor is the cost of the electronics package needed to convert (invert) DC from the battery into AC for the motor. However, with the advent of better and less expensive electronics, a large number of today's electric vehicles are using AC motors or controller systems because of the improvements in motor efficiency and lighter weight offered.

1.1 Background

Several types of motor drives are used in electric vehicles, such as induction motors, permanent magnet brushless AC motors, and permanent magnet brushless DC motors [1]. Electric motor drives for EV applications differ from those used in industrial applications. In the later, electric motor drives run at rated speed, whereas in EV applications, there are frequent start or stop processes along being used in different environments. The EV motor drive also has specific requirements to be fulfilled, such as high-power density, high instant power, and high torque when at low speed, when starting, and also for acceleration. The operating environments are also different. EV motor drives are usually installed in mobile vehicles, while industrial motor drives are generally located in fixed positions [2].

The most successful drives developed to fulfil the particular requirements of electric vehicles include Permanent Magnet Synchronous Motors (PMSMs) and Induction Motor (IM). Because of its characteristics such as high power density, high starting torque, and high cruising speed, the PMSM drive is becoming attractive for electrical vehicle (EV) applications. PMSMs are brushless and have permanent magnets instead of the field winding. By replacing the field winding of conventional synchronous motors with a permanent magnet, the PMSM eliminates conventional brushes, slip rings, and field losses. This type of motor includes six common topologies, surface-mounted, inset, spoke, single-barrier, multiple-barrier, and axially-laminated forms [3].

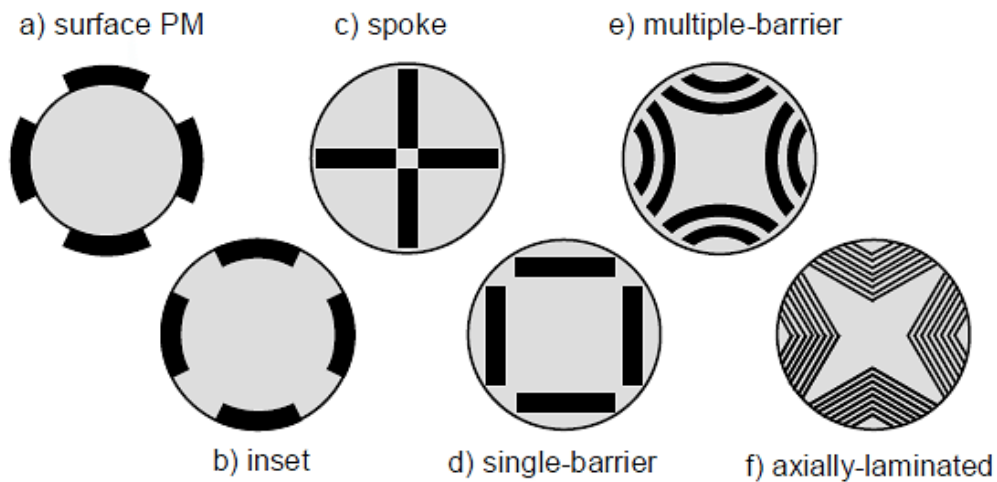


Figure 1. 1 Different rotor topologies for permanent magnet motor [4]

The PMSM has become a very popular choice of AC motor due to the following reasons [4];

- Lightweight because of the compactness and small size of the machine
- High power density
- High efficiency and power factor
- Larger torque inertia ratio
- Powerful overload capacity

The basic requirements for electric vehicles (EVs) are

- High power density.
- An extensive speed range with a constant power region.
- A fast torque response.
- High efficiency over a wide range with constant torque and constant power region.
- High efficiency for regenerative braking.
- Downsizing and weight reduction.
- Low moment of inertia
- High reliability and robustness for various vehicle operating conditions.
- Reasonable cost.
- Fault tolerance.
- Suppression of electromagnetic interference (EMI) from motor controllers.

It can be concluded that several factors have to be taken into account in the choice of an electric motor for EVs. These include efficiency, weight, cost, and the dynamic characteristics of motors, including high torque at low speed for starting and acceleration and high power at high-speed cruising, and the speed range under constant power will preferably be as comprehensive as possible.

.

1.2 Statement of the problem

An electric motor with high torque and power density is becoming increasingly popular, especially for high-performance applications such as electric vehicles and aerospace systems. Applying high current density in the stator winding and making the machine run at a higher speed can increase the power density. However, the higher current density in the stator winding results in significant copper losses and high hot-spot temperatures. The increase in copper and iron losses may, if the resulting heat is not adequately dissipated, causes the temperature to increase, which may be particularly problematic in parts of the machine that are difficult to cool down

PM motors containing rare-earth permanent magnets provide high power density and efficiency. However, the price of rare-earth magnet materials has increased substantially, which limits the practical use of these machines to high-performance applications that can deal with high material costs.

As is well known, field harmonics induce eddy current losses in the permanent magnet segments of the rotor. Since the rotor is a passive part of a thermal point of view, an accurate estimation of rotor losses is necessary to prevent the thermal demagnetization of the magnets. Interior permanent magnet (IPM) motors are an up-and-coming design alternative because of their better efficiency and power factors and utilisation in comparison to the other types of electrical motors. However, IPM motors have a much more complex rotor construction. It causes the appearance of additional constraints that can restrict the design of the motor, especially from the thermal and mechanical points of view. Therefore, the increasing temperature is a major factor threatening the magnetism of the magnets and the life and stability of PM motors because overheating can cause demagnetisation of the magnets and damage to the carbon-fibre sleeve. It is essential to model the heat transfer behaviour in PM motors accurately, at least to some degree, as this will define the cooling capability and, consequently, the nominal power of the motor.

The remnant flux density of the permanent magnet material depends on temperature. If the temperature of the permanent magnet exceeds the critical limit, it will affect the amplitude of the induced-back EMF and the performance characteristics of the machine. Thus, to ensure that the motor design has a long operational lifetime, it is necessary to focus on the thermal analysis

of the motor to be able to predict the accurate temperature distribution in the most sensitive parts of the machine. One of the problems in the development of large electric vehicles is their heavyweight, which leads to short driving distances.

Consistently, excessive temperatures will reduce the lifetime of the motor and may lead to severe failure. Thus, more studies focusing on electric machine manufacture aim to develop smaller motors. Besides, researchers are carrying out thermal analysis in parallel with the traditional electromagnetic and drive design [5]. Most existing electrical motors and actuators are not designed to survive in harsh, high-temperature environments. There is a need for such high-temperature motors in terrestrial applications as well as in power plants, launch vehicles, and furnace system components.

A smaller motor is considered to be an advantage in some respects, but this can be a disadvantage from the thermal point of view because the smaller size contributes to a higher loss density, and this makes the cooling of the machine more difficult. To create a design that will ensure the safe operation of a PM motor, the methods used for the thermal and mechanical analysis of the machine should be very reliable. The goal of this study is to predict the temperature and heat transfer behaviour in PM motors, which must be able to operate in hotter conditions but can still operate safely.

1.3 Objectives and scope of the thesis

The primary research objective is to develop a new electrical motor for automotive applications that is smaller in size with minimised use of magnets use and can run safely at a higher temperature. To achieve the primary research objective, the following purposes that have to be fulfilled are:

1. To construct and develop PM motors of different sizes that use less of magnet materials but give the output desired.
2. To analyse the effect of using two different types of permanent magnets: Neodymium-iron-boron and Samarium Cobalt.
3. To determine the output performance of using different types of rotor and stator lamination.
4. To compare the output performances between the existing machine with high-temperature materials machine.
5. To conduct experiments on prototype machines that have been developed to validate the simulation results to design an IPM motor with minimum magnet use and maximum torque that meets the requirements for automotive electrical applications.

1.4 Methodology

This research focuses on minimising the usage of permanent magnet material in permanent magnet synchronous motors with the desired torque value. Also, to make sure that smaller motors can run safely., The following steps are followed to achieve the design and validate the results:

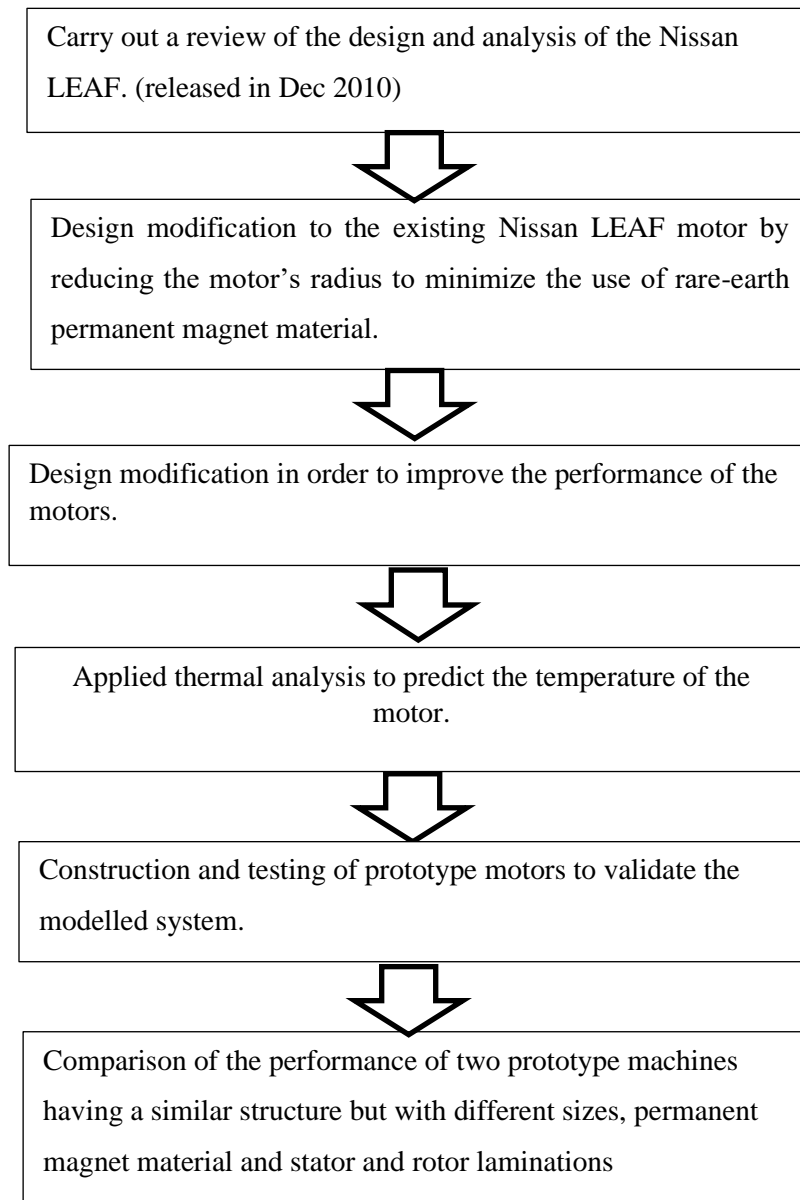


Figure 1. 2 General flow chart of the research

1.5 Outline of the Thesis

This thesis consists of eight chapters, with chapter one and chapter eight, the introduction and conclusion, respectively.

Chapter 2 is a literature review chapter presenting the details of IPM motors, the winding topologies and main specifications of IPM motors are also described. Besides, high-temperature machines, materials, and applications have also been discussed.

Chapter 3 presents the methodology used to analyse the thermal behaviour of the IPM motors. This thermal modelling method will be used to predict the temperature of essential parts of the machines.

Chapter 4 presents a comparison of motor configurations and the effect of reducing the size of the motor. Comparisons are also conducted with different types of permanent magnet material and rotor and stator lamination type. In this chapter, the electromagnetic performance of IPM motors is analysed. Two types of windings that can be used in IPM motors, which are either distributed or concentrated windings. Distributed winding is generally adopted as the winding configuration for IPM motors. Even the original Nissan LEAF motor adopted distributed winding. In this chapter, the same topologies of the rotor but with different types of winding and stator topologies are analysed.

Chapter 5 describes the effects of using a different type of permanent magnet in the IPM motor. The IPM motor also has been constructed with high-temperature materials, and the performance analysis has been analysed. Also, a thermal study of the designed machines is conducted. The optimization has been applied to the IPM motor to reduce the cogging torque.

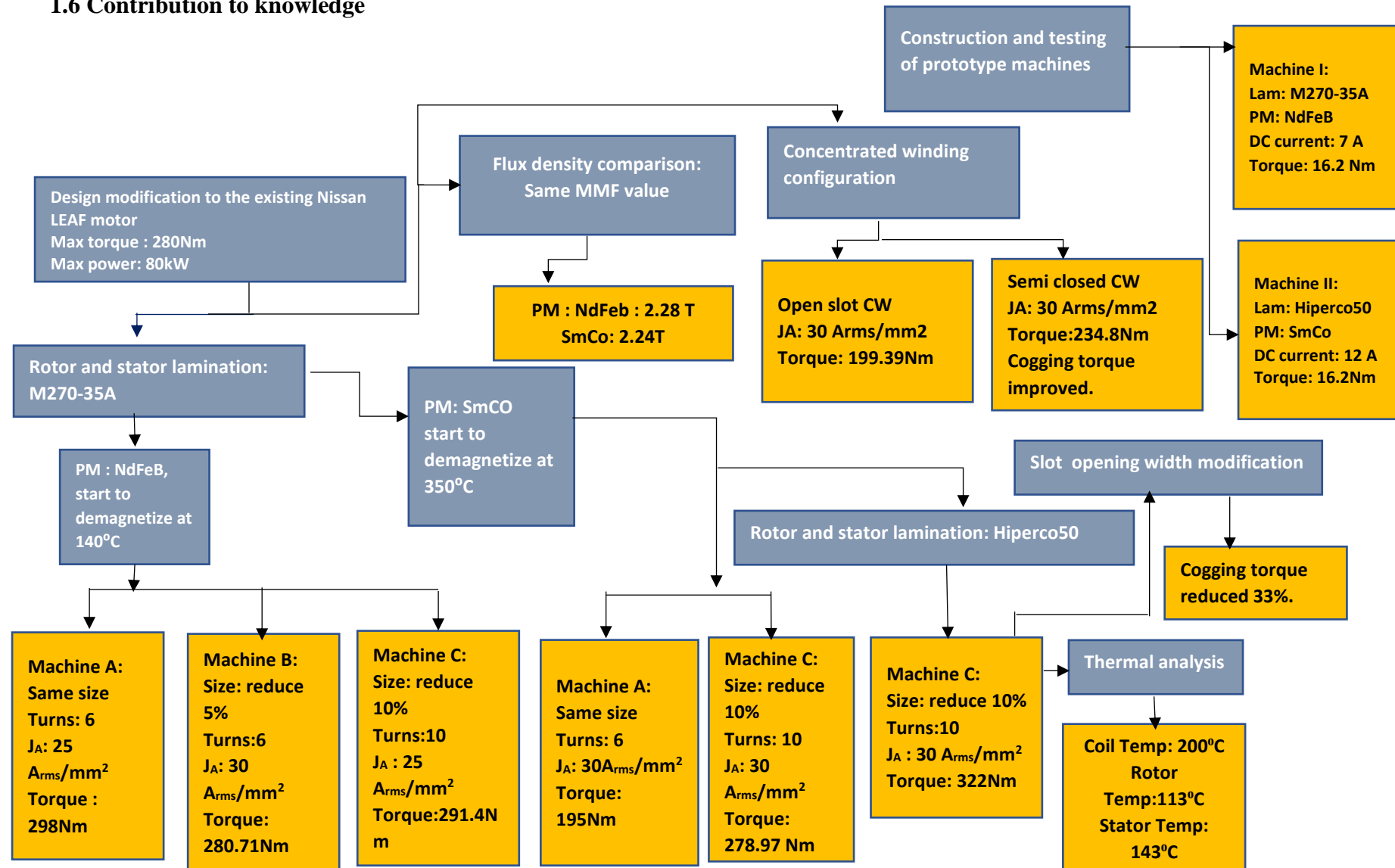
Chapter 6 describes the methods used in prototype construction. The materials used to achieve a high-performance IPM motor for electric vehicles have also been described here.

Chapter 7 focuses on the performance analysis of the prototype machines. Machine testing is conducted, and a comparison made between the simulation and experimental results.

Chapter 8 outlines the conclusions of this research work and recommendations for future studies.

.

1.6 Contribution to knowledge



1.7 List of Publications

The following publications have stemmed from this research:

- (1) R. Aziz, G.J. Atkinson. “Performance of Automotive Permanent Magnet Machines with Different Sizes, Rare-earth Magnets and Winding Configuration.” In: IEEE 15th International Conference on Environment and Electrical Engineering, Rome, 10-13 June 2015.
- (2) R. Aziz, G.J. Atkinson, “Maximised Torque and Minimised Magnet Use in Permanent Magnet Machines for Automotive Applications.” In IEEE WEMDCD 2015, Torino Italy, 26-27 March 2015.
- (3) R. Aziz, G.J. Atkinson, N.H.M. Radzi, S. Salimin, “Smaller High Temperature Machine for Electric Vehicle Application.” In CEAT 2016, Kuala Lumpur, Malaysia, 14-15 November 2016.
- (4) R. Aziz, G.J. Atkinson, S. Salimin, “Thermal Modelling for Permanent Magnet Synchronous Machine (PMSM)” International Journal of Power Electronics and Drive System (Ijpeds), UTHM, 8, 4, UTHM, 1903-1912, ISSN:20888694 (2017).

Chapter 2 Literature Review

Three main types of electric vehicles (EVs) are shown in Figure 2.1. Both hybrid electric vehicles (HEVs) and plug-in electric vehicles (PHEVs) are powered by petrol and electricity. HEVs generate the electrical energy to recharge the battery by using the car's braking system. Meanwhile, PHEVs can charge the battery through both regenerative braking and plugging into an external electrical charging outlet. Battery electric vehicles (BEVs) also use an external charging outlet to charge the battery. Even though BEVs have a short driving range and low speed, BEVs offer several advantages, which are environmentally friendly vehicles and low maintenance. High efficiency and high performance are the main characteristics needed to develop an electric vehicle system [1, 2, 6-8].

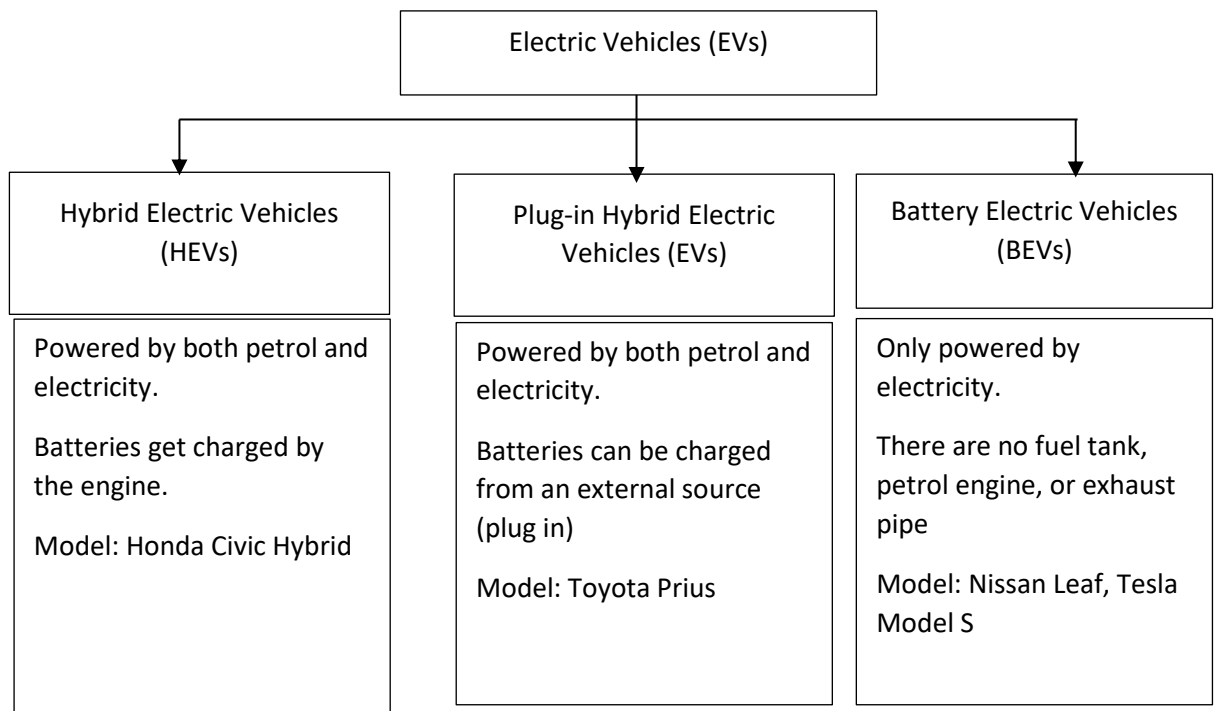


Figure 2. 1 Types of electric vehicles

2.1 Electric Machines

Electric machines, similar to motors, convert electrical power input into mechanical output, as shown in Figure 2.2. Generally, this type of device is operated as a motor, but when it slows down, and the power flow is reversed, the machine will enter generating mode

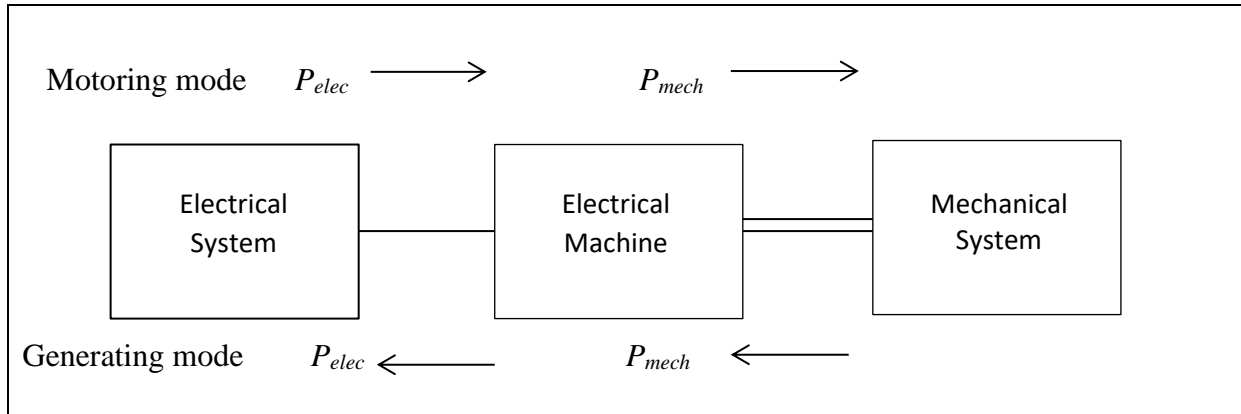


Figure 2. 2 Electric machines as an energy converter [9]

Figure 2.3 shows the structure of an electric machine. The stationary part is called the stator, and the rotating part is called the rotor. The fixed and rotating components are separated by an air gap, thereby allowing the rotor to rotate freely on a shaft supporting by bearings. The stator is firmly affixed to a foundation to prevent it from turning.

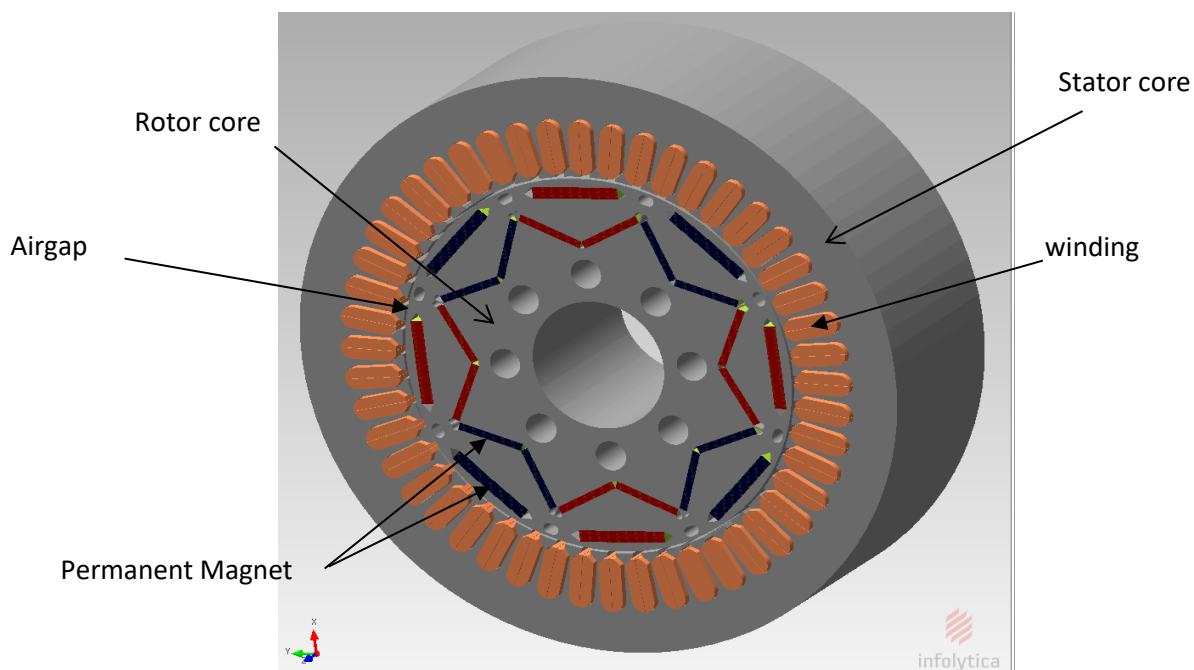


Figure 2. 3 Structure of electric machines

The stator produces a flux distribution where the field distribution corresponds to a combination of north and south poles. Machines with uniform magnetic reluctance in the path of flux lines crossing the air gap structures are called non-salient pole machines. However, some machines are designed as saliency machines so that the magnetic reluctance is unequal along various paths, thus producing reluctance torque.

There are two ways to govern the electric machine's operation for converting energy into mechanical work. Either an electromotive force (EMF) is induced in a conductor moving in a magnetic field, or a force is produced on a current-carrying inductor when it is subjected to an externally-established magnetic field. A conductor with length l is carrying a current i and subjected to an externally-established magnetic field of a uniform flux density B perpendicular to the conductor length. A force f_{em} is applied to the conductor due to the electromagnetic interaction between the external magnetic field and the conductor current. The magnitude of this electromagnetic force is given as:

$$A = \pi r^2 \quad (2.1)$$

$$f_{em} = Bil \text{ (Nm)} \quad (2.1)$$

Where B is the flux density (T), i is the current through the conductor (A), and l is the length of the conductor (m).

Induced EMF occurs when the coils in the stator experience a change of flux linkage caused by the moving magnet. The waveform in the induced EMF is very dependent on the waveform of the flux linkage. The product of the flux in the air gap and the number of turns associated with the flux lines will produce the flux linkage.

The root mean square (RMS) value of the induced EMF is given by:

$$E_{rms} = \frac{2\pi T_{ph} \phi_m f_r}{\sqrt{2}} = 4.44 T_{ph} \phi_m f_r \quad (2.2)$$

Where f_r is the frequency of the EMF or rotational frequency, T_{ph} is the number of turns per phase, and ϕ_m is the peak mutual flux.

2.2 Electric Motors

Alternating current (AC) and direct current (DC) motors are two main types of electric motors. An AC motor is driven by alternating current as input, whereas a DC motor takes direct current. AC motors may be a single-phase or three phases, which are mainly classified into induction motors, synchronous motors, flux switching motors, and switched reluctance motors. The essential parts of an AC motor are the stator and rotor. A stator is the stationary part of the motor, whereas a rotor is the rotating part of the motor.

In the industry, especially for bulk power conversion from electrical to mechanical, the three-phase AC motors are mostly applied. Meanwhile, single-phase AC motor are primarily used in domestic appliances such as fans, washing machine, and mixer. There are various types of electric motors used in electric vehicles. The classification for an electric motor, as illustrated in figure 2.4. It is crucial to select the appropriate electric vehicle motor based on the requirements of the motor performance. For high power applications, the ideal motor choice would be permanent magnet synchronous motors or induction motors. The permanent magnet synchronous motors can be classified into surface permanent magnet motor and interior permanent magnet motor.

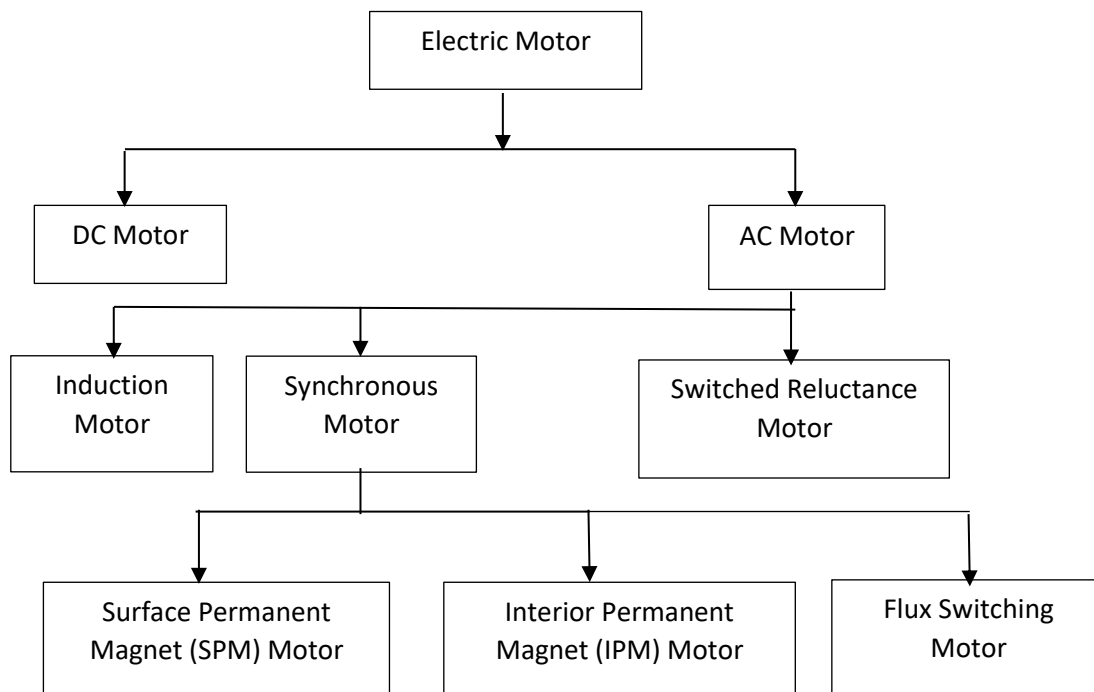


Figure 2. 4 Classification of Electric Motor

2.3 Electric Motors for Electrical Vehicles (EVs)

There are various types of electric motors in industrial applications. However, for electric vehicle applications, performance indexes have to be taken into accounts, such as efficiency, weight, cost, and dynamic characteristics [10]. Figure 2.5 shows the differences between the typical performance of an electric motor (A) and the desired output characteristics of electric motors in electric vehicle applications (B). Electric motors for electric vehicle applications need to exhibit high torque at low speed for starting and acceleration and high power and high speed for cruising. Besides, the speed range under constant power needs to be as comprehensive as possible.

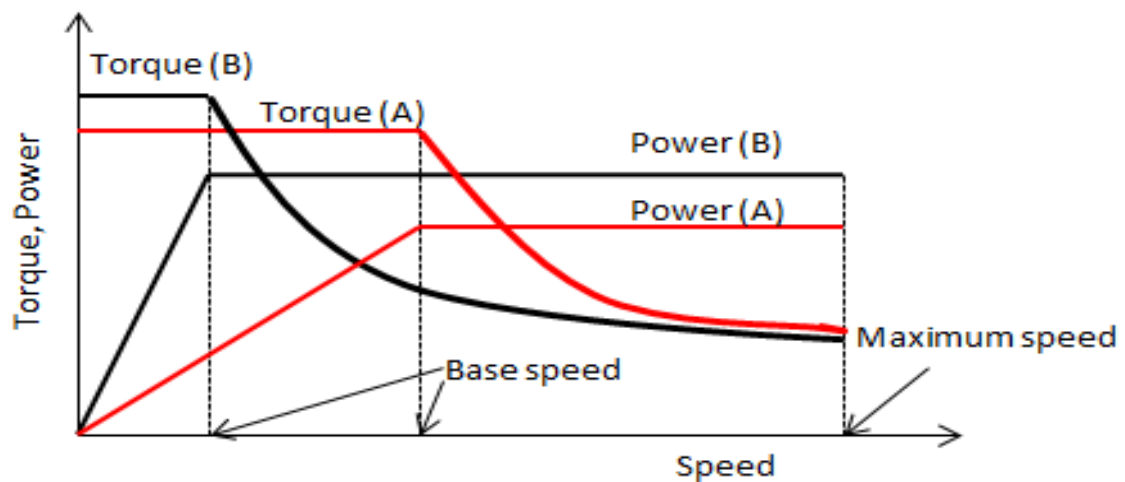


Figure 2. 5 Typical performance of electrical motor in industrial applications (A), and desired output characteristics of an electric motor in electric vehicles (B)

Madhavan and Fernandes (2010) proposed a three-phase, 12/8 pole axial synchronous switched reluctance motor (ASSRM) with a toroidal-type winding for electric vehicle applications. They found that an SRM has a simple, rugged construction with increased mechanical strength and a simplified manufacturing process. However, the segmented SRM with concentrated winding used to reduce the end winding length has poor magnetic utilisation, and an ASSRM with segmented rotors has the advantage of low noise [11]. As a result, the proposed machine has a short flux path at the aligned position, with a higher fault-tolerant capability because the windings are thermally and mechanically isolated from others, as well as a higher electrical loading. After all, the disc rotors naturally act as fans.

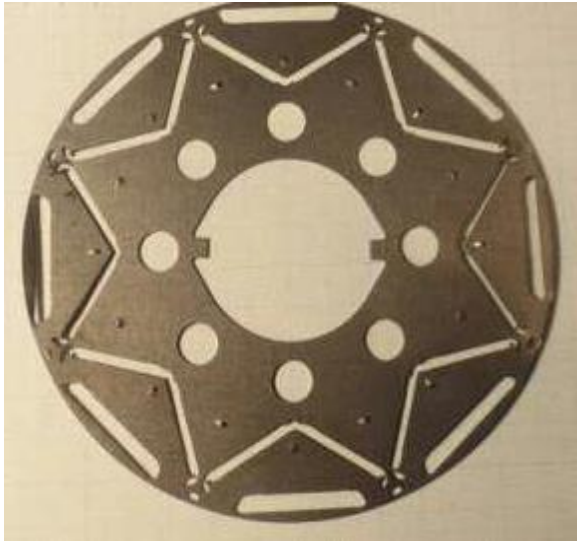
In research done by Xue et al. [10], four different types of motor drives for EVs were compared: a brushed DC motor, an induction motor, a permanent magnet (PM) brushless DC motor, and an SRM. As expected, in terms of efficiency, the PM brushless DC motor is the best choice.

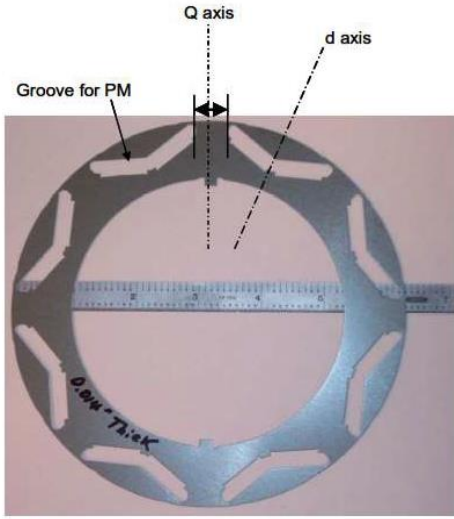

However, the SRM is lighter than others in terms of weight. Nevertheless, the PMSM has been successfully developed to fulfil the particular requirements of EVs [2, 4, 12-14].

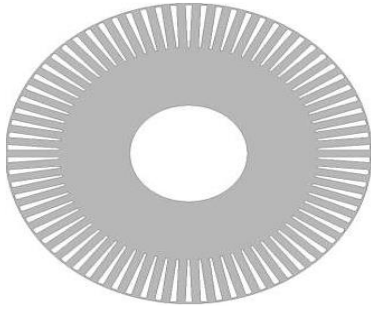

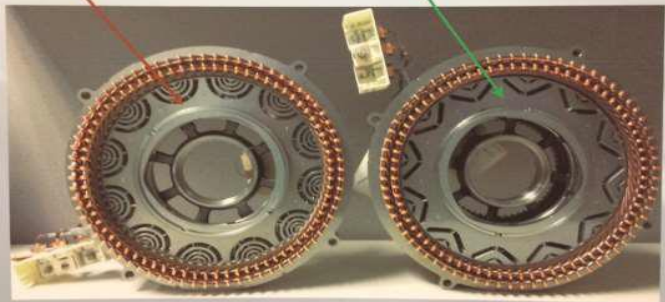
EVs are a dream for the human being, city traffic without exhaust gas and with low noise. PMSMs become the most preferred choice of AC motors in high-performance drive systems such as EVs.

Recently, there is more than 40 series production of highway-capable all-electric cars available in various countries. Nissan LEAF is the world's top-selling EVs among them, followed by Toyota Prius. Meanwhile, BMW i3 ranked third among all-electric cars sold worldwide. To overcome the problem of the high cost of rare earth magnets, Tesla Model S adopted a propulsion solution without rare earth PM. However, the starting current of an induction motor can be high and will affect battery duration. A list of EV models is presented in Table 2.1.

Table 2. 1 List of electric vehicles model

EV Model	Types of Machine	Rotor Topologies
Nissan LEAF 2010[15]	48 slots, eight poles interior permanent magnet synchronous machine	 <p>There are two magnet layers for each pole: a flat magnet and a V-magnet. Three circumferential channels in the housing act as a water jacket.</p>

EV Model	Types of Machine	Rotor Topologies
Toyota Prius 2004 Model	48-slots, 8-poles IPM machine	 <p>Toyota Prius only has one v-magnets layer</p>
BMW i3[16]	125 kW NdFeB IPM machine	 <p>BMW i3 is a B-class, high-roof hatchback manufactured and marketed by BMW. The car has an electric powertrain using rear-wheel drive via a single-speed transmission and an underfloor Li-ion battery pack with an optional range-extending gasoline engine.</p>

EV Model	Types of Machine	Rotor Topologies				
Tesla Model S [17]	60-slots, 4-poles, induction motor	<div></div> <p>Seventy-four rotor bars are fabricated on a copper-rotor induction motor.</p>				
Honda ACCORD 2005 Model[18]	24-slot, 16-pole IPM with flat magnets	<div></div>				
Chevrolet Volt	Two IPM machines have been used for this model. One is 50 kW ferrite, and the other is 100 kW NdFeB.	<div><p>GEN2 VOLT ELECTRIC MOTOR DRIVE UNIT</p><table><tr><td>Motor A</td><td><ul style="list-style-type: none">• 12 Pole Ferrite IPM• 50 kW• 11000 RPM</td><td>Motor B</td><td><ul style="list-style-type: none">• 12 Pole Dysprosium Diffused NdFeB IPM• 100 kW +• 12000 RPM</td></tr></table><div></div></div> <p>Chevrolet Volt is a plug-in hybrid car manufactured by General Motors. Both IPM machines are designed with different rotor topologies as well.</p>	Motor A	<ul style="list-style-type: none">• 12 Pole Ferrite IPM• 50 kW• 11000 RPM	Motor B	<ul style="list-style-type: none">• 12 Pole Dysprosium Diffused NdFeB IPM• 100 kW +• 12000 RPM
Motor A	<ul style="list-style-type: none">• 12 Pole Ferrite IPM• 50 kW• 11000 RPM	Motor B	<ul style="list-style-type: none">• 12 Pole Dysprosium Diffused NdFeB IPM• 100 kW +• 12000 RPM			

2.4 Permanent Magnet (PM) Synchronous Motors

In AC drives, there are primarily two types of motors: induction and PMSMs. Induction motors are typically used in industry, and PMSMs are mostly used for high-performance applications due to their capability of producing smooth torque. Both are supplied by three-phase AC voltage and current. The stators are similar and consist of three-phase winding; however, the rotor construction is different in these two machines. In the stator, each phase winding (which consists of several coils connected in series) produces a sinusoidal field distribution in the air gap[9].

A PMSM is a rotating electric machine in which the rotor has PMs either on the surface or internally, and the stator is similar to an induction motor, which is a classic three-phase type. In other words, a PMSM is equivalent to an induction motor where a PM works to produce a magnetic field in the air gap. Replacing the field winding of conventional synchronous motors with a PM can eliminate conventional brushes, slip-rings, and field losses [2]. Also, it can increase power density and efficiency.

PMSMs can achieve smooth torque. The rotor magnet generates stator and rotor flux that is used to define the torque value and the speed of the motor.

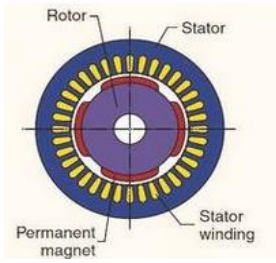
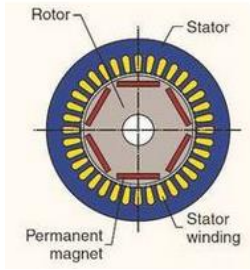
The use of PMs in the construction of electrical machines will give the following advantages [19] :

- No excitation losses because the field excitation absorbs no electrical energy.
- Increase efficiency.
- Higher torque.
- Higher output power.
- Better dynamic performance.
- Simplification of construction and maintenance.

There are two basic directions of field flux in a PMSM, either radial or axial direction [20-22]. For the radial field, the flux direction is along the radius of the machine, and the magnets can be placed in many positions on the rotor. Meanwhile, for the axial field, the flux direction is parallel to the rotor shaft [23].

Two main categories of PM machines are surface permanent magnet (SPM) motors and interior permanent magnet (IPM) motors. Table 2.2 shows the difference between an SPM and an IPM motor.

Table 2. 2 Difference between SPM and IPM motors

	SPM motor	IPM motor
Structure		
Permanent magnet	Permanent magnets are affixed to the exterior of the rotor surface	Permanent magnets are embedded into the rotor.
Mechanical strength	Lower mechanical strength due to mechanical mounting	Mechanically sound, and suitable for operating at very high speeds
Torque	Rely significantly on the magnet alignment torque component to produce torque	Able to generate torque by taking advantage of both magnet alignment and reluctance torque components of the motor

2.4.1 Interior Permanent Magnet (IPM) Motor Topologies

Various characteristics of permanent magnet motors have to be considered for traction applications, such as high efficiency, high power density, and extensive constant power operating range [3]. All these characteristics can be achieved using an IPM motor that produces PM torque from their magnet flux and reluctance torque from their rotor saliency. The number, thickness, and location of the rotor flux barriers control the reluctance torque of a motor. Meanwhile, by varying the magnetic flux density and the fraction of the rotor barriers that are filled with a magnetic material, the PM flux can be adjusted independently.

The equivalent circuit for the interior PM motor is shown in Figure 2.6.

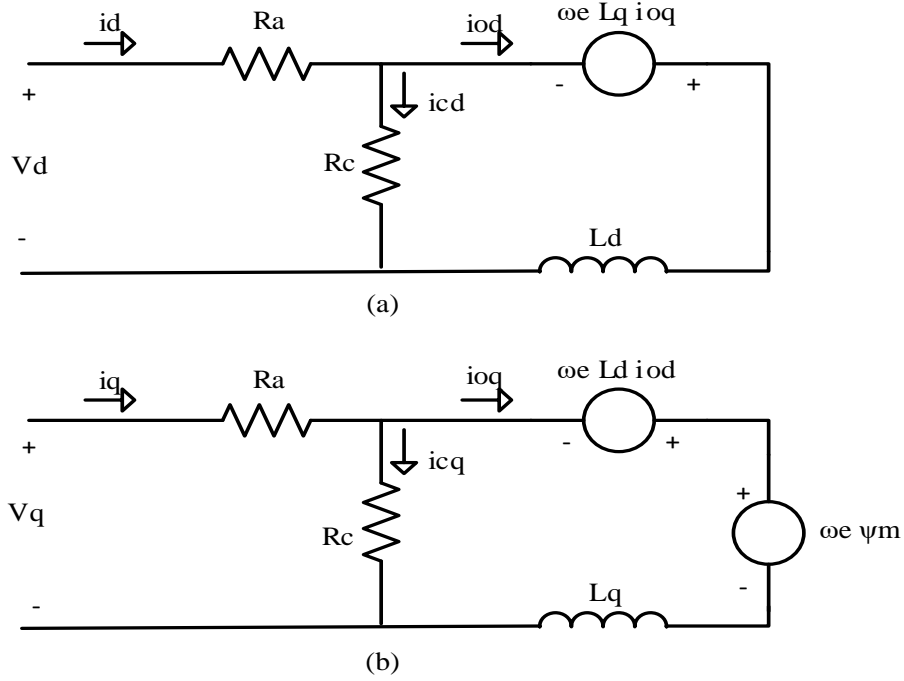


Figure 2. 6 Equivalent circuit for interior PM motor: (a) d-axis equivalent circuit; (b) q-axis equivalent circuit [4]

From the equivalent circuit parameters for the interior PM motor, the equation for d -axis voltage, V_d and q -axis voltage, V_q are,

$$V_q = R_a \cdot i_q + L_q \frac{di_q}{dt} + \omega_e \psi_m + \omega_e L_d i_d \quad (2.4)$$

$$V_d = R_a \cdot i_d + L_d \frac{di_d}{dt} - \omega_e L_q i_q \quad (2.5)$$

where ψ_m is the RMS phase magnet linkage, ω_e is the electrical frequency, and L_d and i_d are the d -axis inductance and current components respectively, while L_q and i_q are the q -axis inductance and current components, respectively.

The other three alternative equivalent circuit parameters are saliency ratio, ξ , characteristic current, I_x and peak back EMF, E_p .

The ratio of L_q over L_d will produce the saliency ratio as in the equation below:

$$\xi = L_d / L_q \quad (2.6)$$

The characteristic current, I_x is given as:

$$I_x = \psi_m / L_d \quad (2.7)$$

And the peak back-EMF equation is:

$$E_p = \sqrt{6} \omega_{em} \psi_m \quad (2.8)$$

where ω_{em} is the electrical frequency at the maximum speed.

By substituting those three alternative equivalent circuit parameters in equations 2.6 – 2.8 into the voltage equations 2.7 and 2.8, the equations can be defined as:

$$V_q = \frac{\omega_e}{\omega_{em}} \frac{E_p}{\sqrt{6}} \left[1 + \frac{i_d}{I_x} \right] \quad (2.9)$$

$$V_d = \frac{\omega_e}{\omega_{em}} \frac{E_p}{\sqrt{6}} \left[-\frac{\xi i_q}{I_x} \right] \quad (2.10)$$

Meanwhile, by using equations 2.12 and 2.13, the equation for output power, P , can be expressed as:

$$P = m(V_q i_q + V_d i_d) = \frac{\omega_e}{\omega_{em}} \frac{m E_p}{\sqrt{6}} i_q \left[1 + (1 - \xi) \frac{i_q}{I_x} \right] \quad (2.11)$$

where m is the number of phases.

Generally, the rotor topologies for an IPM motor are as shown in figure 2.7. The rotor of an IPM motor consists of a stack of metal laminations stamped with slots so that the stack forms a cavity parallel to the axis of the motor. The magnets fit into these slots, creating accurate alignment without the need for special tooling and retains the magnets even in the face of big shock, vibration, and centrifugal force. As mentioned previously, several EVs applied IPMSMs as their motors, such as Nissan LEAF, Toyota Prius, Chevrolet, and BMW i3.

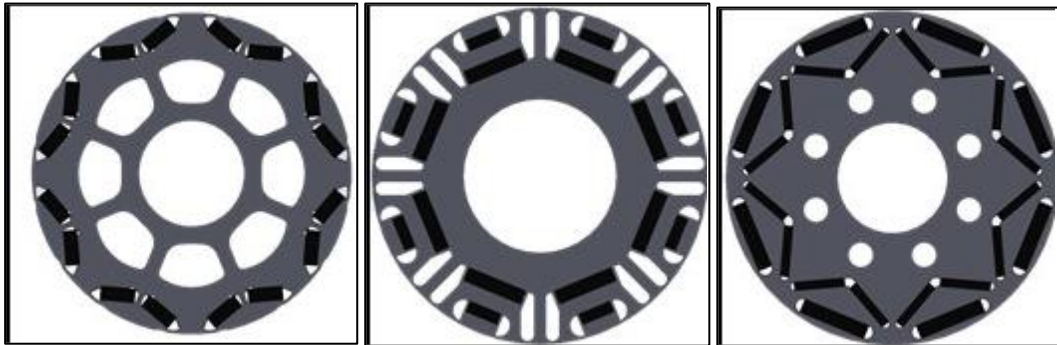


Figure 2. 7 Different types of IPM motors: a) V-shape, b) double magnet shape and c) delta shape with a bar magnet in V shape

2.4.2 The Nissan LEAF

The most popular IPM motors among researchers for EV applications are Nissan LEAF that was released in 2010. M270-35A is used for rotor and stator lamination material. Nissan LEAF needs 24 magnets for a complete machine, as shown in Figure 2.8. The type of magnet used is neodymium (NdFeb). Meanwhile, Table 2.3 shows the specifications of the Nissan LEAF.



Figure 2. 8 Feature of Nissan LEAF 2010

Table 2. 3 Specifications of Nissan LEAF (2010) [15]

Voltage	240-403V (dc voltage-inverter)	
Current amplitude	Max ac current = 425 Arms (4 sec) 340 Arms	Coolant temp = 65°C
Speed	Top motor speed = 10,390 rpm	
Torque	Max torque = 280Nm	For climbing steps 30% of grades
Cooling	Three cooling water channels are provided in parallel to ensure sufficient cooling performance.	
Temperature	Coolant temperature = 65°C	
Size	Electromagnetic steel sheet of less than 0.35mm	
Output	Maximum power = 80 kW	To facilitate effortless, high-speed cruising.
Winding connection	For stator, either distributed or concentrated. This motor drive adopts the distributed types, which offers advantages for the magnetic circuit.	
Weight	Approximately 58kg	
Housing	Made of cast aluminium and incorporates the water jacket for cooling the motor.	

Even though the PM motor has been widely used, the use of PMs has become a severe issue because their cost is steadily increasing. Therefore, the main objective of this study is to determine a smaller size PM machine that can maintain the level of electromagnetic performance, torque capability, and efficiency of the reference machine.

2.4.3 Stator Winding Topologies

There are two common stator winding topologies: the distributed winding stator and concentrated winding stator. The number of slots per pole per phase (SPP) characterizes these stator windings.

a) Distributed winding stator

This type of winding is widely used and has a relatively large number of slots per pole per phase, which is $SPP \geq 1$. The stator winding coils generally span more than one slot, and the stator has a relatively low ratio of leakage to magnetizing inductance, which allows high saliency ratios to be achieved.

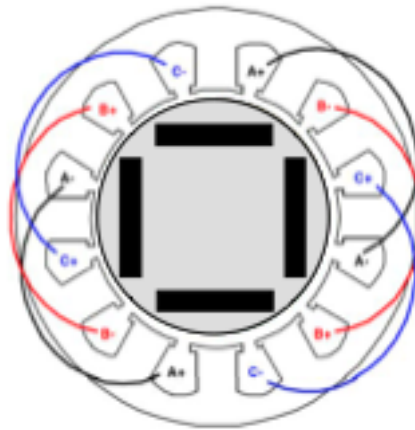


Figure 2. 9 Distributed winding stator

b) Concentrated winding stator

This type of winding has coils that are wrapped around individual teeth, and it offers significant advantages in manufacturing, achievable packing factor and thermal performance. Generally, they have values of $SPP < 0.5$. The stator also has the potential to achieve low torque ripple and is well-suited to deliver high torque density by using high pole numbers.

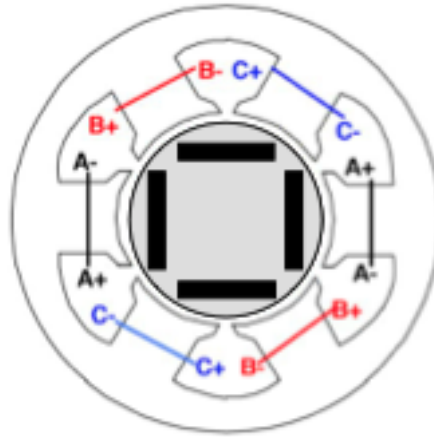


Figure 2. 10 Concentrated winding stator

In recent years there has been increasing interest in the use of concentrated winding stators for both interior and surface permanent magnet rotors. In comparison, the main advantage of concentrated winding is the shorter end winding, which will produce lower winding resistance. For a machine with applications which need wide speed ranges, the concentrated winding is a better choice because it can provide higher inductance values [24]. Nevertheless, the saliency ratio is lower for concentrated winding compared to distributed winding stators. Comparisons of distributed and concentrated windings in interior PMSMs have been conducted by many researchers [25-32].

Commonly, motors with distributed winding will have more slots than motors with a concentrated winding. Theoretically, a motor with concentrated winding will have a lower copper loss, but higher iron loss and magnet eddy current due to high armature field harmonic content. During motor testing, significant amounts of additional rotor power loss have been identified [24]. Thus, it can be concluded that the concentrated winding has higher inductance, and gives advantageous in improving field weakening, but provides lower peak power within a given inverter limit and a smaller saliency ratio compared to distributed winding. However, for

the low-speed surface-mounted type of PM machine, the concentrated winding is superior because the minimization of the copper volume reduces power loss and manufacturing costs [33].

2.5 Permanent Magnet Materials and Characteristics

Even though the use of PMs will increase the cost of an electrical machine, it is still preferable because the presence of PM will provide a free source of flux, which otherwise has to be created by current-carrying windings that incur i^2R losses in winding resistance. Permanent magnet machines can offer higher efficiency and power density.

Commonly, NdFeB is chosen as the permanent magnet material for the PM motor because it has the characteristic of the highest density to volume ratio. However, compared to other permanent magnets like ferrites and Alnicos, NdFeB can lose its magnetization more quickly [34]. In comparison with ferrites, there is an improvement in PM motors with NdFeB in terms of power density and torque density [35].

Nakamura, Yoshida, and Ichinokura (2009) [36] have presented a novel permanent magnet reluctance generator (PMRG) with ferrite magnets, which can reduce the cost materials by about 45%. They also proved that ferrite has almost the same output power as rare-earth magnets. Furthermore, by cutting off the rotor pole-tips and stacking two PMRGs, they were able to decrease the torque ripple.

Miura et al. (2010) [37] proposed a ferrite permanent magnet axial gap without rare earth material for HEV applications. The rotor of the proposed motor has a segmented structure composed of ferrite segments, and the soft magnetic composite (SMC) core segments arranged alternately. Even though the force and remanence flux density of ferrite magnets are much smaller than in rare earth magnets, the proposed motor is equipped with both excellent torque characteristics and good endurance of irreversible demagnetization in the ferrite PM.

Even among different grades of NdFeB, comparisons of performance have been conducted in terms of materials and the impact of temperature [38]. The five categories HS42EH, HS40FH, HS36EH, HS32GH, and HS35EH magnets, have been observed to provide the most suitable characteristics for interior PM motors. Each grade has different remanent flux density and

thermal characteristics. As a result, the HS43EH magnet has the highest remanent flux density and will produce the minimum iron losses and minimum torque ripple at all temperatures. On the other hand, in terms of cost and cogging effects, the HS35EH magnet is the better solution.

Demerdash and Nyamusa (1985) compared samarium-cobalt and strontium-ferrite in terms of their overload parameters and performance. Two equivalent 15 h.p brushless DC motor were investigated, one built with samarium cobalt and the other made with strontium-ferrite [39]. The samarium-cobalt machine was more able to absorb overload and more readily capable of carrying momentary overloads without danger of instability or excessive magnet flux reduction. Research by Pal (1993) found that, where demagnetisation is concerned, rare-earth magnets samarium and neodymium were vastly superior to any other magnet type available. Compared to samarium-cobalt, NdFeB magnets are more sensitive to variable temperature effects relating to the air gap. Besides, NdFeB magnets corrode and need special protection to avoid self-disintegration [40].

A study by Tariq et al. [41] compared permanent magnet materials to find those most suitable for the PMSM and especially for HEV applications. Table 2.4 below shows the characteristics of NdFeB, SmCo, AlNiCo, and ferrite permanent magnet material. For high-temperature applications, SmCo or ferrite magnets are the best options. The remanent flux density of NdFeB will decline at a faster rate with increases in temperature compared to SmCo. Ferrites can also be used as the magnet materials in PMSM. However, the ferrite PMSM will produce less flux density and have less power density [42]. Therefore, due to high B_r and H_c , NdFeB and SmCo are more suitable for high power density.

Table 2. 4 Characteristics of Permanent Magnet Materials [41]

Parameters	Neodymium-iron-boron	Samarium Cobalt	AlNiCo	Ferrite
Flux density, B_r (T)	0.7 – 1.41	0.55 – 1.15	0.7 – 1.35	0.22 – 0.42
Coercive force, H_c (kA/m)	310 - 1500	360 - 820	44 - 151	151 - 254
Energy product BH (kJ/m ³)	35 - 385	56 – 246	11.0 – 59.0	9.0 – 33.0
Permeability, μ_{rec}	1.05 – 1.25	1.02 – 1.1	1.5 - 4	1.05 – 1.35
Temperature, T_{opt} (°C)	100 - 200	200 - 550	200 - 500	100 - 250
Relative Cost	\$\$\$	\$\$\$\$	\$\$	\$

Therefore, for this research, two types of magnet materials are used: samarium-cobalt (SmCo) and neodymium-iron-boron (NdFeB). Both types of magnets are used in many ways and are the basic types of materials for rare earth magnets. Generally, SmCo can be used at higher temperatures (350 °C) compared to NdFeB, which needs to be used for lower temperature applications. However, it depends on the applications concerned. Higher H_{ci} materials of NdFeB can be used at the temperature as high as 200 °C and under 100 °C for low H_{ci} materials.

It is well known in the industry that the highest energy product room temperature magnet type, NdFeB, has weak temperature coefficients compared to those of SmCo. It means that there is a region around 125 °C where the BH_{max} value for NdFeB grades falls below that of SmCo compositions. Thus, it is clear that SmCo-based magnets represent the best choice of magnet for high-temperature applications [43].

Choosing SmCo as the magnetic material will give advantages in humid and high radiation environments. As SmCo does not require any surface treatment because it does not oxidise, it is very stable in radiation environments at higher grades because this type of magnet offers high resistance to corrosion. However, SmCo is not mechanically as strong as NdFeB because SmCo is more brittle, and in terms of cost, NdFeB is generally cheaper than SmCo. SmCo is the most

expensive magnetic material to manufacture and fabricate due to its high cobalt content and the brittle nature of the samarium alloy.

2.5.1 Price of rare-earth magnet

Due to the issues of the price of rare earth PM and their availability, thus the whole world needs to take proper actions. The cost of rare earth magnets increased dramatically in 2011, which forced some companies to find other alternatives. They developed alternative PMs, such as ceramic ferrite magnets. However, the magnetic strength is low, and a bigger size magnet and motor are produced[44].

Neodymium (Nd) is an ingredient of PMs used in EV motors, whereas dysprosium (Dy) is also one of the rare earth magnets with high demand that is added to improve the heat resistance of PM. China was the dominant source of supply during the crisis in 2011. Figure 2.11 shows the price of a rare earth magnet. The cost of Nd reached as high as 550 USD per kg, and for Dy, the price was 3,350 USD per kg in the current term. However, the cost of the PMs collapsed as predicted. In 2018, the prices stabilised at 70 USD per kg for Nd and 280 USD per kg for Dy. Although the prices now appear to have flatlined, market players remain worried that China might halt imports again.

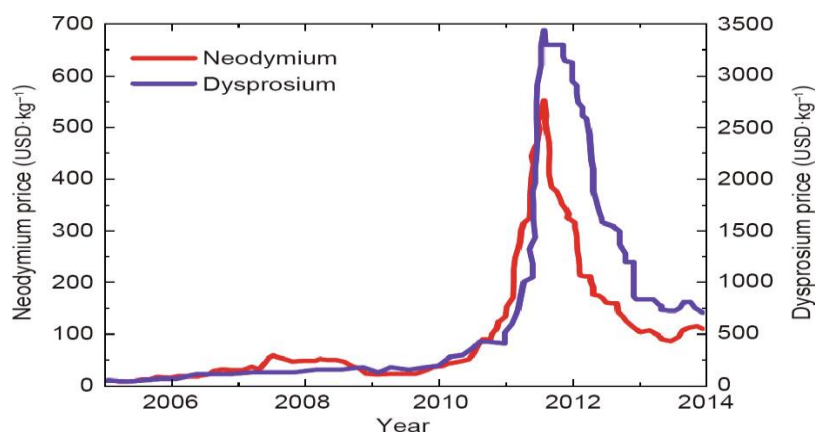


Figure 2.11: Price of the rare-earth magnet [45]

In the future, the price of rare earth magnets is predicted to increase significantly. Figure 2.12 shows the forecast of Nd price worldwide from 2009 to 2025. It is expected that the cost of neodymium oxide will reach 94,438 USD per metric ton in 2017. Until 2025, the price is expected to increase over 148,000 USD per metric ton [46].

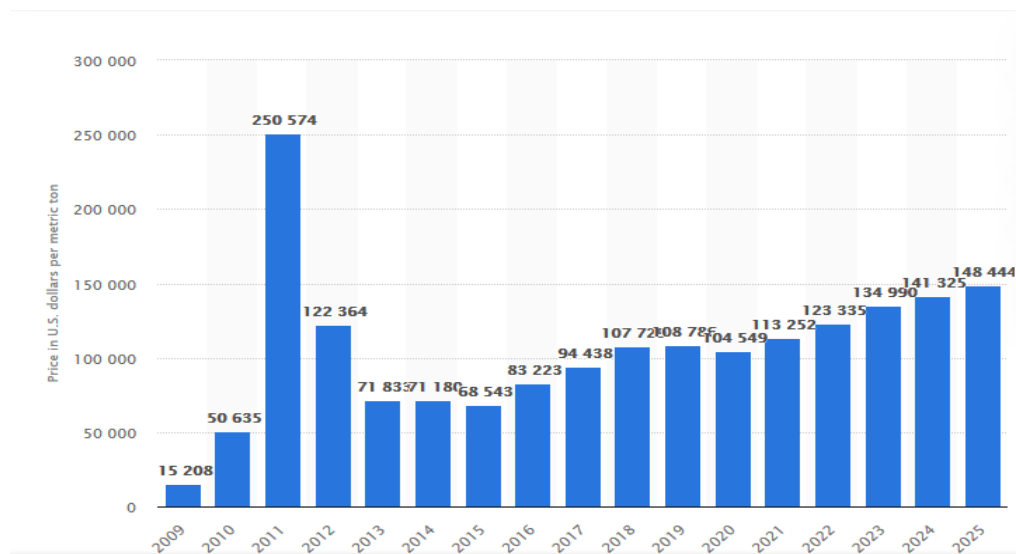


Figure 2.12: Prediction price of neodymium [46]

2.5.2 *B-H Loop and Demagnetisation Characteristics*

Figures 2.12 and 2.13 below show typical characteristics and thermal effects for NdFeB and SmCo, respectively. Parameters like remanent flux density (B_r) at zero magnetic field, the coercive field (H_c) at zero flux density, and irreversible demagnetization can be found in these figures. The main diagonal lines show the material's magnetization characteristics in the second quadrant. The magnet is operating in a safe linear region if the main diagonal line crosses the intrinsic curve above the knee point at any temperature. However, if the main diagonal line crosses below the intrinsic curve, then the magnet will start to demagnetise due to the relative recoil permeability of the magnet. It is essential to make sure that the temperature of the permanent magnets does not exceed 150°C for NdFeB and 350°C for SmCo to avoid demagnetisation.

Two factors can cause the partial or irreversible demagnetisation of the magnet: operating temperature and the magnetic circuit. To avoid the demagnetisation of the magnets in PM

motors, the current in the negative d -axis should be limited. Figure 2.13 shows the demagnetization curve of a NdFeB permanent magnet of grade N42UH, which is used in the machine designed. It can be seen that 0.6T is the safe limit of magnetic flux density, which is just above the demagnetization knee at 150°C. Therefore, the lower limit of flux density in the permanent magnet has been set at 0.6T.

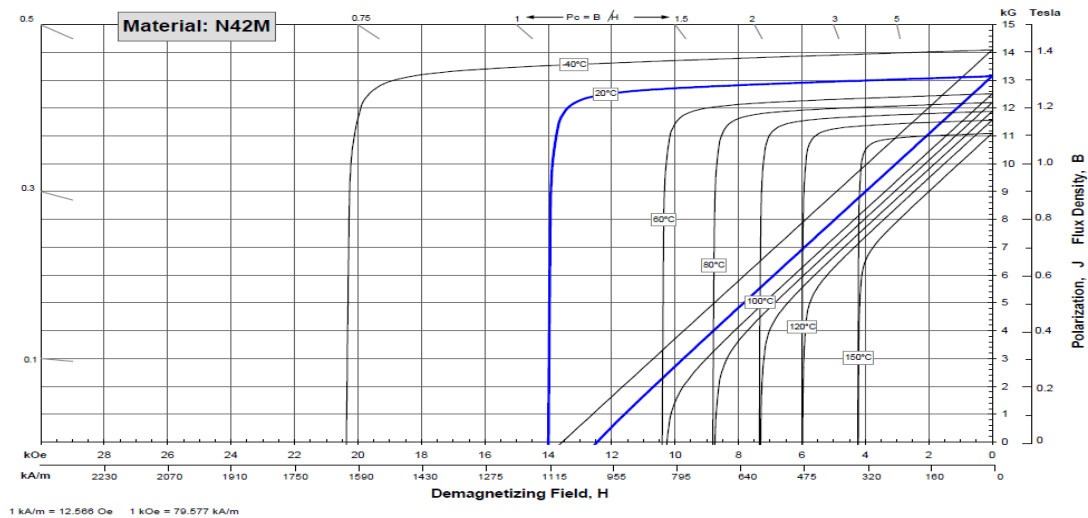


Figure 2. 11 Magnet characterisation B-H curve for NdFeB [47]

Meanwhile, for the PM machine with SmCo as the magnet material, the grade Recoma 33E is used. Thus, the lower limit of its permanent magnet flux density is 0.2T at 350°C.

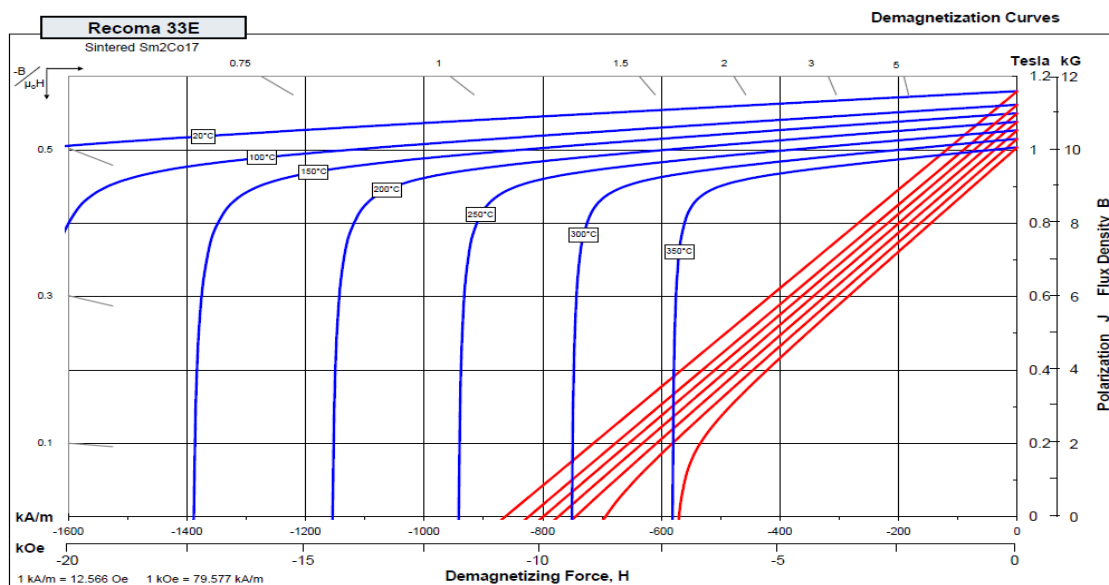


Figure 2. 12 Magnet characterisation B-H curve for SmCo [48]

Table 2. 5 The PM flux density

Temperature	Flux Density	
	NdFeB	SmCo
20°C	Below 0T	Below 0T
120°C	0.5T	Below 0T
150°C	0.6T	Below 0T
250°C		Below 0T
350°C		0.2T

A fault detection strategy based on the information contained in the branch-current spectrum has been proposed by Ruschetti et al. [49] to detect rotor faults in PMSMs to avoid overheating in the windings produced by the branch current itself. It was concluded that if demagnetization happens in a single magnet in a PMSM with a series winding configuration, this will reduce the induced EMF current. Meanwhile, with a parallel winding configuration, partial demagnetization effects can be detected in the branch currents, thus giving clear signs of rotor faults in the PMSM. Hence, limiting the maximum phase current can protect the machine indirectly.

2.6 Torque Production

High torque density has become one of the reasons for permanent magnet synchronous motors (PMSMs) being widely used in many industrial applications. For PM motors, there are three main components of electromagnetic torque: mutual torque, reluctance torque, and cogging torque [35]. The interaction between the magnet field and the magneto-motive force of the stator current winding is called as mutual torque. Reluctance torque occurs due to the rotor saliency producing variations in air gap reluctance according to the rotor position. Meanwhile, the interaction between the permanent magnetic field and the slotted stator will produce cogging torque. Reducing cogging torque and torque ripple in mutual torque can improve the quality of the torque. The electromagnetic torque strongly depends on the properties of the iron material.

The value of torque for an interior PMSM can be calculated analytically [50]. The conventional method calculates output torque by using an equivalent circuit to define the d - and q -axis

inductances to estimate the reluctance torque. Then, PM torque and reluctance torque are summed to determine the total torque. However, the conventional method is not simple. Thus, a new simple process has been introduced to obtain the full torque value, especially in designing a new machine or if the machine has an air gap which is non-symmetrical in shape.

A method to estimate the iron loss has been proposed [51] based on equivalent circuit modeling to find the iron losses. Finite element analysis (FEA) is used first to obtain the d - and q -axis inductances. Then, the iron loss resistance is calculated using the values of inductances. The results showed that the proposed method achieves good agreement with experimental results. Also, a plan to analyse torque ripple reduction for axial flux PM synchronous motors by using analytical magnetic field calculations has been published [52, 53].

In the IPMSM, the d -axis current is used not only for field weakening but also for generating the reluctance torque. Therefore, in producing a given required torque, numerous combinations are feasible of magnetic and reluctance torque. The torque-speed curve was achieved from an FE model by solving a 2D transient with motion. The electromagnetic torque equation can be expressed in the equation below:

$$T = \frac{m}{2}p(\Psi_d i_d - \Psi_q i_q) \quad (2.12)$$

where m is the number of phases, p is the number of pole pairs, Ψ is flux linkage, and i is the instantaneous current. The subscripts d and q indicate the d -axis and q -axis, respectively.

For the classical analysis, the equation for flux linkage is:

$$\Psi_d(i_d) = \Psi_m + L_d i_d \quad (2.13)$$

$$\Psi_q(i_q) = L_q i_q \quad (2.14)$$

where the term $\lambda\Psi_{d,PM}$ is the d -axis flux linkage from the rotor flux permanent magnets. Substituting the terms 2.9 and 2.10 into equation 2.8, the conventional torque equation of IPMSM becomes:

$$T = \frac{m}{2}p(\Psi_m i_q - (L_d - L_q)i_d i_q) \quad (2.15)$$

The values of $\Psi_{d,PM}$, L_d and L_q can be calculated from an FE model by solving a 2D transient with motion.

The torque produced oscillates around a mean value, varying in value with rotor position and dependent on stator current. Unfortunately, two undesired pulsating torque components will affect the performance of PM machines: ripple torque and cogging torque [54]. The pulsating torque occurring in the PM machine will create problems because the ripple can lead to mechanical vibration and acoustic noise [55].

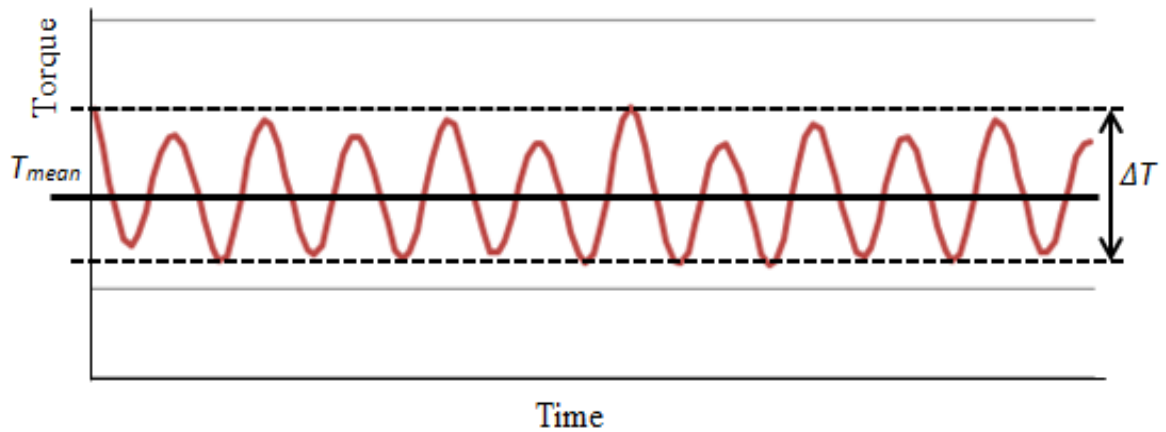


Figure 2. 13 Torque at load condition

The following actions have been proven acceptable to reduce cogging torque and torque ripple to improve the performance of PM machines:

- Using soft magnetic composite (SMC) material as the stator core [54].
- Using two stacked permanent magnet reluctance generators (PMRGs) whose rotors differ in spatial phase by 180° in electrical angle [36].
- Increasing the stator slots [55].
- Employing an appropriate magnet shape [52].
- Selecting a suitable combination of slot and pole numbers, slot opening design, and air gap variation [35].

2.7 Losses and Efficiency

Three main types of losses in permanent magnet machines are iron, copper, and magnet losses. Iron losses have been recognized as a significant issue at high speeds in interior permanent magnet machines. These iron losses include stator losses, rotor losses, and PWM switching iron losses. Most of the research on reducing iron losses has focused on stator losses [56]. Solutions include increasing the stator slot openings, changing the angular position of the rotor barriers, and optimally selecting rotor and stator geometries. However, rotor losses cannot be neglected during the design process to avoid an underestimation of the operating temperature [57, 58]. A study of the relationship between rotor losses and size of PM machines [42] concluded that rotor loss also causes an increase in the working temperature, and bigger machines will have a higher probability of rotor loss occurring. Each of the losses of the machine contributes to the local inner heat flows [59].

The most significant part of the total losses in low- and medium-speed applications is the copper loss. In high-speed applications, copper losses in interior permanent magnet motors are an essential issue. The use of high electrical frequencies at higher speeds can make it necessary to consider practical effects such as the skin-effect, proximity effect, and circulating current. In general, these effects can be reduced by using conductors, which are bundles of multiple, thin, insulated strands, and ensuring the appropriate transposition of both the conductors within each bundle and of the bundle position within the slot. Making a gap between the coil and the slot opening may also achieve a substantial reduction in losses [3]. Ohmic resistance losses depend on the current in the coils, while eddy current copper losses depend on the speed of the motor.

The iron losses consist of hysteresis and eddy current losses. The former originates from the hysteresis band of the core, while the conductivity of the core material causes the latter. The hysteresis loss is higher than the eddy current loss at the fundamental frequency. However, the eddy current loss becomes dominant in the high-frequency region.

In interior PM motors, magnet losses are generally not a significant source of losses as the rotor iron effectively shields the magnet from the high-frequency flux variations. However, magnet losses will become substantial in surface permanent magnet machines where the rotor magnets are directly exposed to high-frequency air gap flux variations. On the other hand, mechanical losses include friction and windage loss, but these are not dealt with here.

2.7.1 Copper Loss

When current is flowing through a wire, it will cause copper loss. Copper loss is the dominant type of loss in a machine under most operating conditions [60]. Copper losses are obtained analytically by a calculation as in the equation below:

$$P_{cu} = 3 R_s I_s^2 \quad (2.18)$$

where R_s is the stator winding resistance of a phase and I_s is the RMS current running in the winding resistance of a phase.

However, changing the temperature of the winding will cause variation in the winding resistance, R_s . Therefore, the copper loss increases when the copper temperature increases due to increased winding resistance. This equation is used to calculate the value of winding resistance:

$$R_{s(T)} = R_{s20}(1 + 0.0038(T - 20)) \quad (2.19)$$

where $R_{s(T)}$ is stator resistance at temperature T and R_{s20} is stator resistance at a temperature of 20°C.

Copper losses during high-speed operation are essential for the interior PM motor. Large negative d -axis currents with high electrical frequency are required for field-weakening. Thus, a few practical effects, such as circulating current, skin, and proximity effects, need to be considered [3]. If the conductors used are bundles of multiple, thin, and insulated strands, this can reduce these effects.

2.7.2 Iron loss

Iron loss is produced in a magnetic material operating in an alternating magnetizing field. It generally consists of hysteresis loss and eddy current loss. Here, the total iron loss is simply modelled as:

$$P_{iron} = k_{iron} \cdot P_{15} \cdot \left(\frac{B}{1.5}\right)^2 \cdot m \cdot \left(\frac{f}{50}\right)^2 \quad (2.20)$$

where k_{iron} is a dimensionless coefficient in the range of 1.5 to 2, P_{15} is the material losses coefficient [W/kg], m is the mass of the region where the losses are calculated [kg], and f is the operating frequency [Hz].

For low-speed applications, the eddy current losses in permanent magnets and the rotor core back are usually neglected, but this is not the case for high-speed machines, and they must typically be included in the thermal model [57]. For an interior PM motor, magnet loss is not a significant issue since the rotor effectively shields the magnet from the high-frequency flux variation. Still, for surface PM machines, magnet loss is substantial because the rotor magnets are directly exposed to high-frequency airgap flux variations.

2.7.3 Stray Loss

The stray losses are due to higher winding space harmonics and slot harmonics. These losses take place in the surface layers of the stator and rotor adjacent to the air gap and the volume of the teeth. The calculation of stray losses is complicated and does not guarantee a satisfactory accuracy. In practice, stray losses are evaluated as:

$$P_{str} = C_{str} \omega^2 (i_d^2 + i_q^2) \quad (2.21)$$

where C_{str} is the stray loss coefficient.

2.7.4 Total Loss

Summing the above losses, the total loss P_t is equal to:

$$P_t = P_{cu} + P_{iron} + P_{str} \quad (2.22)$$

If the power of the drive is P_o , then the input power of the motor is:

$$P_{in} = P_o + P_t \quad (2.23)$$

2.7.5 Efficiency

At any operating condition, if P_{loss} is equal to all losses in the motor, then the energy efficiency of the motor is:

$$\eta_{motor} = \frac{P_o}{P_{in}} = \frac{P_o}{P_o + P_t} \quad (2.24)$$

2.8 High-Temperature Machine and Its Applications

For some applications such as electrical machines in gas turbines, industrial process control and motors and downhole equipment requires very high special power machines, which have a high level of internal heat dissipation, might with limited cooling. The high-temperature range for the device depends on the applications itself. However, a wide range from 250°C to 800°C was considered. Besides, some researchers declare that high temperatures would mean up to 550°C.

Switched reluctance (SR) motor is always used in applications requiring high temperatures. The SR motors are known as a simple mechanical structure without windings and permanent magnets on the rotor. The machines are called doubly salient machines because both the stator and rotor have salient poles. Even with poor performance, SR motor represents a competent candidate for air-craft applications of its inherent modularity and fault-tolerance. The structure is based on concentrated windings, and the lack of permanent magnet makes the machine behaviour independent from the temperature and safe as regards some necessary failure

conditions [61]. Besides easy to build, SR motor also more robust, cheaper, and no dragging torque is produced in the case of phase short-circuit.

2.8.1 Principle operation of switched reluctance motor (SRM)

With force created by the rotor's magnetic reluctance, the rotor pole will be aligned with the nearest stator pole. As the rotor rotates, the inductance of the phase windings of a machine varies between the inductance's values concerning the rotor angle.

The 6/4 three-phase structures are among the most common SRM structure, as shown in figure 2.14. When stator pole axis AA' and rotor pole axis aa' are in alignment, they are in the minimum reluctance position. Variable reluctance and the existence of variation in inductance will make the rotor develops a torque. There is no torque developed if the position of the shaft is aligned with stator pole axis BB' . However, the torque will be developed if the rotor rotates further 30° . The cyclic process will happen continuously.

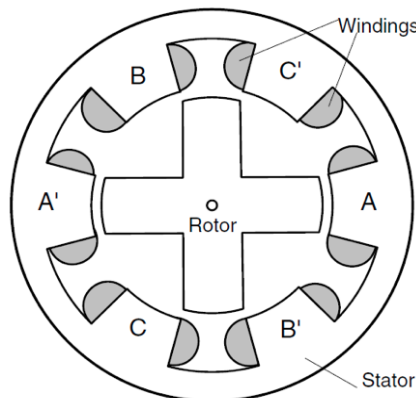


Figure 2. 14 The SRM structure [61]

Size reduction of electrical motors is an important issue. Two methods can be applied to reduce motor weight and increase power. Either electromagnetic design modification or increase the cooling effect of the motor. By identifying the locations where high temperature exists and consider the temperature limitation for the materials can increase the cooling effect of a motor. A new IPM motor using rotor cooling to enhance the motor power per specific weight has been proposed [62].

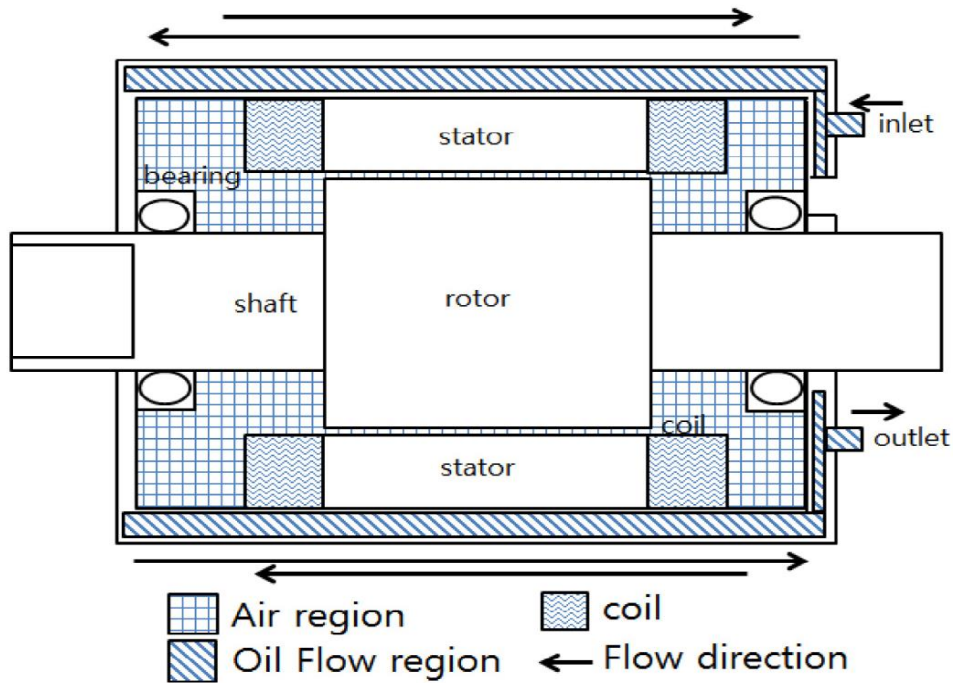


Figure 2. 15 Housing jacket cooling type rotor [62]

Not all existing motors are designed to survive in harsh, high-temperature environments. However, in specific applications such as in the aerospace industry, the motor needs to be developed for high temperature. For example, a prototype has been built for high-temperature switched reluctance and BLDC Motors [63]. Both are using the same high-temperature materials, and the capability of the motors are compared.

The stator and rotor are built up to form stacks of magnetic-alloy laminations. Meanwhile, the stator windings are made of high-temperature magnet wire insulated with a thin enamel film, and the wire winding is bonded together with ceramic binder.

A thin-walled cylinder is positioned coaxially between the rotor and stator to prevent debris from stator winding to reach the rotor. The stator windings are wound on wire spools made of ceramic. Meanwhile, to keep debris from the motor migrates into bearing, the stator and rotor are encased in a stator housing with rear and front-end caps, and rear and front bearings for the rotor shaft are mounted on outer sides of the end caps. Also, there is no windings or magnets on the rotor to avoid failure while operating under high temperature or high-pressure conditions. Both motors are capable of operating at 460 °C continuously for long durations.

Table 2.6 presents high-temperature materials that have been used to build each part of the motors.

Table 2. 6 Materials used

Parts	Materials
Rotor and stator	Iron-cobalt-vanadium alloy (to have high magnetic saturation)
Stator winding	high-temperature magnet wire insulated with a fully cured (1400°-1500°F.) vitreous enamel film bonded to the Wire conductor
bearings	ceramic balls coated with tungsten disulfide.
Motor capability	operating at 460°C continuously for long durations.

For aerospace applications, Ultra-High-Temperature Ceramic (UHTC) materials are become popular among researchers since their capability to develop components for extreme use [64]. Aerospace applications demand ultra-high temperature machines since the operation temperatures above 1600 °C and possibly exceeding 2200 °C [65]. Therefore, some parts of the rocket materials must meet several requirements simultaneously. It must be a high melting temperature, minimum strength, and environment resistance.

A study has been done to improve motor load performance and efficiency by proposing a new method of reducing the resistivity of cast aluminium by boron-aluminium alloy. The results show that the primary technical performance of ultra-efficient motors by boron-aluminium alloy rotor is far better than the typical cast aluminium rotor in terms of efficiency, temperature, and power factor. Also, in terms of rated speed, slip, and rated current, ultra-efficient motors by boron-aluminium alloy have much better performance [66].

2.9 Thermal Analysis

Significant challenges are faced in determining accurate values for thermal parameters such as the thermal conductivity of the composite mixture of conductors and potting materials within the slot, or thermal resistance between the stator lamination and the frame. It is imperative to model the heat transfer behaviour in electrical machines accurately, at least to some degree, as this defines the cooling capability and, consequently, the nominal power of the machine. Generally, the heat-transfer might be different if the machine is cooled with water instead of air. Accurate modelling of heat transfer is practically impossible without finite element analysis due to the complex three-dimensional geometries involved. Even though faster microprocessors are available, 3D FE analysis is still too time-consuming when used for dynamic thermal analysis, and often different kinds of analytical methods are applied to model the heat transfer in the machine instead.

There are three main types of thermal machine models: analytical modelling, lumped-circuit models, and finite-element analysis. Analytical modelling is useful for obtaining physical insights into simple thermal problems, such as the temperature distribution within a slot. Meanwhile, a lumped-circuit model has intermediate complexity between analytical modelling and finite-element analysis [3]. It provides a rapid solution that can be utilized within optimization loops while still retaining useful physical insights into the model structure. However, the most accurate method is the finite element analysis, which can consider the detailed motor geometry. At the same time, computational fluid dynamics (CFD) also becomes another choice for researchers [67, 68]. The researcher must choose which type of thermal modelling to use. Some prefer just one type, and some combine or compare more than one type of thermal modelling. Table 2.7 states the reasons why each thermal modelling type should be applied.

Table 2. 7 Types of the thermal model

Lumped parameter	FEM Modeling	3D CFD Calculation
<ul style="list-style-type: none"> • Gives a rough estimate of the hotspot very quickly. • Takes much less time. • Accuracy is higher than 2D FEA. • Easy to use. • With more excellent computational capabilities, it will be much more detailed. • Efficient, robust mathematical routines are used in the network solver. 	<ul style="list-style-type: none"> • The solution process is straightforward and does not require a lot of computational time. • Better with a more complex component shape. • Clearly illustrates more accurate and finer details in the conducting regions due to unsymmetrical flux density and related power loss distribution inside the machine. 	<ul style="list-style-type: none"> • The selection of optimal cooling flow for the selected thermal regime becomes straightforward. • 3D transient thermal model, determining the temperature rise of the stator windings accurately. • A reliable way of obtaining heat transfer coefficients or static temperature distribution. • Very accurate.

However, each type of thermal model has weaknesses. FEA modelling needs more time to build the geometry to use this method for thermal analysis. Thus, it is very time-consuming. Meanwhile, besides being an expensive and prolonged process for CFD thermal modelling, it is also prolonged because there is a need to define physical material properties and boundary conditions accurately, and it is only applicable for steady-state conditions [69].

It is essential to model and analyse thermal behaviour to achieve the desired output. The most temperature-sensitive parameters for PMSM are stator winding resistance and the demagnetisation characteristics of the permanent magnet [69].

Schofield and Giraud-Audine [14] reported the findings of a case study into the design of a traction machine for an electric vehicle. The thermal capability of the machine was the second most critical constraint. The temperature rise in the machine can be estimated by using the thermal impedance of machine components and the frame interface. A liquid cooling system was considered in this research. A lumped parameter model was used, where the motor was split into several discrete regions according to expected temperature variation. As a result, using liquid as a cooling system could lead to a drastic reduction in the machine mass and gave a better power/mass ratio. However, accurate estimation of heat loss at the frame surface was difficult due to its dependence on the frame geometry and temperature and the flow rate of the cooling medium.

Several factors such as geometry and materials and the surface area and size of the machine can determine the rate of heat removal in the air-cooled electric machine [70]. For air-cooled electric machines, the cooling method will be more challenging for larger machines because, with L as the length of a machine, the losses are proportional to volume L^3 and the surface equivalent to L^2 . The rotating speed of the machine and size of the rotor and air gap strongly influence the air gap convective heat transfer and make it variable.

2.9.1 Heat Transfer

Heat is energy in transition under the motive force of a temperature difference, and the study of heat transfer deals with the rate at which such energy is transferred [70, 71]. Heat transfer is thermal energy in transit due to a spatial temperature difference. Whenever there exists a temperature difference in a medium or between media, heat transfer must occur. When temperature differences are present in any material, heat flows from the hot to cold regions until the temperatures are equalised. This activity occurs even when the movement of macroscopic portions of the matter is prevented, as in solids.

In solids, the conduction heat is partly due to the impact of adjacent molecules vibrating about their mean positions, and partly due to internal radiation. When the solid is metal, there are also large numbers of mobile electrons that can easily move through the material, passing from one atom to another, and they contribute to the redistribution of energy in the metal. Indeed, the contribution of mobile electrons predominates in metals. They are thus explaining the relationship which is found to exist between the thermal and electric conductivities of such materials.

For heat-transfer, the larger the area through which heat is conducted, the larger the heat transferred. The same concept applies to convection, where the more significant the surface area in contact with the fluid, the larger the potential convection heat-transfer, which will happen. Larger surfaces will emit more thermal radiation than small surfaces as well.

There are three modes of heat transfer:

- a) Conduction – this happens due to the vibration of molecules in a material. Energy is transferred on a molecular scale with no movement of macroscopic portions of matter relative to one another. This heat transfer mechanism is found in a solid body. For this mode, heat-transfer will almost always be directly proportional to the area.
- b) Convection – here, heat transfer occurs when temperature differences exist at the boundary between a fluid and a solid. Heat is transferred from hotter to colder material, but the redistribution of energy is partly due to conduction, and partly due to the motion of the fluid itself.
- c) Radiation – this does not depend upon the existence of an intervening medium. All matter at temperatures above absolute zero emits energy in the form of electromagnetic waves.

2.9.2 Conduction Heat Transfer

This type of heat transfer is normally found in a solid body and only sometimes in liquids and gases. Heat transferred from a high temperature region to a low temperature region is proportional to the temperature gradient:

$$q_{cond} = -kA \frac{\partial T}{\partial x} \quad (2.25)$$

where q is the heat transfer rate, $\frac{\partial T}{\partial x}$ is the temperature gradient in the direction of the heat flow, and k is the thermal conductivity of the material. Table 2.8 shows the example of several materials with conductivity values.

Table 2. 8 Thermal Conductivity

Materials	Conductivity (W/m/°C)
Insulating materials	0.1
Copper	400
Air	0.026 at ambient temperature
Aluminum alloy	170

2.9.3 Convection Heat Transfer

Convection heat-transfer is comprised of two mechanisms. Energy can not only be transferred due to random molecular motion or diffusion, but it can also be moved by bulk or macroscopic, the motion of the fluid.

In general, convection heat transfer occurs between the fluid in motion and a bounding surface when the two are at different temperatures. When fluid flow over a heated surface, a consequence of the fluid-surface interaction is the development of a region in the fluid through which velocity varies from zero at the surface to a finite value u associated with the flow. This region of the liquid is known as the hydrodynamic, or velocity, boundary layer. If the surface and flow temperatures differ, there will be a region of the fluid through which temperature varies from T_s at $y=0$ to T_∞ in the outer flow. This region called the thermal boundary layer, maybe smaller, larger, or the same size as that through which the velocity varies. In any case, if $T_s > T_\infty$, convection heat transfer will occur from the surface to the outer flow.

At the interface between the surface and the fluid ($y=0$), the fluid velocity is zero, and heat is transferred by this mechanism only. Convection heat transfer may be classified according to the nature of the flow.

- Forced convection: when the flow is caused by external means such as a fan, a pump, or atmospheric winds.
- Natural convection: the flow is induced by buoyancy forces, which are due to density differences caused by temperature variations in the fluid.
- Mixed force and natural convection:

Each of the types of losses in the machine contributes to the local inner heat flows [69]. The heat transfer, starting from the solid parts (winding heads, housing, end shield) to the gaseous components (central air), is mainly determined by convection.

An appropriate equation for convection heat transfer is:

$$q_{conv} = hA(T_s - T_\infty) \quad (2.26)$$

where q_{conv} the convective heat flux (W/m²), is proportional to the difference between the surface and fluid temperatures T_s and T_∞ , respectively. This expression is known as Newton's law of cooling. The parameter h is termed the convection heat transfer coefficient, and A is the

surface area. The value depends on conditions in the boundary layer, which are influenced by surface geometry, the nature of the fluid motion, and an assortment of fluid thermodynamic and transport properties. Table 2.9 shows the typical value of the heat transfer coefficient that always been used.

Table 2. 9 Typical values of the convection heat transfer coefficient

Process		h (W/m.k²)
Free convection	Gases	2-25
	Liquids	50-1000
Forced convection	Gases	25-250
	Liquids	100-20,000
Convection with phase change	Boiling or condensation	2500-100,000

In the PMSM, convection usually takes place in the airgap and around the end winding. It is essential to find an accurate value for the h coefficient for any convection surface in the machine. Therefore, a proven empirical formulation (correlations) is used [49]. The following dimensionless numbers used are the Reynolds (Re), Grashof (Gr), Prandtl (Pr), and Nusselt (Nu) numbers. The general correlation equation for natural convection is shown below,

$$Nu = a (GrPr)^b \quad (2.27)$$

Meanwhile, a general equation for the forced convention is;

$$Nu = a(Re)^b (Pr)^c \quad (2.28)$$

where a , b and c are constants given in the correlation. The other equations are stated below:

$$Re = \rho v L / \mu \quad (2.29)$$

$$Gr = \beta g \Delta T \rho^2 L^3 / \mu^2 \quad (2.30)$$

$$Pr = c_p \mu / k \quad (2.31)$$

$$Nu = h L / k \quad (2.32)$$

where,

- h - heat transfer coefficient [W/m²/°C]
- μ - fluid dynamic viscosity [kg/s.m]
- ρ - fluid density [kg/m³]
- k - fluid thermal conductivity [W/m/°C]
- c_p - fluid specific heat capacity [kJ/kg/°C]
- v - fluid velocity [m/s]
- ΔT - delta temperature of surface fluid [°C]
- L - the characteristic length of the surface [m]
- β - coefficient cubic expansion 1/(273+ T_{fluid}) [1/°C]
- g - gravitational force of attraction [m/s²]

The product of Gr and Pr is used in natural convection systems. Meanwhile, to determine if the forced convection is laminar or turbulent flow, the Reynolds number (Re) is used.

2.9.4 Radiation Heat Transfer

Radiation is the mode of heat transfer from a surface due to energy transfer by electromagnetic waves, which commonly takes place in a vacuum. The equation for radiation heat transfer is as shown below:

$$q_{rad} = \varepsilon_1 \sigma A. (T_w^4 - T_\infty^4) \quad (2.33)$$

where σ is the Stefan-Boltzmann constant, and ε is emissivity. Materials with different surfaces present different emissivities.

2.10 Cooling Methods

As mentioned above, three primary sources of heat in a PM machine are:

- Copper winding
- Rotor permanent magnet material
- Lamination stacks of the rotor and stator

For the copper winding, heat is generated as Joule losses due to the current flowing in the winding, as shown in equation 2.23. Heat is also produced by the eddy current induced inside the magnet, which is dependent on the frequency, f , and flux density, B . To decrease the eddy current losses, a large magnet has to be segmented into small pieces. For the lamination stacks, the heat is generated from the induced eddy current, hysteresis, and other iron losses. This loss can be calculated using equation 2.25. Thus, different cooling techniques or heat transfer fluids are widely studied to make sure that the machine is operating below its temperature limits.

Fluids that flow through or around a device to prevent it from overheating are called coolants. The ideal coolant should have a high thermal capacity, low viscosity and low cost, be no-toxic, and some applications also require an electric insulator coolant. Coolants may be gases, liquids, molten metals, liquid gases, nanofluids, or solids.

The most common cooling methods for the thermal management of electrical machines use air either as convective airflow or forced circulation. Air as a cooling material is robust and low in cost. However, fully enclosed machines need an additional fan attached to the shaft to increase convective heat transfer. Therefore, the machine will be larger and heavier. For high power density machines, forced air-cooled is preferred, which is directed to the end windings and air gap. However, these cooling systems are quite sensitive to dust and need air filters and added fans as well [72].

The most popular cooling method is a water jacket, which is a liquid coolant that cools a frame. The coolant can be water or another liquid with better cooling capabilities such as ethylene glycol, deionized water, or dielectric fluids. Compared to air cooling methods, liquid cooling is more expensive but more effective. If the end windings covered are by some compound, which is an insulating material with high thermal conductivity, this makes the water cooling method

more significant [73]. Water cooling also can be adopted through an aluminium jacket sandwiched in between two slotted stator cores on an axial-flux PM machine, as shown by Odvarka et al. [74]. Water cooling is typically applied in high power machines. By reducing the inlet coolant temperature and increasing its flow rate, the efficiency of a machine with liquid cooling can be improved.

Spray cooling is another option for heat removal at the end winding [72]. Besides that, allowing liquid to flow inside the armature conductors can be another cooling method. This method is more efficient because the heat is removed from the source. However, spray cooling can only be applied to large machines. Those with permanent magnets on the rotor need closer attention because the different cooling method has to be involved in making sure that the temperature still is kept within certain limits to avoid demagnetization.

Research has been conducted on cooling machines by combining two types of cooling methods: water cooling and evaporative cooling techniques [75]. Evaporative cooling was adopted for the stator. Unlike when cooling water is forced to flow through a water jacket, an evaporative coolant is forced to flow through narrow slots and the axial slots in the stator cavity. However, with this technique, most of the stator iron core and the stator iron winding are immersed in evaporative coolant. Meanwhile, the coolant in the stator cavity and the narrow slots absorbs the heat. Therefore, the evaporative cooling technique is not suitable for most electrical machines. It is only suitable for special machines like PM motors used in the underwater apparatus.

Copper bars have been used in an axial-flux PMSM to improve the cooling system [68]. The copper bars act as extra heat carriers, and the use of high-conductance potting material in the end winding of a liquid-jacket-cooled machine significantly improves its thermal behaviour.

Comparisons have also determined the relative efficiency of air and water cooling method [76]. From the results of thermal analysis, it was proven that water cooling dissipates more power even with lower flow. Water is approximately 1000 times denser than air and can store a much higher quantity of heat per unit of mass, as shown in Table 2.8 below.

Table 2. 10 Physical properties of fluids [76]

Fluids	Specific Heat	Density
Water	4217 J/kg.°C	998 kg/m ³
Air	1060 J/kg.°C	1.2 kg/m ³

Several attempts have been made to reduce the temperature of PM machines besides using coolant. A recent study by Li Weili et al. (2010) found that by changing the arrangement of permanent magnets in a PM machine, higher fundamental flux density and back EMF, lower space harmonics, and iron loss can be produced [77]. As a result, the temperature in the PM machine is reduced too. The authors also reported that by adding a copper screen between the PM and the alloy sleeve could reduce eddy loss in the rotor. Thus, the temperature will decrease accordingly. The thicker the copper screen, the lower the temperature will occur. Even small gap size ratios can improve the average heat transfer on the stator surface in the air gap [34].

Stator and rotor lamination with different amounts of alloy content can also lead to a 2-10% variation in the temperature of rotor and winding, according to Nategh [78]. A lower number of alloy content in a lamination material will reduce cost but increase lamination losses. Hence, besides using coolant for the cooling methods, the temperature of the machine can be controlled by applying appropriate design techniques and choosing the most suitable materials.

2.11 Summary

An extensive review has been carried out in this chapter to present the characteristics of electric motors for vehicle applications. Much researches about PM motors have been conducted. However, a lot of work still needs to be done in terms of thermal analysis and the materials used. Besides, the high price of PM materials leads to the need to find a way to reduce the use of PM materials. Therefore, this work focuses more on smaller size PM machines that can achieve the desired torque and power density as in the existing machine.

A survey has been conducted for different types of electric motors, and comparisons have been made among different types of PM motors to identify suitable topologies for EV applications. The requirement and characteristics of electric motors for EV applications have also been presented and discussed. From the result, an IPMSM has been chosen for this research. Thus, the characteristics and topology of the Nissan LEAF motor are selected as a reference and an

indicator to produce a smaller PM motor. The features of the PM have also been discussed in the context of avoiding demagnetisation of the magnet. NdFeB and SmCo have been selected as the magnet materials due to their behaviour and ability to produce the desired output. Two different windings for PM motors have also been studied to find the most suitable option. Relevant equations and calculations have been shown, which can be used to estimate the characteristics and output of the motor. The most important part of this work is to ensure that the PM machine can work even at high temperatures. Hence, a survey has been done on previous high-temperature motors and materials used to construct the motor. Besides, several types of thermal analysis and coolant methods have been investigated to find the appropriate choice for the motor.

Chapter 3 Thermal Modelling

This chapter will describe the method used to predict the temperature in some of the essential parts in a permanent magnet motor. There are three main types of thermal models usually used, such as analytical modelling, lumped-circuit models, and finite-element analysis. As described in Chapter 2, to obtain real insight into simple thermal problems, analytical modelling is advantageous. However, in terms of thermal modelling for detailed motor geometry, compared to the lumped parameter model, finite element analysis is more accurate and faster. Also, some researchers combine more than one type of thermal model to predict the temperature.

In this study, finite element analysis has been selected to predict the temperature in the PM motor. JMAG software has been used in this research. The losses obtained from the electromagnetic field analysis are used as the heat source in the thermal analysis.

This study is focusing on reducing the size of the permanent magnet motor. Therefore, thermal modelling is essential because the smaller motor needs a higher current to achieve desired torque, and a higher temperature is predicted to occur in the motor. Most researchers usually do not pay much attention to thermal analysis during machine design as much as the electromagnet design. Besides, the parameters of the motor will keep changing because this research aims to find the smallest motor that can run safely and have the desired output.

Thermal modelling has been conducted to ensure that the damage that can occur after the demagnetisation of the magnets is prevented and at the smaller motor can be run without any problems even though it becomes higher temperature. Knowing the thermal behaviour of a motor gives many advantages because it not only prevents overheating but will also improve its utilization during regular operation. Increasing temperature is a significant factor that compromises the state of magnetization of magnets and, consequently, the stability of the motor. Details explanation about the thermal modelling that has been applied will be discussed in the next sections.

3.1 Lumped Parameter Thermal Model

The lumped parameter model has been the most common approach for the thermal analysis of electric machines during the past few decades. It is the simplest way to analyse the thermal field based on the eddy current loss, which is derived using the Motor-CAD software package. During this analysis, an accurate thermal resistance network using a T-equivalent lumped-parameter system is defined. The components with similar temperatures are lumped together to represent a single node. Then, thermal resistances are placed in the circuit to separate the nodes so that the model also shows the heat transfer pathways in the machine [72]. Also, the power sources are placed at nodes where losses occur. The equation below is used to calculate the phase resistance at a working temperature to find the stator copper losses:

$$R_{at} = R_{20}[1 + (T - 20)P_t] \quad (3.1)$$

where R_{20} is the resistance measured at 20°C, T is the working temperature and P_t is the temperature coefficient.

3.1.1 Conduction Resistances

It is essential to define the type of heat transfer for each part of the machine to calculate the thermal resistance. The transfer can be by conduction, convection, or radiation. Generally, most parts of the motor, such as magnets and lamination, transfer heat by conduction. Thus, for conduction resistance, the equation is:

$$R_{cond} = \frac{l}{S \cdot k} [C/w] \quad (3.2)$$

where l is the length of the body in the direction of heat flow, S is the cross-sectional area, and k is the thermal conductivity.

The thermal conduction coefficients, as in Table 3.1, is used to find the value of the resistance in the thermal network.

Table 3. 1 Material Properties [79]

Regions	Conductivity, λ (W/m/°C)	Density, ρ [kg/m³]	Specific Heat Capacity, c_p [J/kgC]
Copper coils	375	8900	390
Aluminum alloy	168	2790	833
Steel sheet stator and rotor	28	7600	465
Permanent magnet (NdFeB)	8	7500	450
Permanent magnet (SmCo)	10.5	8500	418
Shaft	40	7800	485
Air (at 40°C –ambient temp)	0.28	1.127	1007
epoxy	0.22	1200	1500
Nomex 410	0.14	1400	1300

3.1.2 Lumped Parameter with MotorCAD

For more detailed results in a thermal analysis, a lumped parameter circuit needs great software for simulation purposes. In this work, MotorCAD has been used to obtain accurate values in the thermal analysis. Some input data inside MotorCAD software needs to be completed first. Then after choosing the cooling option, the result for the temperature for each part in the machine can be calculated. However, this process is more accurate for steady-state analysis. Figure 3.1 shows the axial section of the machine that has been designed.

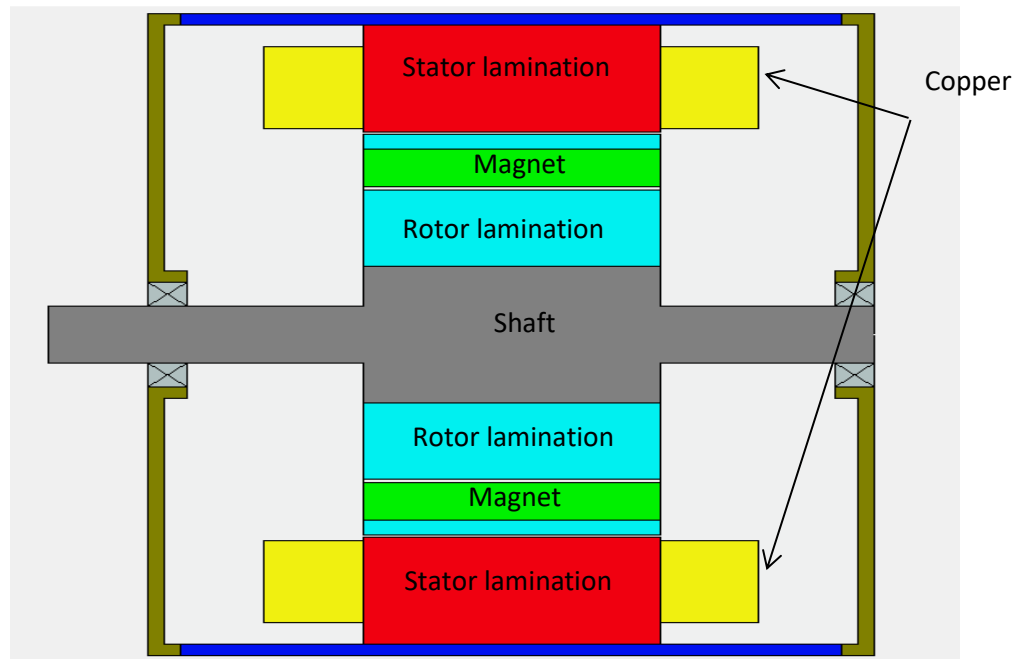


Figure 3. 1 Axial Section of the IPM Machine

MotorCAD can also present the results of the thermal analysis in the form of a schematic circuit, as shown in figure 3.2. The values of power, resistance, and capacitance will be displayed as well.

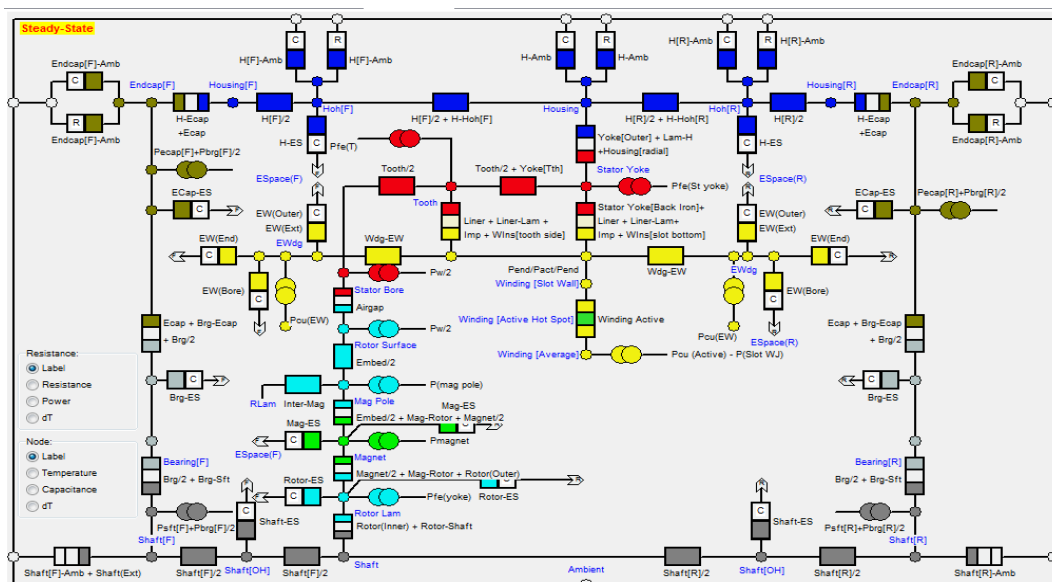


Figure 3. 2 Schematic circuit

3.2 Finite Element Analysis Thermal Model

Another method of thermal analysis has also been applied to obtain accurate values of temperature increases in the crucial components of the IPM motor. In this section, a 3D transient thermal analysis coupled to a 3D transient with thermal motion analysis is conducted to calculate the transient temperature. This method is not only restricted to the calculation of the magnetic field distribution but is extended to assess the temperature rise in the machine quantitatively. The interchange of energy between the electromagnetic and thermal fields is taken into consideration.

The design procedure used for the proposed thermal modelling is illustrated as a flowchart in Figure 3.4. This thermal modelling shows that when the required accuracy in electromagnetic design is reached, the proposed thermal model is implemented to calculate the temperatures of the various parts of the motor. The motor needs to be constructed first using JMAG software and then analysed. The losses obtained from the electromagnetic field analysis are used as the heat source in the thermal analysis.

During this part, a few design specifications have to be determined according to the output characteristics. The selection of appropriate configurations, materials, parameters, and initial guesswork should be accomplished. The output must follow the specifications with the smooth-running capability and satisfy the torque-speed requirements. The verification of overall performance is then achieved using finite element analysis (FEA).

Figure 3.3 below shows a flow chart used to simulate the designed machine for 3D transient electromagnetic analysis by using JMAG software.

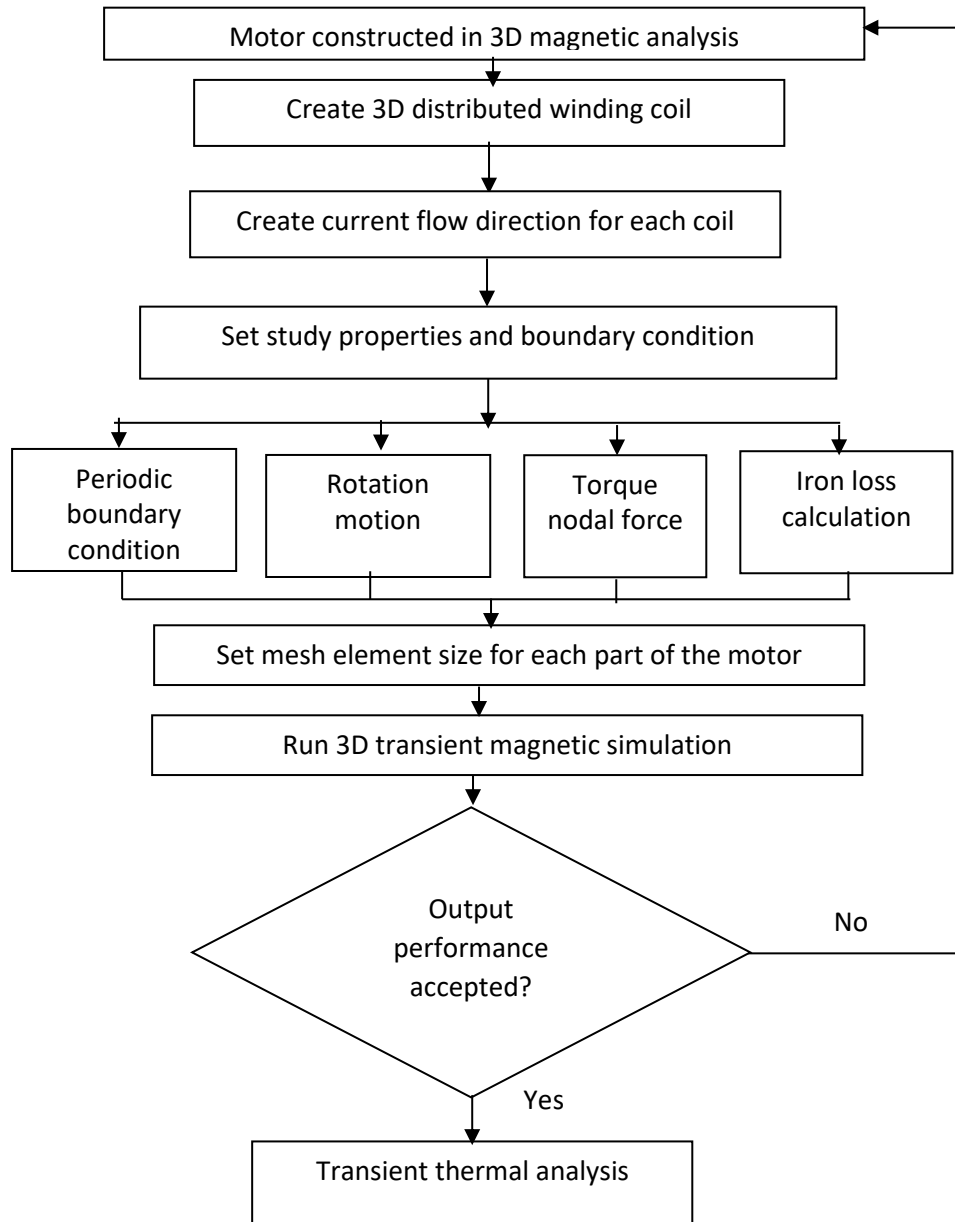


Figure 3. 3 Flow chart for 3D transient magnetic analysis

Then, the losses produced by the transient magnetic analysis will be used as a heat source for the transient thermal analysis. Figure 3.4 presents the flow chart for transient thermal analysis. If the simulation result is not acceptable, then the motor needs to be reconstructed again by using 3D transient magnetic analysis.

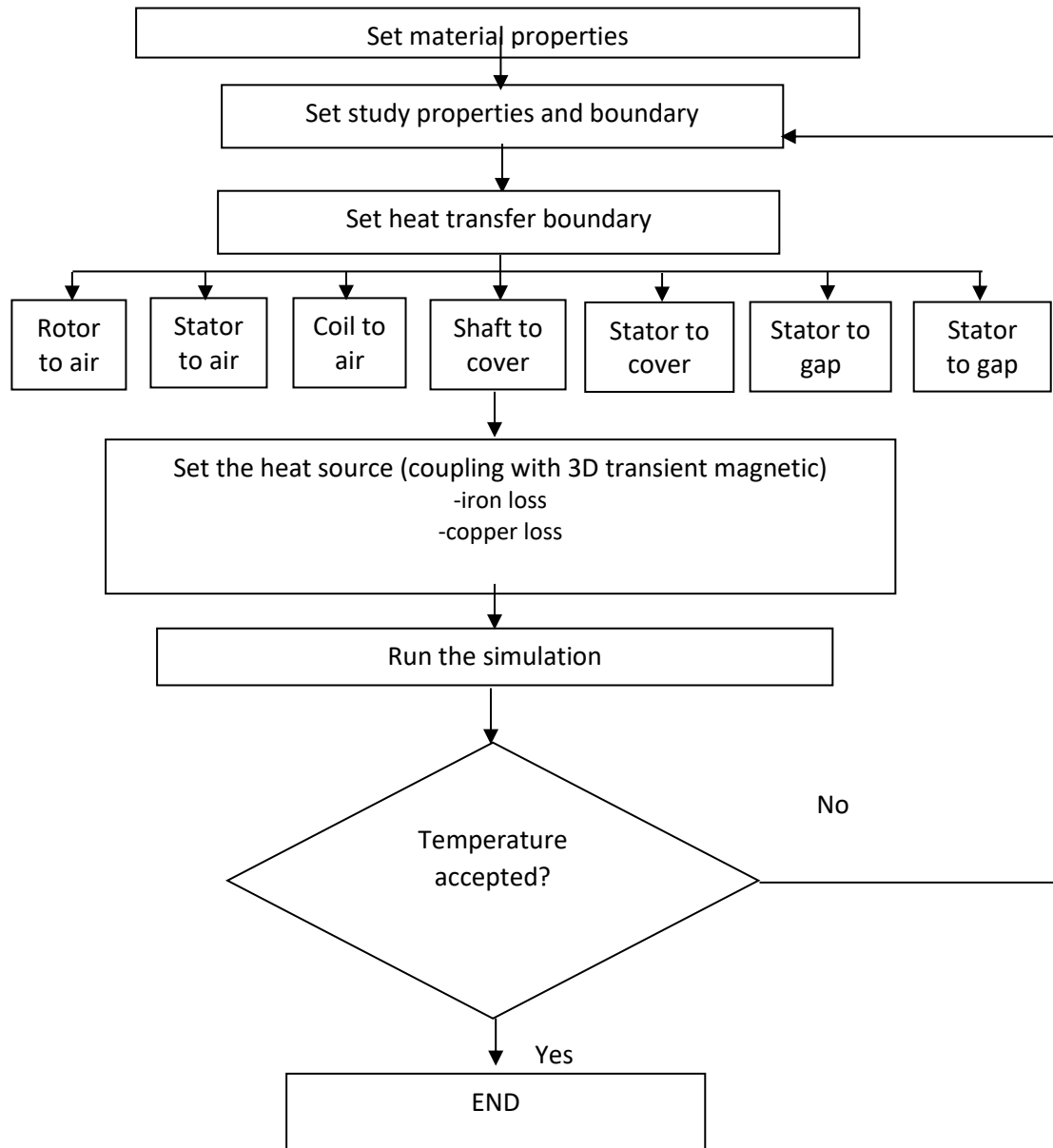


Figure 3. 4 Flow chart for transient thermal analysis

3.2.1 3D Transient Magnetic Analysis

It is crucial to choose the appropriate electrical and magnetic loadings and thus to select the optimum distribution of losses, as well as to select the most appropriate magnet material and grade. Moreover, when performing mechanical analysis, it is necessary to ensure that the material characteristics are modelled at the right temperature. For thermal analysis, the steps below are applied.

The heat source for a motor is mainly from copper loss in the coils and iron loss in the core. The 3D magnetic transient analysis will produce the heat source to carry out an accurate thermal design.

Few assumptions need to be done for the thermal analysis for IPM motor. Among them is the current flows through the coil is assume as a sinusoidal wave, the rotor moves rotational, and the cover surface is air-cooled. Also, the rotor is consisting of a rotor core, a magnet, and a shaft, and stator are consists of a stator core and a coil. The component of the 3D motor is, as shown in figure 3.5.

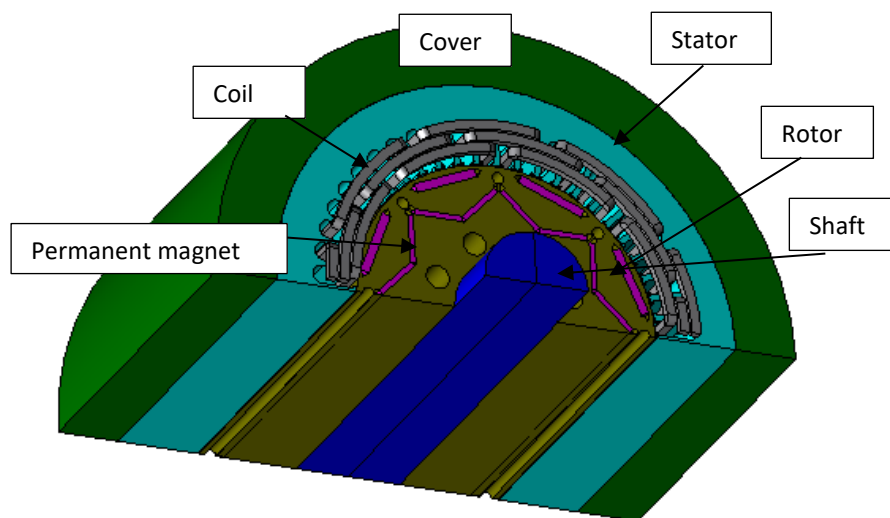


Figure 3. 5 3D IPM motor

Some of the materials are not applicable for thermal analysis. Therefore, to use the material needed, the thermal properties need to be added. One of the challenging parts is to create the 3D coil. Figure 3.6 shows the phase for the coil in the 2D design.

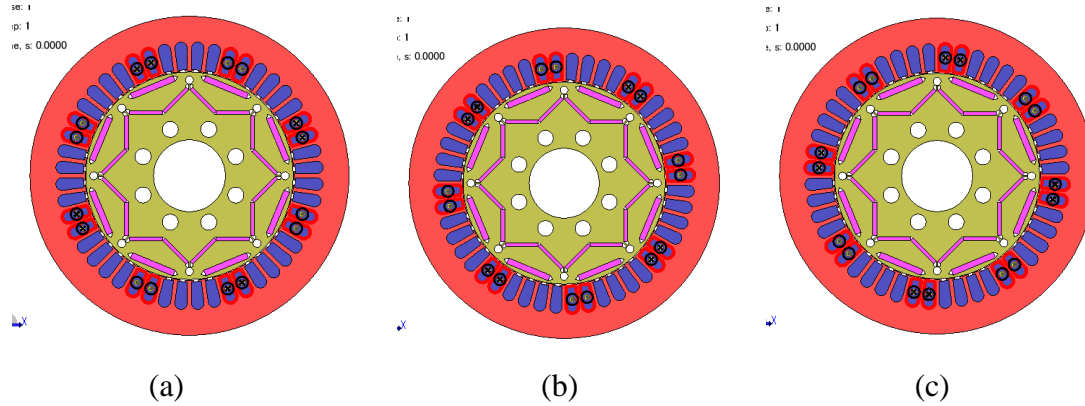


Figure 3. 6 2D winding configuration: (a) Phase U, (b) Phase V, and (c) Phase W

Therefore, for 3D design, the winding needs to be created according to the 2D winding configuration. Figure 3.7 presents the 3D distributed winding geometry.

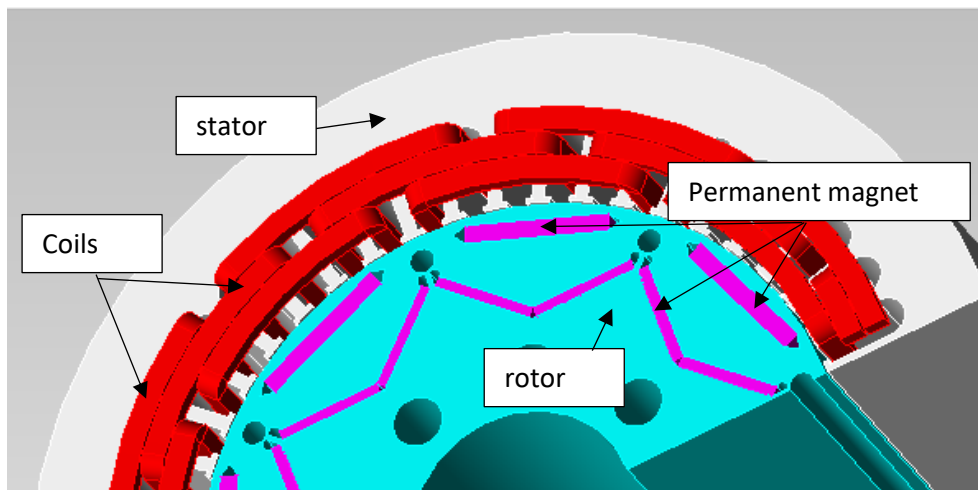
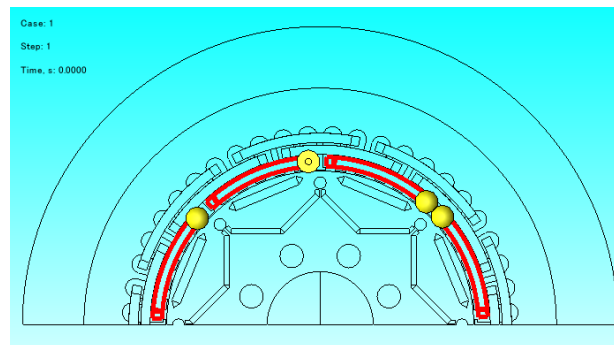
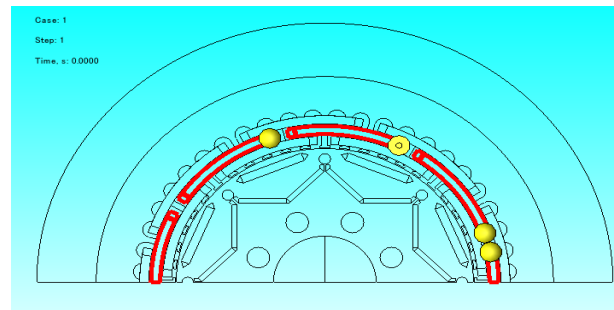


Figure 3. 7 3D distributed winding coil geometry

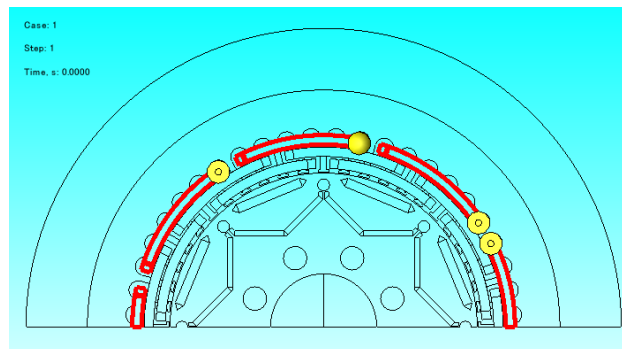
For 3D magnetic analysis, the flow of the current in the coil needs to be defined first. Figure 3.8 shows the flow of the distributed coil for each phase.



(a)



(b)



(c)

Figure 3. 8 Current flow direction for each coil; (a) Phase U, (b) Phase V, and (c) Phase W.

Since the coil winding will be one of the heat sources in the thermal analysis, to create the coils, it needs more attention. Besides, the setting for study properties and conditions such as periodic boundary condition, rotation motion, and torque: nodal force also need proper calculation. Iron loss calculation also needs to be set up during 3D magnetic analysis.

Before the simulation can be run, the mesh element size needs to be set up for each essential part. The size of the mesh for each part should be set differently and reasonably to satisfy the corresponding discrete requirements. Even the time step of the transient electromagnetic field simulation should also be set accurately according to the discrete level of the mesh [80]. Table 3.2 shows the element size selected for each part, and Figure 3.9 shows the motor after the mesh is generated. It took a few days to complete the 3D magnetic analysis since the file is too big.

Table 3. 2 Element size for each part of the motor

Motor part	Mesh element size
Rotor	2mm
Stator	2mm
Housing	3mm
Coil	2mm
Magnet	1mm
Air gap	1.1mm

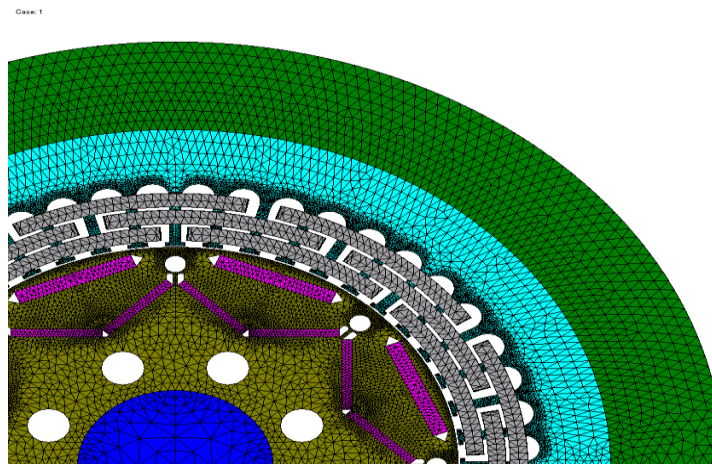


Figure 3. 9 Mesh element for the motor

3.2.2 Transient thermal analysis

For transient thermal analysis, the circuit diagram, as shown in Figure 3.10. The heat is transferred from the cover to the air and the shaft.

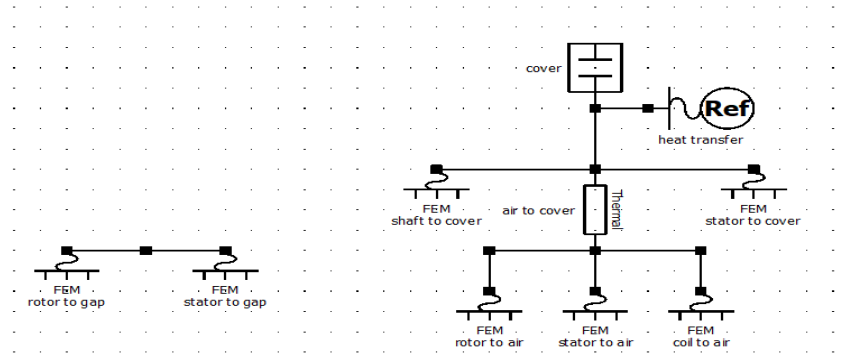


Figure 3. 10 Heat transfer circuit diagram

3.2.3 Convection heat transfer coefficient at the motor outer surface

Convection heat transfer is related to the outer air velocity. If the air velocity is 0 ~ 25 m/s, the heat transfer coefficient can be expressed as follows [81]:

$$\alpha = \alpha_0 + 4v \quad (3.3)$$

where α_0 is the convection heat transfer in calm air, and v is air velocity.

Three parts of the motor involve heat transfer to the air, rotor core, stator core, and coil winding. Figure 3.11 shows the heat transfer rotor to air. The surface on the rotor needs to be selected. Meanwhile, figure 3.12 and 3.13 show the heat transfer stator to air and coil to air, respectively.

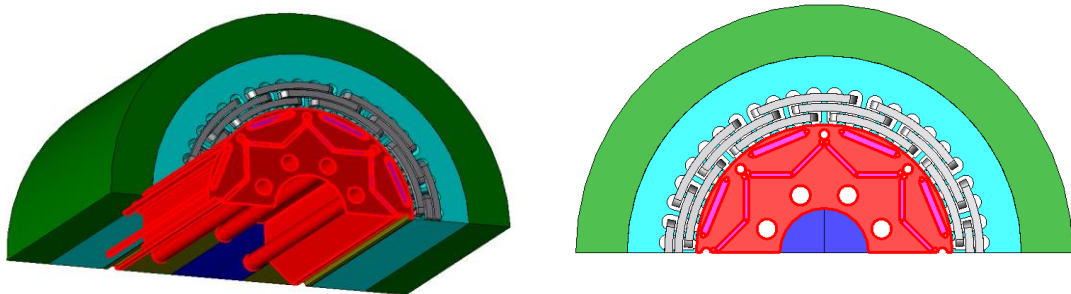


Figure 3. 11 Heat transfer rotor to air

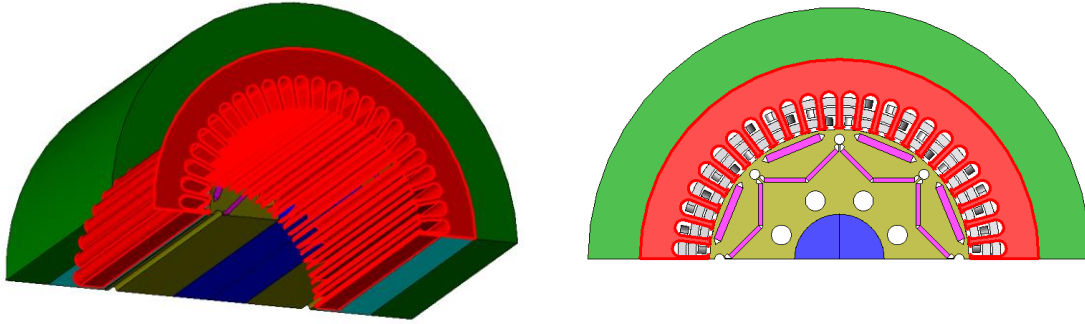


Figure 3.12 Heat transfer stator to air

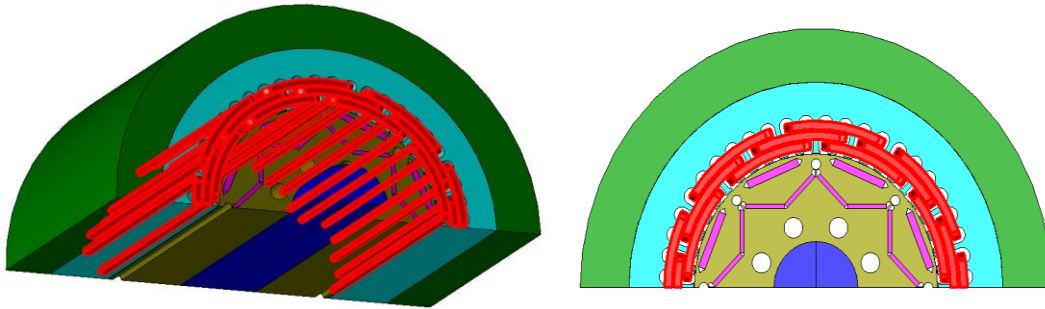


Figure 3.13 Heat transfer coil to air

3.2.4 Convection heat transfer coefficient in the air gap

When the motor is running, the rotation of the rotor will produce a flow of air through the air gap. Thus, the heat is transferred between the stator and rotor through the convection of air in the gap. As a result, the thermal field and fluid field are coupled together, which increases the difficulty of solving the motor temperature field. Figure 3.14 shows the heat transfer rotor to the air gap. Meanwhile, figure 3.15 presents the heat transfer stator to the air gap.

The equation for heat transfer coefficient is

$$h_1 = \frac{6.6 Vr^{0.67}}{10^5 lg^{0.33}} \times 10^4 \text{ (W/m}^2\text{/degC)} \quad (3.4)$$

where, Vr is rotor rotation speed in cm/s, and lg is gap length in cm.

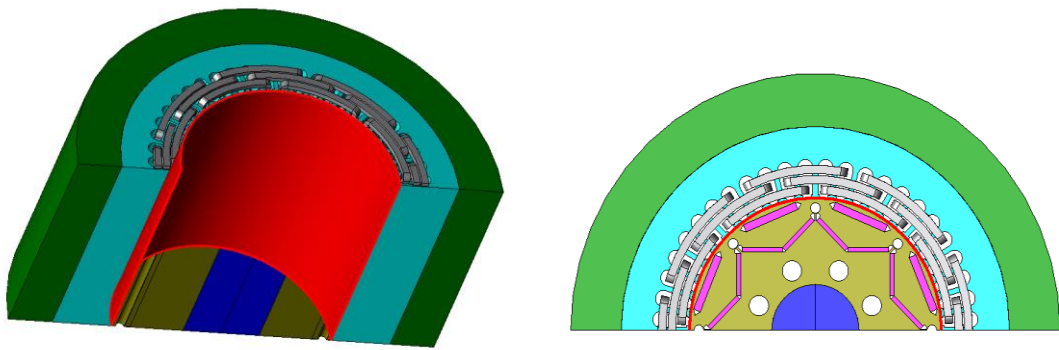


Figure 3. 14 Heat transfer rotor to the air gap

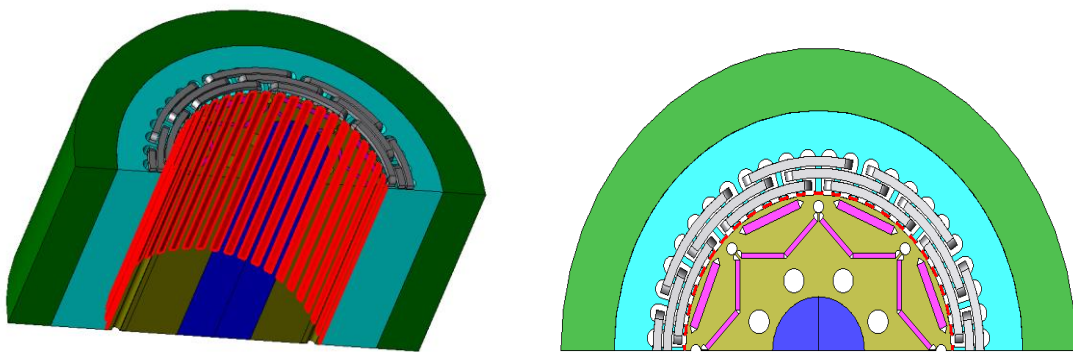


Figure 3. 15 Heat transfer stator to the air gap

Also, the coil winding phase U, V, and W, the permanent magnets, rotor, and stator, act as the heat source for the transient thermal analysis. The joule losses produced by permanent magnets and iron loss produced by rotor and stator in the 3D magnetic study will be the primary heat source

3.3 Summary

Two different types of thermal analysis have been studied to define the heat transfer for each essential part of the PM motor. Each method has advantages and disadvantages. The preference will be to do all analyses in a multiphysics environment linking finite electromagnetic elements and thermal elements in one operation to choose the better method for thermal analysis. For the lumped parameter thermal model, all resistances need to be calculated first, and by applying the value to MotorCAD software, the output will be

the temperature rise of the calculated part. The lumped parameter analysis can be used to get accurate values of temperature increases. The reason is, the temperature rise can be calculated for each region, depending on the thermal resistance that has been previously defined. The thermal field also can be analysed using thermal lumped parameters based on the eddy current loss derived using MotorCAD software. However, if FEA combining a 3D transient magnet and thermal analysis is applied, the problematic part only during the beginning of the machine design. The machine needs to be designed first, and a simulation has been conducted of the electromagnetic analysis. The values of losses obtained from the electromagnetic analysis act as the values of heat transfer for the thermal field analysis. Thus, the result of electromagnetic can be used directly to perform the thermal field analysis.

Chapter 4 Analysis of Motor Performance

This chapter will show the methodology used to construct the motor. As mentioned in Chapter 3, JMAG software will be used to design the motor to do the electromagnetic analysis. Then, the value of losses from the 3D transient analysis will be used as heat transfer in thermal analysis.

Besides, this chapter also will introduce the benchmark motor, which is used as a reference motor in this study. The motor must be used as a reference to make sure that the required output from the motor design can be achieved at least as same as the reference motor. In this study, the benchmark motor is used as a reference in designing the stator and rotor topologies. Other than that, the proposed motor should achieve the required output as performed by the benchmark motor. The main objective of this study is to find the smallest size of motor. The methods to accomplish the main aim of this study will be discussed in this chapter. The size of the motors will be reduced gradually by 5% from the original size of the benchmark motor to come out with significant results.

Even though the IPM has been used widely, the usage of permanent magnets has become a severe issue because their cost is steadily increasing. Therefore, the main objective of this research is to determine the smallest size of the IPM motor, which can maintain the level of electromagnetic performance, torque capability, and efficiency of the reference motor. Besides, the motor with new dimensions must run safely.

The latest demands for electrical motors are that they must be compact and light and have torque density required to tolerate environmentally and load conditions. Reduce the usage of permanent magnets has also become the main focus in designing a new electric motor, especially for electrical vehicle applications. Research has been conducted on three different sizes of motors. From the original dimension to progressively smaller ones: machines A, B, and C. At the beginning of motor design, the assessment of the electromagnetic performance of the motor and magnetization analysis have been conducted using JMAG software. Then, thermal analysis is applied to perform thermal static or transient analysis, either as stand-alone or coupled to static or time-harmonic since the temperature is a major factor threatening the magnetism of magnets and the life and stability of machines.

4.1 Design Methodology

By using finite element analysis, the temperature rise of the motor can be derived directly from the electromagnetic output of the simulation, where the values of the losses obtained from the electromagnetic analysis act as the values of heat transfer for the thermal field analysis. Thus, the result of the electromagnetic analysis can be used directly to perform the thermal field analysis.

The steps taken to achieve the main objectives are as shown in figure 4.1. Nissan Leaf motor was used as a reference to design the motor. From the original size as benchmark motor (BMM), the size of the motor was reduced until the most suitable size was found. For each step, the size of the machine was reduced 5% smaller from the previous size because it will show more significant results. At first, the motor will be designed by following topologies and specifications that have been decided. Then, the electromagnetic analysis will be conducted on the motor designed. If the required output is achieved, then thermal modelling will be applied to the motor. If the temperature is still within the accepted range, then the size of the motor will be reduced for another 5% from the previous one. However, if the temperature was high, this means that the size of the motor could not be reduced further.

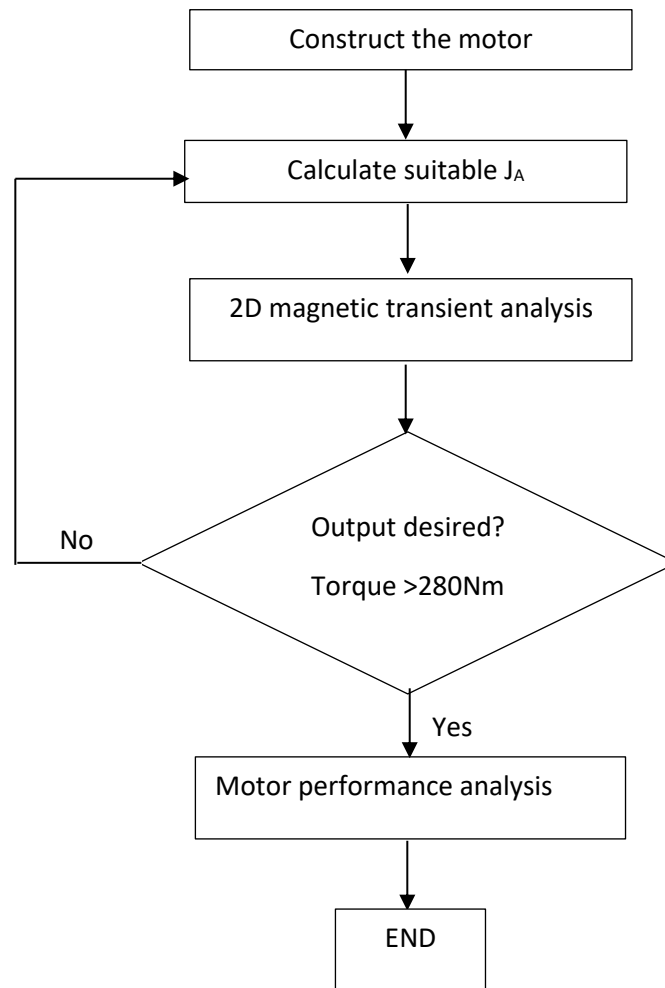


Figure 4. 1 Flow chart of motor design

4.2 The Nissan LEAF

The Nissan Leaf interior permanent magnet (IPM) motor, which was released in December 2010, is used as the benchmark in designing the PM motor to satisfy the requirements of electric vehicle applications. The Nissan Leaf's motor achieves high power and efficiency and uses water as a coolant, which is applied in parallel as a water jacket. Table 4.1 below shows the specifications and performance of this motor.

Table 4. 1 Specifications of Nissan LEAF

Maximum power	80 kW
Maximum torque	280 Nm
Maximum AC	425 A _{rms}
Efficiency	Nearly 95%
DC Voltage	240-403V

Nissan LEAF has an inner rotor and outer stator. The rotors are laminated with M270-35A non-oriented silicon steel with buried permanent magnets. Neodymium iron boron (NdFeB) is used as permanent magnet material, and the machine has eight poles in the rotor. Nissan LEAF has 3 magnets per pole arranged in an inverted triangle shape, and the winding arrangement in stator-embedded 3-phase distributed winding. Figure 4.2 shows the features of the Nissan LEAF.

Table 4. 2 Motor topology and major dimensions

Outer diameter of stator	198.2	mm
Inner diameter of stator	131	mm
Stack length of stator	151	mm
Outer diameter of rotor	130	mm
Inner diameter of rotor	45	mm
Large magnet dimensions	3.79 (DOM) x 28.85 x 8.36*	mm
Small magnet dimensions	2.29 (DOM) x 21.3 x 8.34	mm
Number of slots	48	
Number of poles	8	
Winding type	Full pitch single layer distributed winding	
No. of turns per coil	6	
No. of strands per turn	15	
Diameter of copper wire	0.812	mm
Total magnet mass	1.8954	kg

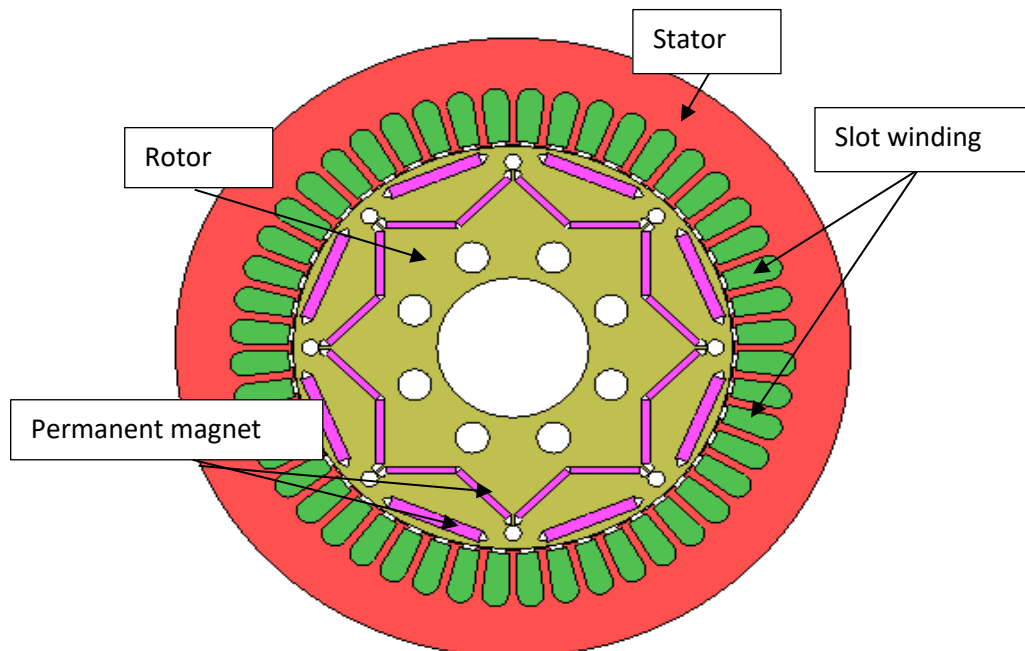


Figure 4. 2 The Nissan LEAF

4.3 Proposed Motor Parameters and Characteristics

Even though the motors are of different sizes, some aspects of motor topology are almost the same for all motors such as the number of rotor poles, number of rotor magnets, magnet arrangement, and stator and rotor lamination material as shown in Figure 4.3. The parameters of the motors are reduced by 5% each time to find the suitable size of the motor. However, for each motor, the total number of poles is maintaining eight, and each pole has six slots. For rotor and stator lamination material, M270-35A is used, and NdFeB has been used as the magnet material. Table 4.3 shows the parameters for each motor [42].

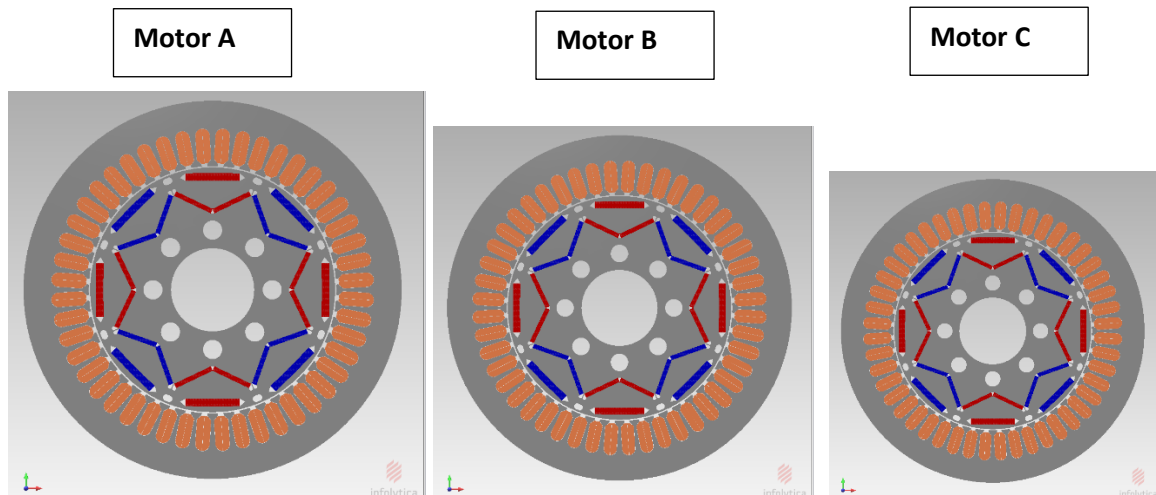


Figure 4. 3 Different sizes of IPM motors

Table 4. 3 Parameters of the IPM motors

Parameters	Motor A	Motor B	Motor C
Stator outer diameter (mm)	198.2	188.3	178.38
Stator inner diameter (mm)	131	124.5	117.9
Rotor outer diameter (mm)	130	123.5	117
Rotor inner diameter (mm)	45	42.75	40.5
Air gap (mm)	0.9	0.86	0.81
Machine length (mm)	151	143.45	135.9

4.4 Electromagnetic Performance

4.4.1 Magneto-motive Force (MMF)

Also known as magnetic potential, magneto-motive force is the property of certain substances that give rise to magnetic fields. MMF value is equal to the total current applied, I multiplied by the number of turns in the coil, N .

$$MMF = NI \quad (4.1)$$

In general, rotor flux and a stator MMF have to be present, which are stationary concerning each other but having a nonzero phase shift between them to produce electromagnetic torque. Different MMF values were injected in the stator winding to get the desired output. Figure 4.4 shows the amount of current needed for the IPM motors to gain a torque of 280Nm and 80kW power. Theoretically, to maintain torque capability and power, a smaller motor needs higher current. Therefore, different values of current are applied to each motor. As shown, motor C needs the highest value of current and number of turns. Meanwhile, the second-highest current value was for motor B.

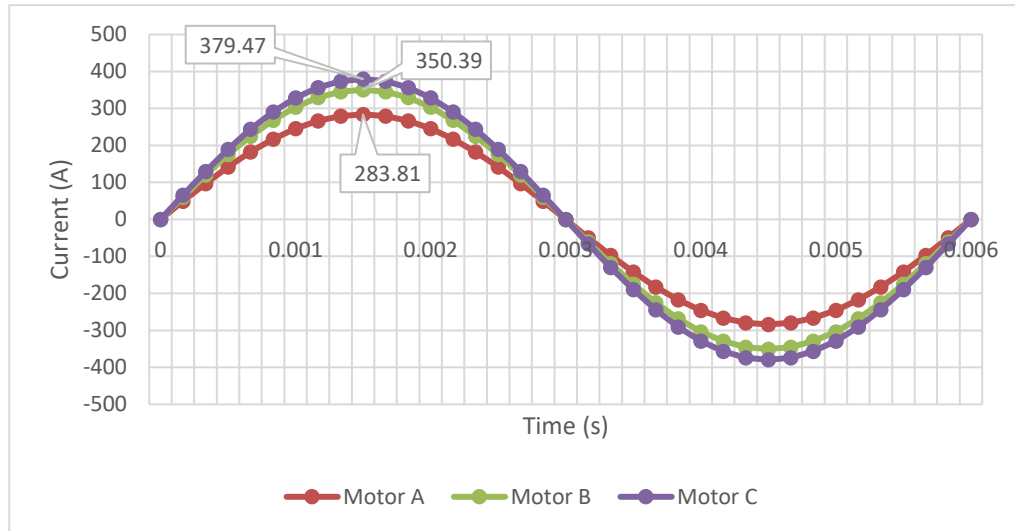


Figure 4. 4 Circuit current for each IPM motor

The number of turns for the slot winding is different for motor C. To achieve the desired torque, motor C needs a higher number of turns. Therefore, motor C has 10 number of turns while motor A and motor B have 6 number of turns.

Table 4. 4 Number of turns for each IPM motor

	Number of turns (N)
Motor A	6
Motor B	6
Motor C	10

Generally, the value of the current is proportional to torque. Increasing the current value will add more torque. However, only specific amounts of current can be chosen since it will affect the temperature increase in the motor. With the selected MMF values, all IPM motors achieve the desired torque and power. If the same MMF value is applied to the stator winding for all IPM motors, the smaller motors will have lower mean torque compared to the reference motor. It can be concluded that smaller motors need higher MMF to gain the same torque and power output.

4.4.2 Flux Linkage and Magnetic Flux Density

Figure 4.5 shows the flux linkage for Motor A. The magnetic field in the stator teeth over the magnets is mostly uniform and in the normal direction.

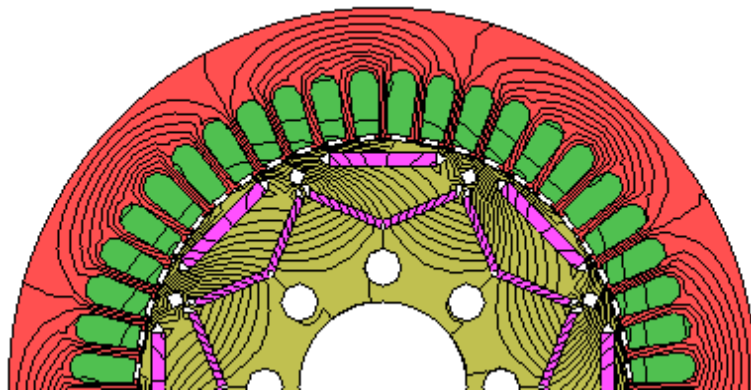


Figure 4. 5 Flux linkage for motor A

Since the parameter and size for motor B are just 5% smaller than motor A, therefore, there is no significant difference in the magnetic flux density for both motors. The minimum value of magnetic flux density is at the stator core, and the maximum value is at the edge of the permanent magnet. The magnetic flux density is as shown in Figure 4.6.

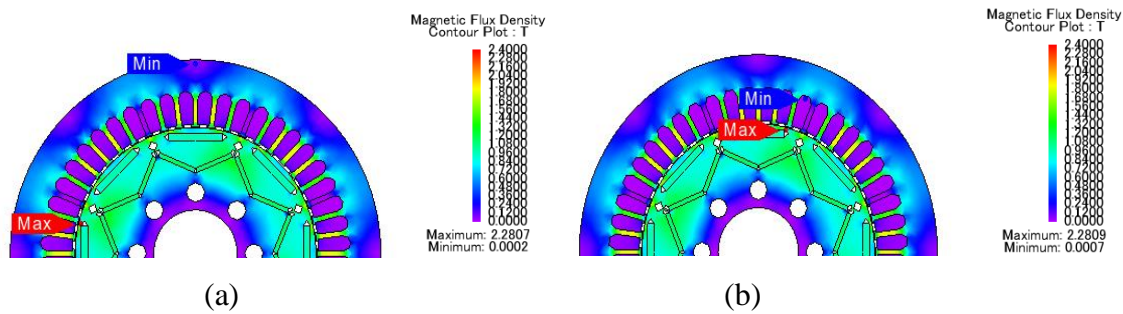


Figure 4. 6 Magnetic Flux density: (a) Motor A, and (b) Motor B

On the other hand, motor C has a 10% reduction from the original size, and the parameter of the Nissan LEAF produces slightly higher magnetic flux density, as shown in Figure 4.7.

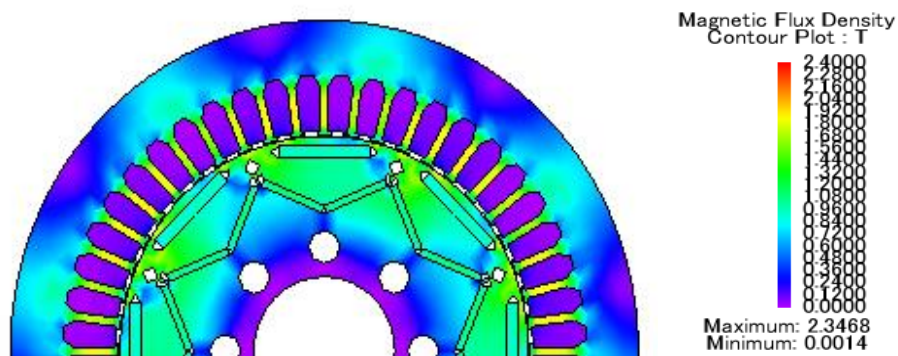


Figure 4. 7 Magnetic Flux density for motor C

4.4.3 Cogging Torque

Cogging torque occurs due to the interaction between the permanent magnet and the stator tooth. Typically, the IPM motor produces slightly higher torque density per unit volume than other motors. It is happened due to the combination of magnet torque and reluctance torque. The structure of the IPM motor itself in which the permanent magnet is embedded in the rotor. Figure 4.8 presents the cogging torque for three different sizes of the IPM motor. Motor A and motor B have more torque ripples, and motor A produces the highest cogging torque, among others.

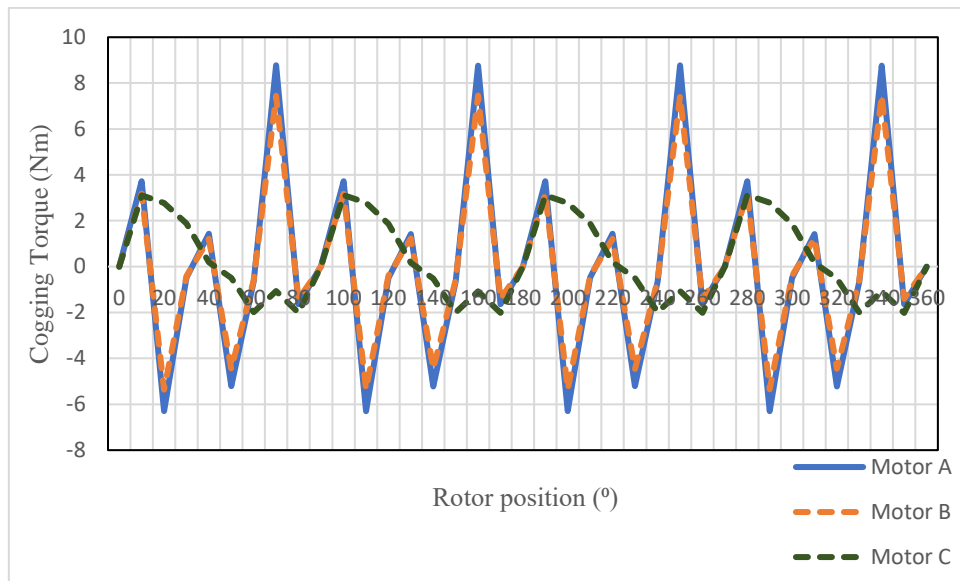
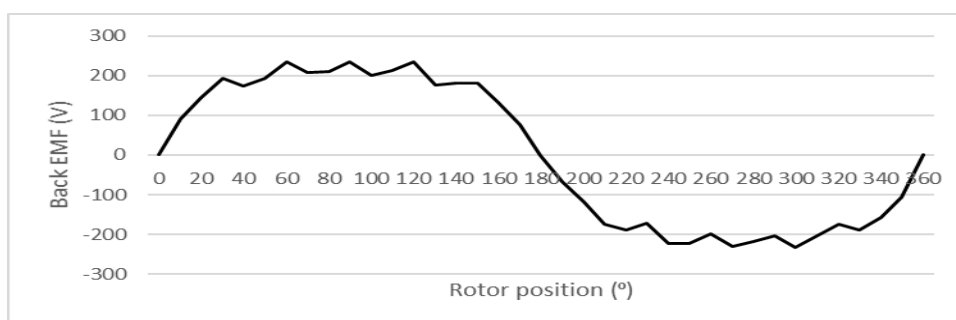


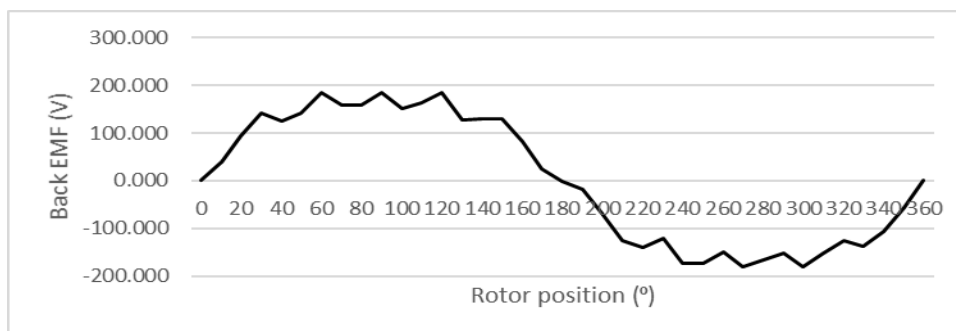
Figure 4. 8 Cogging torque for each IPM Motors

4.4.4 Back EMF

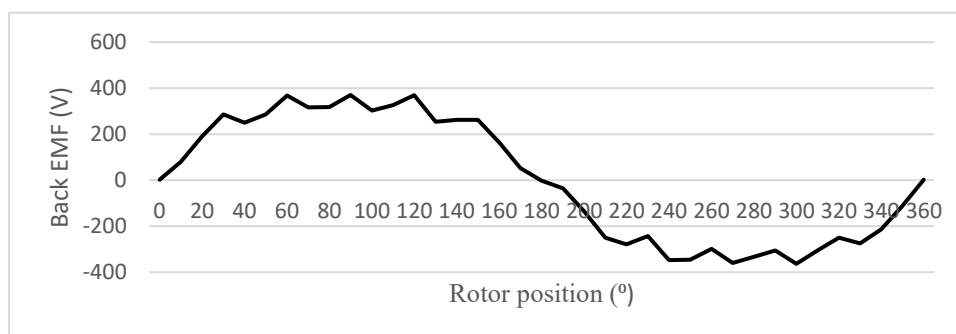
The back-EMF waveforms were obtained from a transient with a motion model for the various sizes of IPM motors and are shown in Figure 4.9. Motor A produced higher peak back-EMF than motor B since both motors have the same number of winding turns. The smallest, Motor C, was wound with a higher number of turns and needed higher current to achieve the desired torque. Therefore, Motor C produced the most elevated peak back EMF.



(a)



(b)



(c)

Figure 4. 9 No-load back-EMF: (a) Motor A, (b) Motor B, and (c) Motor C

4.4.5 Torque Vs Armature current density, J_A

Motor A and B are using the same number of turns. Therefore, the torque values for various J_A are higher for motor A than motor B, as shown in figure 4.10. Motor A produced the desired output torque during 25 A/mm^2 . Meanwhile, motor B needs at least 30 A/mm^2 to achieve the torque value as same as the benchmark motor.

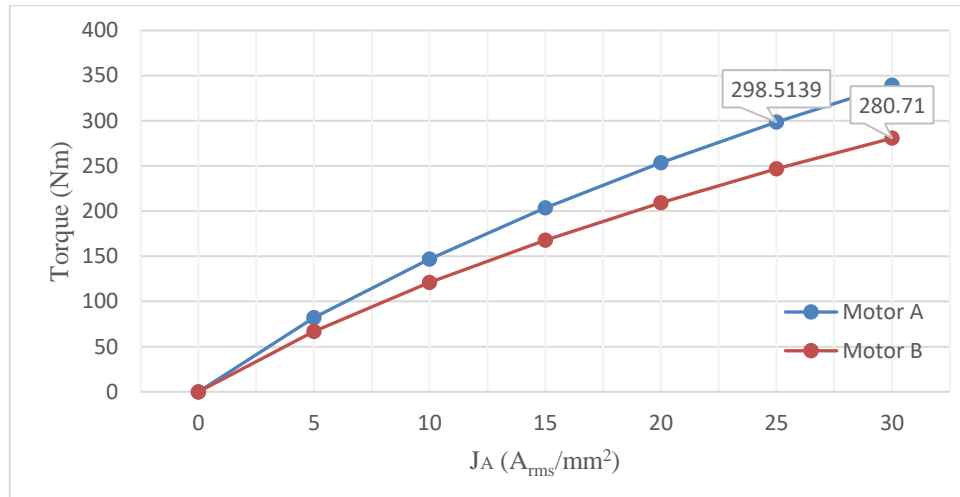


Figure 4. 10 Torque for various J_A for Motor A and B

Motor C was injected with higher current density, J_A , and the number of turns was 10. Motor C is capable of producing the torque more than 280 Nm at $J_A = 25 \text{ A}_{\text{rms}}/\text{mm}^2$. Figure 4.11 presents the torque value for various J_A for motor C. This result shows that motor C can work adequately in the range of selected J_A .

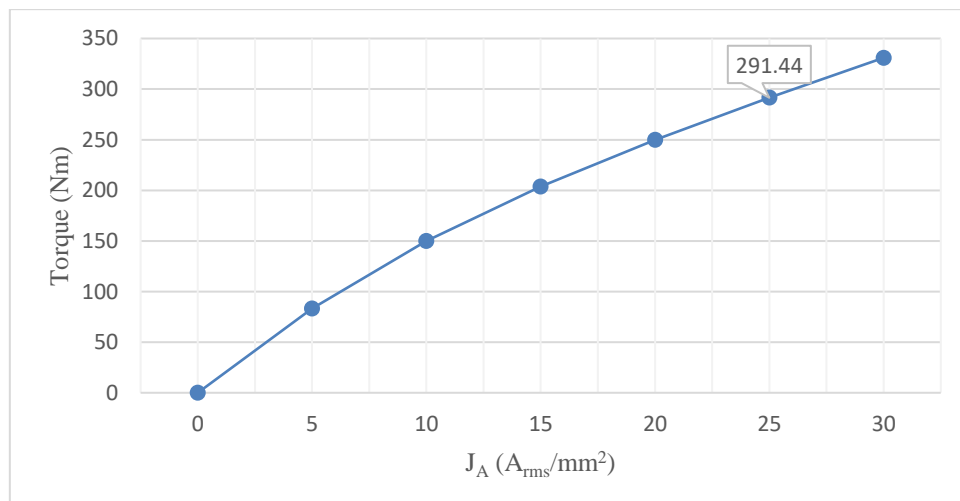


Figure 4. 11 Torque at various J_A for Motor C

4.4.6 Magnet Mass

Each motor needs three permanent magnets per pole arranged in an inverted triangle shape, and the total number of permanent magnets used is twenty-four. Two permanent magnets are opposite each other at an angle of 128° , and they have the same mass and size. Meanwhile, another permanent magnet with a different mass and size is located opposite the other two magnets. NdFeB has been used as the permanent magnet in these motors. The value of density for NdFeB is 7550 kg/m^3 .

Smaller motors will have permanent magnets of smaller size. Therefore, the total mass of the magnets used will decrease. The magnet mass for PM motors with NdFeB and the parameters of the magnets for each machine are shown in table 4.5. The mass is reduced significantly. Consequently, the cost also decreases.

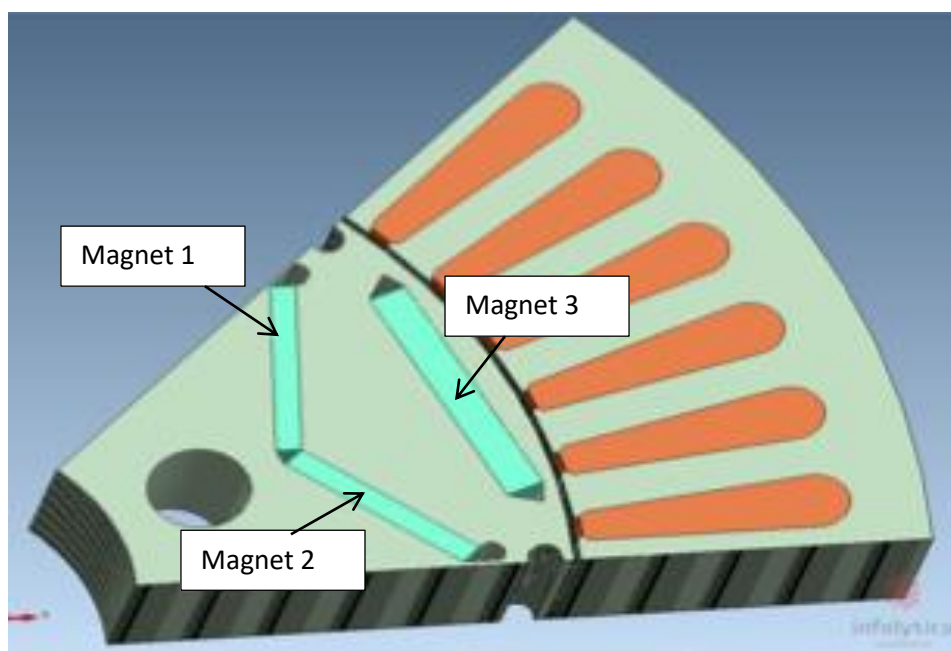


Figure 4. 12 Rotor topologies of IPM machines

Table 4. 5 Dimensions of permanent magnets (NdFeB)

	Magnet 1 & 2		Magnet 3		Total Magnet Mass
	Dimension (mm)	Magnet Mass (g)	Dimension (mm)	Magnet Mass (g)	
Motor A	2.29 x 21.3 x 8.34	0.0544g x 16 = 0.8704	3.79 x 28.85 x 8.36	0.1245g x 8 = 0.9966g	1.867 kg
Motor B	2.17 x 20.24 x 7.92	0.049g x 16 = 0.786	3.6 x 27.41 x 7.94	0.1102g x 8 = 0.8818g	1.668 kg
Motor C	2.06 x 19.17 x 7.51	0.0441g x 16 = 0.7055g	3.41 x 25.97 x 7.52	0.1004g x 8 = 0.8031g	1.509 kg

4.5 Thermal analysis on Motor A

Thermal analysis is performed using the loss obtained with magnetic field analysis as the heat source. It is crucial to predict the temperature rise in a motor to make sure the motor can run safely.

Copper loss and iron loss are considered to be most important in motor analysis because they constitute more than 90% of the total losses [9]. Figure 4.13 shows the power losses for all IPM motors. The performance of each motor should be able to reach the same level as that of the original Nissan LEAF motor, 280Nm and 80kW for the torque and power, respectively. Therefore, the smaller motor needs higher current, and, for this reason, the copper loss will increase, which will consequently affect the temperature rise in the motor. Despite this, the iron loss is reduced slightly in smaller motors, but the total loss is still higher than in bigger motors.

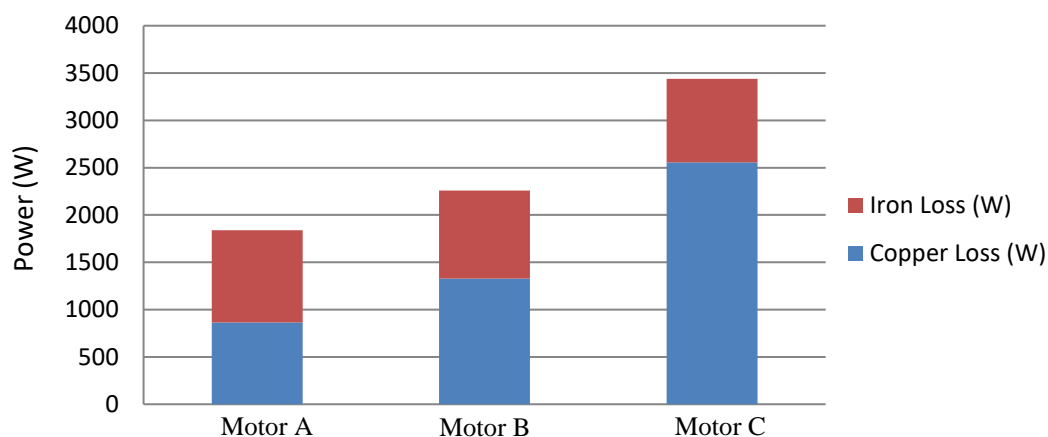


Figure 4. 13 Losses for IPM motors

The losses produced by the transient magnetic analysis will be used as a heat source for the transient thermal analysis. The detailed explanation as in Chapter 3. Figure 4.14 shows the temperature rise in motor A with NdFeB as a permanent magnet. The coil temperature is referring to end-winding temperature since it was the hottest part of the coils. The main concern was on the coils and permanent magnet. The temperature of the coils was below 95°C and 85°C for the permanent magnet. That means the temperature is not over the limit.

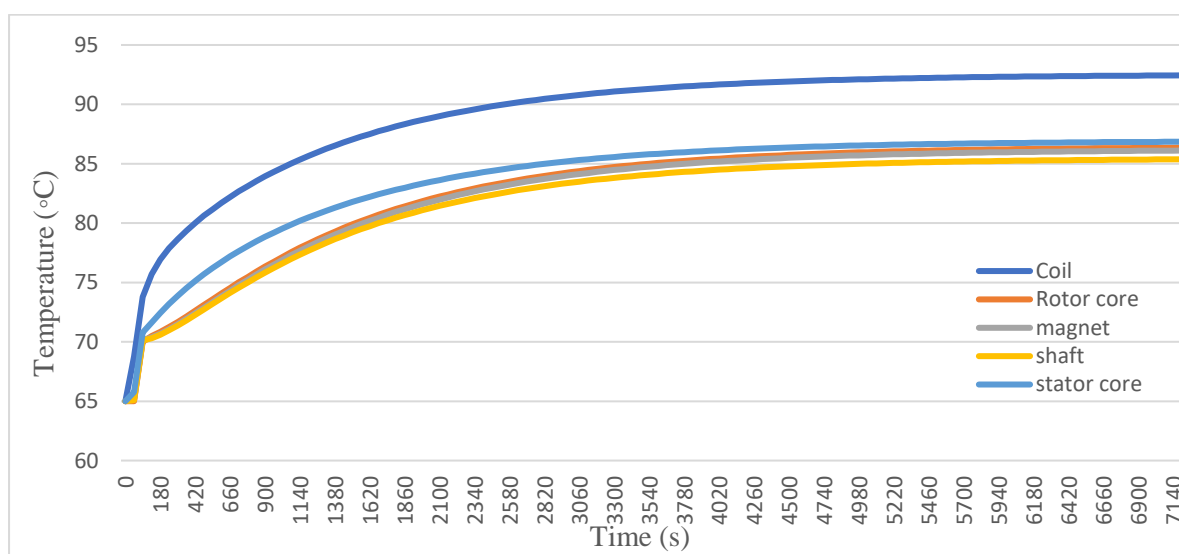


Figure 4. 14 Temperature variations in Motor A.

4.6 IPM Motor Adopted Concentrated Winding

For this section, simulation has been done on the winding configurations to find out either the concentrated winding (CW) is suitable winding configurations for the motor that has been proposed or not. The original Nissan LEAF motor is constructed with a distributed type of winding. In this study, two PM motors, eight poles, and 12 slots with the same rotor topologies are created. Both are constructed with a concentrated winding. The difference in the machines is the slot shape: The first one has an open slot type, and the second is the semi-closed slot type. Most of the significant parameters for the machines are identical, apart from the number of stator slots and the winding structure, so that the effect of winding configuration on machine performance can be easily observed. The features of the IPM motors are as shown in Figure 4.15, and the main parameters are as shown in Table 4.6.

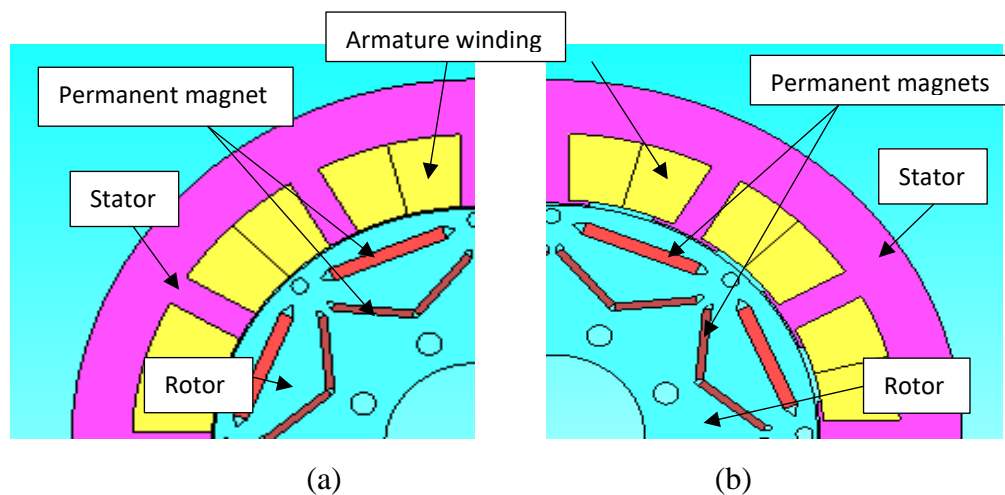


Figure 4. 15 FEA configurations CW IPM motors (8 poles 12 slots): (a) open slots; b) semi-opened slots

Table 4. 6 Parameters of the CW IPM Motors

Stack length	151	mm
Stator outer diameter	198	mm
Stator inner diameter	131	mm
Rotor outer diameter	130	mm
Rotor inner diameter	45	mm
Series of turns per phase	42	
Base speed	500	rpm

4.6.1 Slot dimensions

Different numbers of slots give different slot dimensions for each motor. Motor constructed with distributed winding has the smallest slot area. Meanwhile, the PM motors with the concentrated windings have more room for conductors. Figure 4.16 illustrates the dimensions of the open and semi-closed slots, and the dimensions are given in Table 4.7.

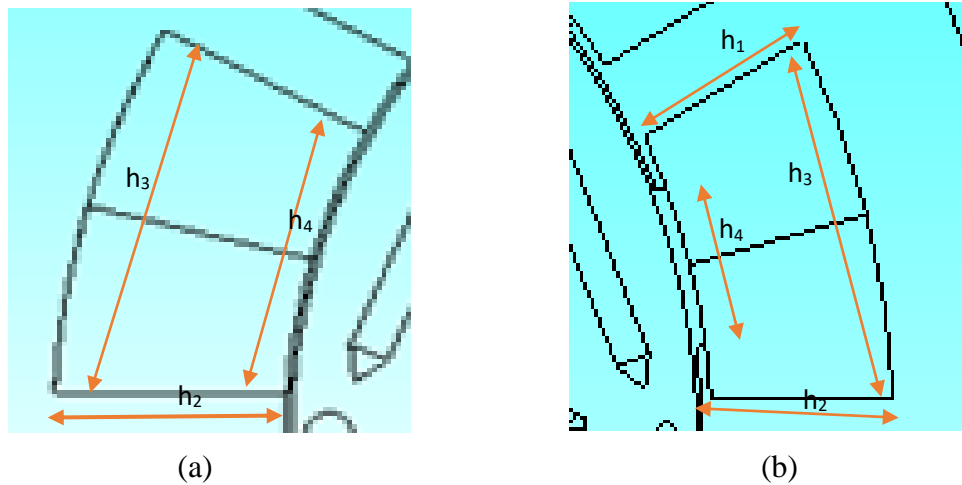


Figure 4. 16 Slot dimension for (a) open slot CW IPM motor and (b) semi-closed CW IPM motor

Table 4. 7 Slots Dimensions

CW IPM Motor		open slot winding	semi-closed winding
Shank length (mm)	h_1	-	16.627
Slot depth (mm)	h_2	19.75	19.75
Slot width (mm)	h_3	25.99	26.5
Tooth gap width (mm)	h_4	25.99	15.81
Conductor area	mm^2	618.79	592.38

4.6.2 Winding Layout and Connection

The windings for the CW IPM motors are shown in Figure 4.17. Both open and semi-closed concentrated winding motors have a more compact design because of the simple and short end windings. The consumption of copper is also significantly decreased when the concentrated winding is adopted.

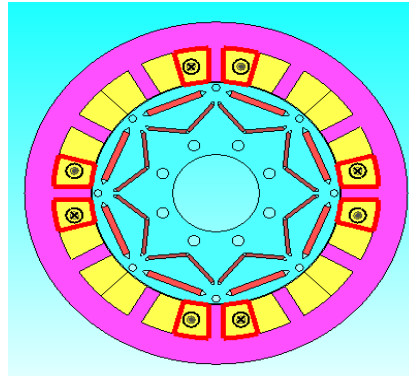


Figure 4. 17 Winding Layout for CW IPM motor phase 1 (U)

4.6.3 Back EMF

Back EMF or induced EMF of both CW IPMSM motors have been analysed at no-load test condition. The no-load back electromotive force (EMF) of the IPMSM Concentrated Winding Open Slot and Semi-Closed Slot are illustrated in Figure 4.18 and 4.19. It can be seen that the waveforms obtain from open slot concentrated winding motors are much more sinusoidal than that semi closed concentrated winding motor. These results imply that an open slot concentrated winding motor can offer much less torque ripple than semi closed concentrated winding.



Figure 4. 18 Back EMF for open slot CW IPM Motor



Figure 4. 19 Back EMF for semi-closed slot CW IPM motor

4.6.4 Cogging Torque

Cogging torque is a kind of pulsating torque, which can cause vibration and noise, and it always exists to some extent in IPM motors. The topology of the IPM motor greatly influences the cogging torque. For IPM machines, cogging torque consists of electromagnetic and reluctance components:

$$W(\alpha) = \frac{1}{2\mu_o} \int_v B^2 dV \quad (4.2)$$

where B is the flux density in the air gap of the machine and μ_o is the permeability of air. From the derivation of the partial differential of magnetic energy $W(\alpha)$, the cogging torque can be expressed as follows:

$$T_{cog}(\alpha) = -\frac{\partial W(\alpha)}{\partial \alpha} \quad (4.3)$$

where α is the angle of the rotor's position.

Cogging torque for CW open and semi-closed slot winding IPM motors as shown in Figure 4.20 and 4.21. Cogging torque for semi-closed slot winding is higher than open slot winding.

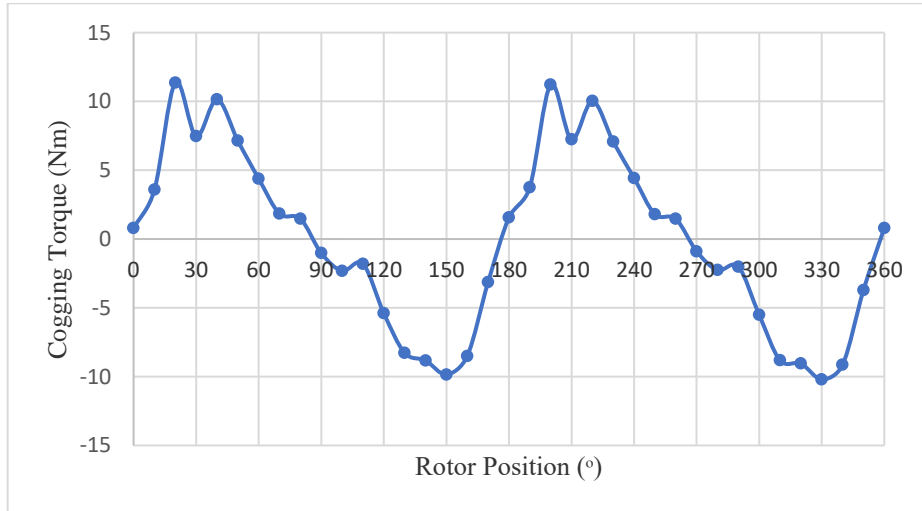


Figure 4. 20 Waveform of cogging torque for the open slot CW IPM motor

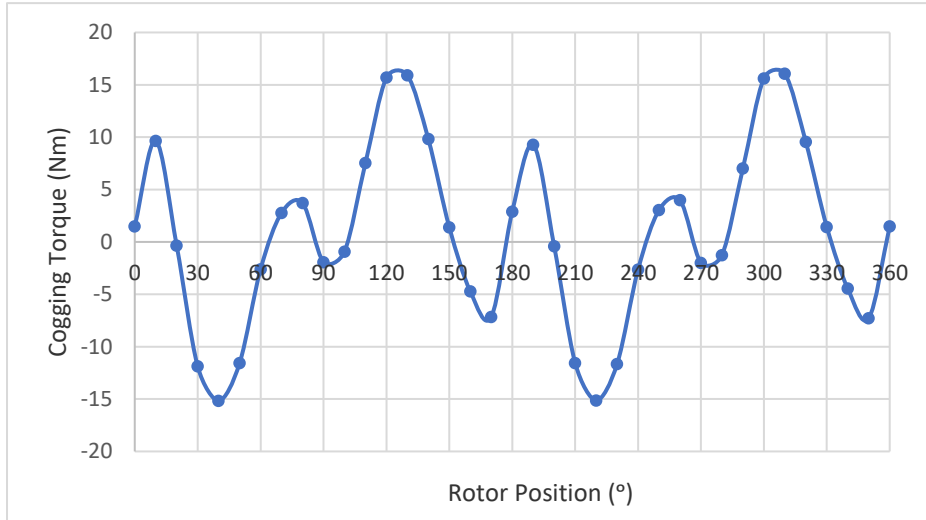


Figure 4. 21 Waveform of cogging torque for the semi-closed slot CW IPM motor

4.6.5 Load Test Comparison

Due to different values of armature coil slot area for open slot and semi-closed slot winding as mentioned in table 4.3, therefore there are different values of current density; J_A is injected to the motors. The strength of the armature current varies from 0 to 30 A_{rms} / mm^2 during the load test. The current maximum density value is set based on Equation 4.4 with this requirement.

$$I_A = \frac{\sqrt{2} J_A \alpha_A \delta_A}{N_A} \quad (4.4)$$

I_A = Injected current coil value, A(peak)

J_A = Armature coil current density, A_{rms}/mm^2

α_A = Armature coil filling factor (set to 0.5)

δ_A = Armature coil slot area

N_A = Number of turns

The value of current density, J_A that has been injected into the coil of the motors are as shown in Figure 4.22 and 4.23. The armature coil slot area for open slot CW IPM motor is slightly bigger than semi-closed slot CW IPM motor, therefore, the armature coil current density for open slot CW IPM motor is higher than the semi-closed CW IPM motor. Both motors are

wound with 42 number of turns. The highest current density ($J_A=30$) for CW open slot IPM motor is $312.54 \text{ A}_{\text{rms}}/\text{mm}^2$ while for CW semi closed slot IPM motor is $299.19 \text{ A}_{\text{rms}}/\text{mm}^2$.

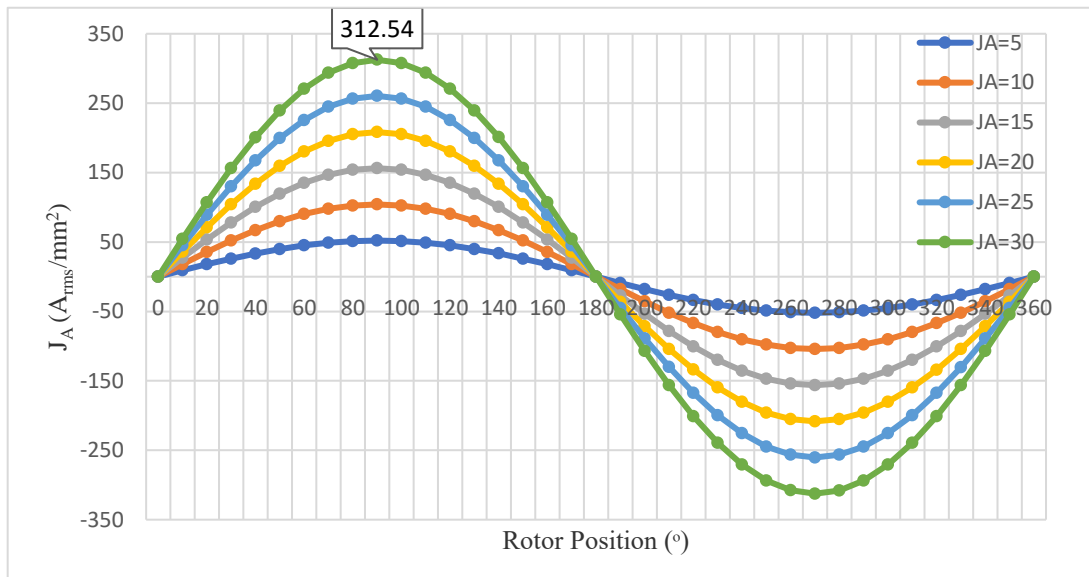


Figure 4. 22 Various current density, J_A for CW open slot IPM motor

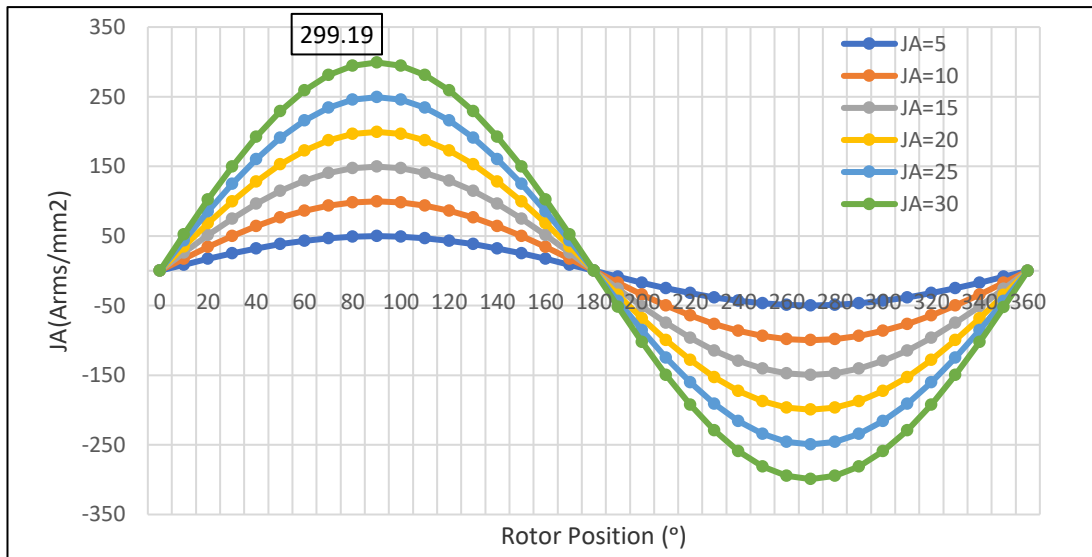


Figure 4. 23 Various current density, J_A for CW semi closed slot IPM motor

4.6.6 Peak electromagnetic torque with different current densities

Both motors are wound with 42 turns of coils. By injecting with a different value of current density, J_A , the amount of torque is increased significantly. As shown in Figure 4.24, the torque values for the semi-closed slot are higher than the open slot IPM motor. With the highest $J_A = 30 \text{ Arms/mm}^2$, the semi-closed slot IPM motor only capable of achieving 200.83Nm for the torque value. Meanwhile, the torque for open slot IPM motor is 171.92Nm during $J_A = 30 \text{ Arms/mm}^2$. Since the motors are purposely constructed to study the effect of the adopted concentrated winding, open and semi-closed slot, therefore there is no target torque and power.

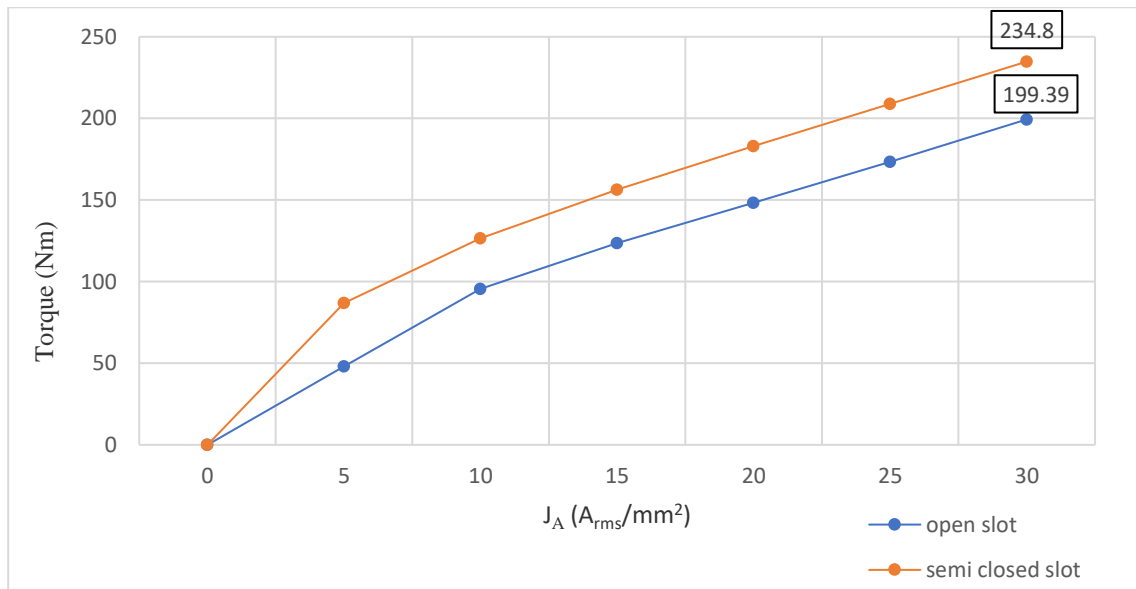


Figure 4. 24 Torque at various J_A .

4.6.7 Flux Linkage and flux distribution

Figure 4.25 shows the flux linkage for open slot and semi-closed slot CW IPM motors. Meanwhile, Figures 4.26 and 4.27 show the flux distribution at no load. It can be seen that the highest value of flux density for concentrated open slot winding motor is 2.2T, meanwhile, for concentrated semi-closed winding machine, the highest values are 2.4T. Consequently, both concentrated winding machines show lower flux density in the stator yoke. Smaller flux linkage in concentrated winding machines leads to the production of lower back-EMF and core losses. The leakage coefficient of machines with concentrated winding is generally larger than for

those with distributed-winding, which contributes to the reduction in output torque for a motor with a concentrated winding.

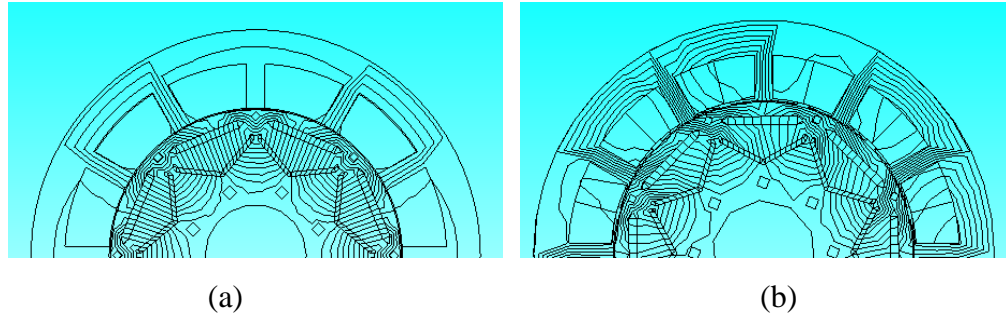


Figure 4. 25 Flux linkage for (a) open slot, and (b) semi-closed CW motor

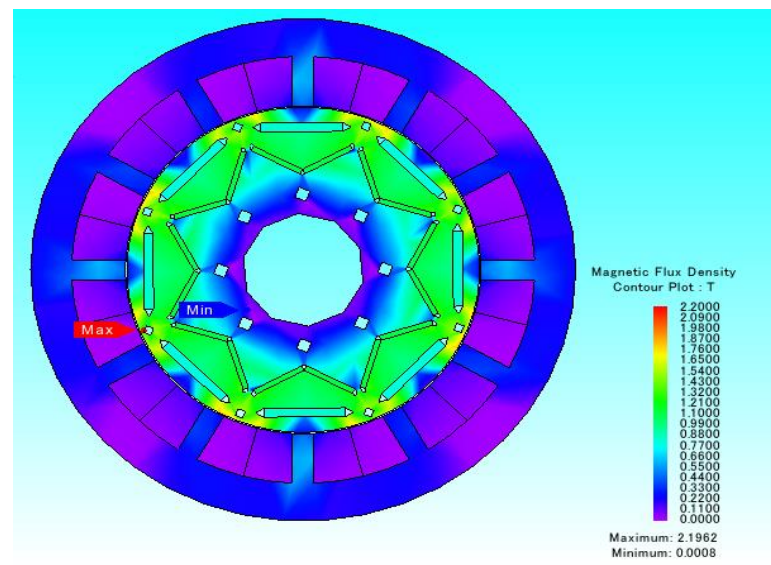


Figure 4. 26 Flux density distribution for open slot CW motor

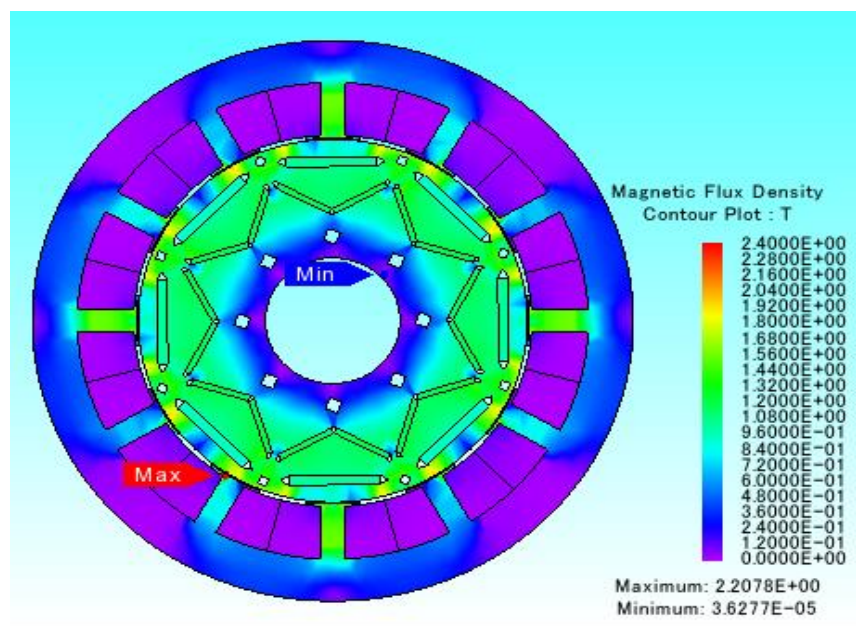


Figure 4. 27 Flux density distribution for semi-closed CW motor

4.6.8 Torque and Power vs. Speed at Various Armature Current Density, J_A

The torque and power versus speed characteristics of open and semi-closed CW IPM motors are shown in Figure 4.28 and 4.29. In each plot, the blue curve represents torque versus speed, while the orange line represents the power versus speed curve. Figure 4.28 shows that during the base speed 500rpm, the highest torque for open slot CW IPM motor is 200Nm, and the output power is 10kW. Meanwhile, the semi-closed CW IPM motor achieved the higher output torque. The torque value is 235Nm at the base speed of 500rpm. The output power peaked at 11kW, and as the speed reached its maximum at 3000rpm, the power gradually reduces to 9kW.

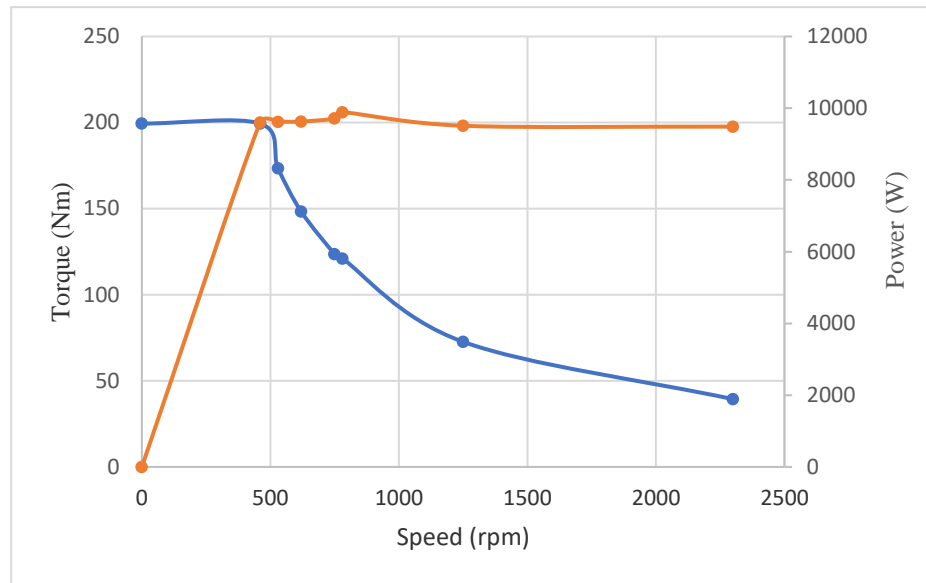


Figure 4. 28 Torque speed graph open slot CW IPM motor

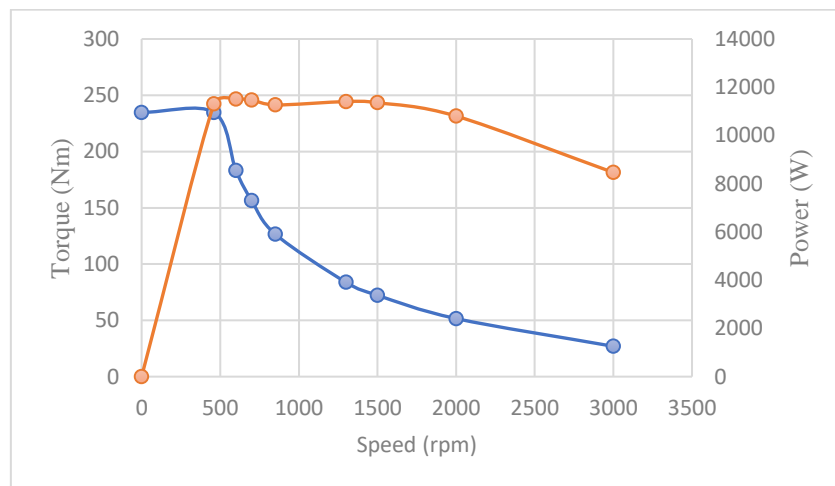


Figure 4. 29 Torque speed graph semi closed slot CW IPM motor

The performance of the CW IPM motor with an open slot and semi-closed slot winding have been comprehensively compared, and the following conclusions have been drawn:

- With the same current density, the motor with semi-closed slot winding can offer higher peak electromagnetic torque than the motor with open slot winding.
- The cogging torque for semi-closed winding is larger than the cogging torque for open slot winding.

However, to achieve the desired torque and power, CW IPM motors need higher current density compared to IPM motor adopted with distributed winding. The concentrated winding has short end turns, low cogging torque, and low stator core loss. In contrast, distributed winding motors offer their advantages in terms of higher reluctance torque, and thus lower magnet mass and lower rotor losses.

4.7 Summary

Motors of three different sizes have been simulated and analysed in terms of torque capability and output performance, starting from the original size (motor A) as a reference and followed by motor B and C of an increasingly smaller scale. All motors must achieve at least 280Nm torque requirements.

The original Nissan LEAF is adopted distributed winding. The results of the study indicate that the IPM motor can be designed with either an open slot or semi-closed concentrated winding. However, the motors need some in-depth research since the characteristic of torque-speed is not meet the specification.

Smaller motors need higher MMF, and power losses will increase. The findings have demonstrated that even when the machine is shrunk by approximately 10% of the original size, it can still give the desired output and can function properly. Compared to the original motor, the magnet mass of motor C can be reduced by 10%. Also, the temperature of the motor can be predicted directly using the output from the electromagnetic analysis without the need for any separate calculation of power loss. To have a smaller motor and can work accurately at a higher temperature, it can be improved by using higher temperature materials for the rotor and stator laminations, permanent magnet and coils. In the next chapter, the simulation results using higher temperature materials to overcome the problem are presented and discussed.

Chapter 5 Development and Optimisation of a Smaller Machine Running at Higher Temperature

The main objective of this study is to develop a smaller machine that can run at a higher temperature. Therefore, this chapter explains the development and optimisation of a smaller IPM motor, which can run at a higher temperature. Simulations have been conducted to come up with a smaller machine that can run safely with the desired output. Chapter 4 has already presented the simulation results for the smaller IPM motor. However, smaller motors will produce higher losses, and higher internal temperatures may occur, which can damage the motor and demagnetise the permanent magnets. Therefore, in this chapter, simulations are conducted with the alternative of higher temperature materials for the laminations, permanent magnets, and coil insulation to protect the motor and to make sure that it can run safely.

5.1 Introduction

Nissan LEAF's motor has been selected as a benchmark motor. However, to achieve the main objectives and come out with a smaller motor, some materials of the benchmark motor need to be replaced with higher temperature materials. Table 5.1 lists the materials used for Nissan LEAF.

Table 5. 1 Material used for Nissan LEAF

Parts	Materials
Rotor lamination	Standard 0.35mm M270-35A
Stator lamination	Standard 0.35mm M270-35A
Permanent Magnet	NdFeB
Wire	Enamelled wire coated with polyamide-imide (AIW)
Shaft, end cap, water jacket	Cast aluminium

5.2 Alternative higher temperature materials

There are few alternative higher temperature materials been suggested to make sure that the smaller motor can run at a higher temperature. A lot of things need to be considered, such as the price and suitability of the materials. Also, it depends on the availability of the materials. Few parts of the motor need higher temperature materials, such as rotor and stator laminations, permanent magnet, and wire. But other parts still used the same materials as used in building Nissan LEAF machines such as shaft, end cap, and water jacket.

5.2.1 Rotor and stator lamination

It is crucial to find suitable materials used in building the motor, especially for the rotor and stator laminations. Four categories of materials may be good selections for motor lamination:

- Laminated silicon steel
- High saturation ferromagnetic alloys
- Amorphous ferromagnetic materials
- Soft magnetic powder composites

M270-35A lamination steel is in the first category of laminated silicon steel. The addition of 0.5% to 3.25% of silicon (Si) increases resistivity, which can reduce eddy current losses. As a result, this will improve the magnetization curves B-H of low carbon steels. However, increasing the silicon content will increase the hardness of the lamination and, as a consequence, shortens the life of the stamping tooling.

Silicon steels are generally specified and selected based on allowable specific core losses. The M number indicates maximum specific core losses. The electrical steel M270-35A offers nearly the lowest core loss in this class of material. It is probably the most commonly used in the manufacture of rotor and stator lamination in motors and generators.

As an alternative, there are other laminations, which can be used at a higher temperature such as Rotelloy, thin nickel-iron (NiFe), and Hiperco50. However, the price is quite high compared to the laminated silicon steel. Hiperco50 alloy is an iron-cobalt-vanadium (49% Co-2% V-Fe) soft magnetic alloy, which exhibits high magnetic saturation, maximum permeability, and low AC core loss. Vacoflux50 (50% Co) cobalt-iron alloy is similar and is typically used for manufacturing magnetic lenses, relays, motors, and actuators with high torque and force. The

magnetic properties of Hiperco50 alloy have been measured up to temperatures of 800°C. It has been determined that the upper-temperature limit for the reliable operation of this material is 580°C [82]. Table 5.2 presents the material properties of Hiperco50.

Table 5. 2 Material Properties of Hiperco50

Mass density	8120 kg/m ³
Modulus of elasticity	207 Gpa
Electric conductivity	2.5 x 10 ⁶ S/m
Thermal conductivity	29.8 W/(mK)
Curie temperature	940 °C
Specific core loss at 2T	76 W/kg
Saturation flux density	2.38 T
Yield strength	430 Mpa
Core losses at 400 Hz and 1.5 T	44 W/kg
Core losses at 400 Hz and 2.0 T	76 W/kg

Due to the availability and suitability, Hiperco50 has been chosen as rotor and stator laminations to build a higher temperature motor.

5.2.2 Permanent Magnets

In most cases, Neodymium iron boron became the best choice to design a permanent magnet machine due to its characteristic, as mentioned in Chapter 2. However, Higher Hci materials of NdFeB can be used at the temperature as high as 200°C, and under 100°C for low Hci materials.

PMs are also known as hard magnetic materials. There are three classes of PMs commonly used for electric motors [19]:

- 1) Alnicos (Al, Ni, Co, Fe).
- 2) Ceramics (ferrites), for example, barium ferrite BaOx6Fez03, and strontium.
- 3) Rare-earth materials such as samarium-cobalt (SmCo) or Neodymium-iron-boron (NdFeB).

Generally, samarium-cobalt can be used at a higher temperature up to 350°C compared to neodymium-iron-boron, which needs to be used at lower temperature applications to avoid demagnetization. Table 5.3 shows the characteristics of the permanent magnets. Even the remanent flux density of samarium-cobalt, $\text{Sm}_2\text{Co}_{17}$, seems to be smaller than N42UH, but the permanent magnet can stand up to 350°C before it is starting to demagnetise. In this case, for a higher temperature machine, $\text{Sm}_2\text{Co}_{17}$ will be used as the permanent magnet.

Table 5. 3 Material properties of permanent magnet

Permanent magnet	Remanence flux density, B_r
N42UH	1.2T at 150°C
$\text{Sm}_2\text{Co}_{17}$	1.16T at 350°C

Electrical machines require high electric loading, and therefore the demagnetisation of permanent magnet material is a significant consideration in the selection of materials. Neodymium-iron-boron is the most advanced type of magnet material used in PM motors for electric vehicle applications. Besides considering the use of NdFeB as a magnet material for the motors, this research also conducts an electromagnetic and thermal analysis of the same topologies of IPM motor when Samarium Cobalt (SmCo) is used as the magnet material. In terms of both cost and flux density, a PM with NdFeB will perform better than one with SmCo. However, when it comes to temperature distribution, especially for smaller motors, as proposed in this study, NdFeB has limitations. Therefore, to avoid the demagnetisation of the magnets in an IPM motor, SmCo has more advantages. Generally, SmCo can be used at higher temperatures up to 350°C compared to NdFeB, which needs to be used in lower temperature applications only up to 140°C.

A comparison of the flux density of two similar IPM motor configurations using different types of rare-earth magnets at no load is shown in Figure 5.1. Both motors used the same value of MMF. The motor that uses SmCo as the rare-earth magnet shows lower flux density in the stator yoke and rotor laminations than the machine with NdFeB, as shown in Figures 5.2 and 5.3. The highest value of coil flux linkage for the motor with NdFeB is 0.1643 Wb. Meanwhile, for the motor with SmCo, the highest coil flux linkage value is 0.1574Wb. Consequently, the IPM motor with SmCo will produce lower values of back-EMF and core loss and will need a higher current to provide the required output torque in the constant torque region.

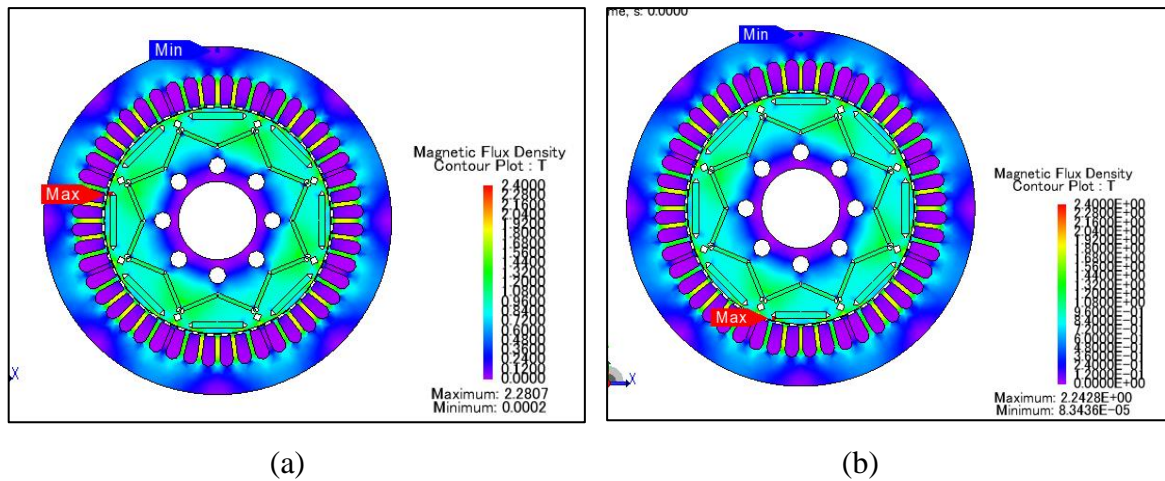


Figure 5. 1 Flux density: (a) Motor A + NdFeB, (b) Motor A + SmCo

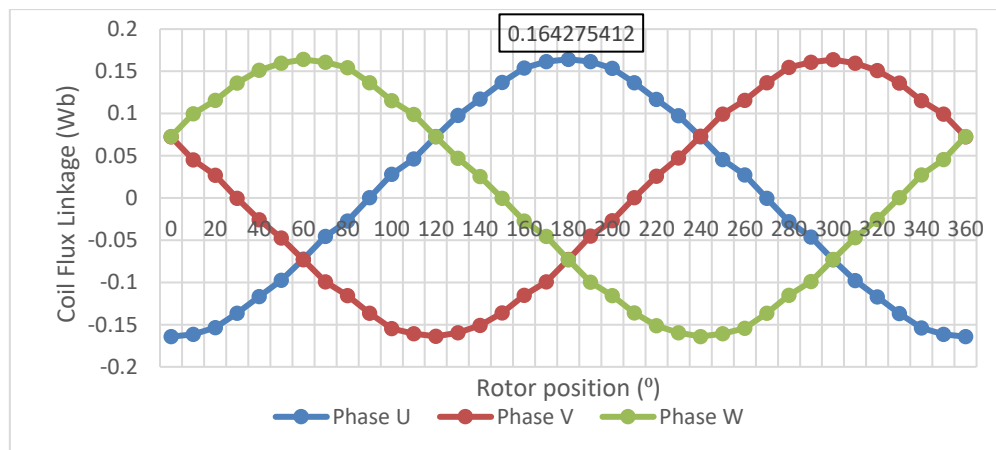


Figure 5. 2 Coil flux linkage for the motor with NdFeB

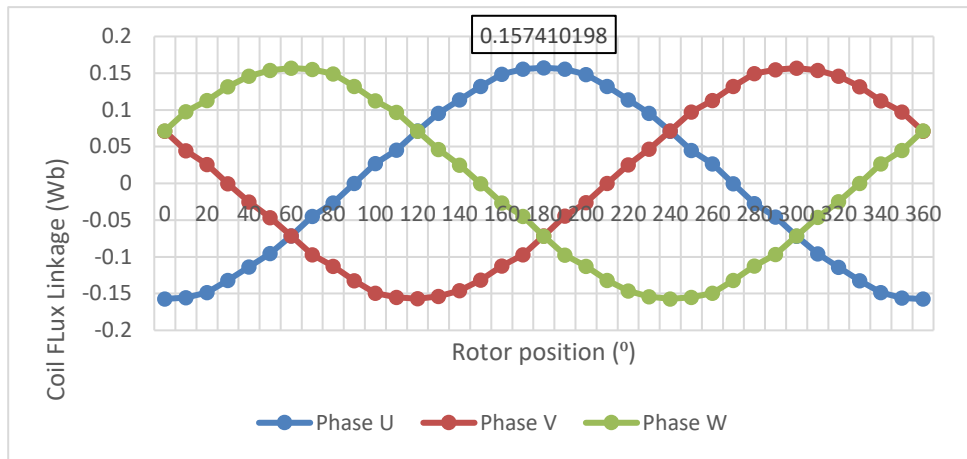


Figure 5. 3 Coil flux linkage for IPM motor with SmCo

Figure 5.4 shows the electromagnetic torque for both IPM motors, which have similar size and rotor topologies but use different types of rare-earth magnet. Both motors have the same value of J_A applied. As a result, with the various amount of J_A , the IPM motor with SmCo generates lower torque compared to the IPM motor with NdFeB. Consequently, the IPM motor with SmCo needs higher current to maintain the output characteristics. Higher current will produce more power losses and needs more attention to be paid to the coolant system.

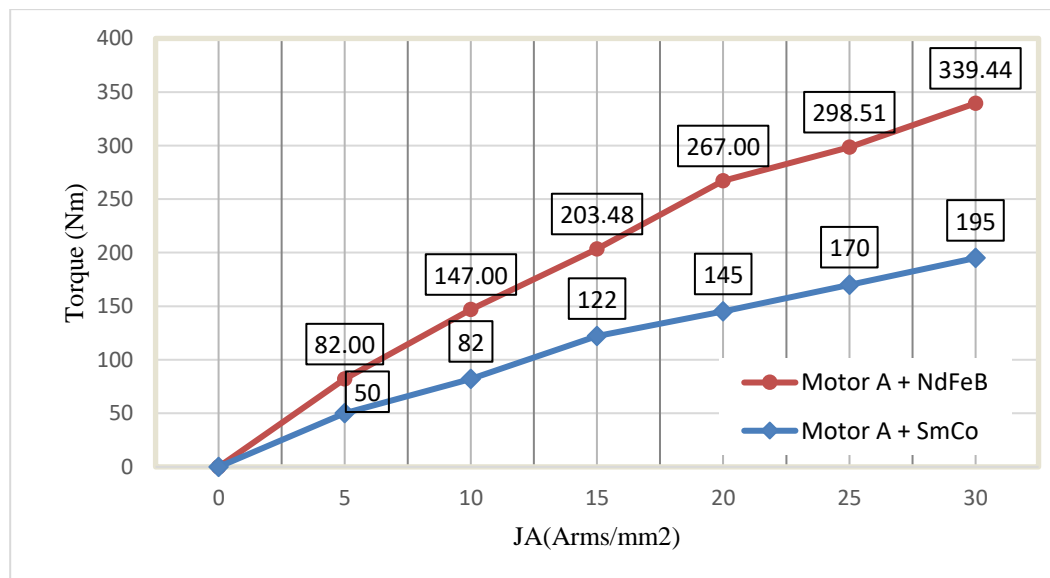


Figure 5. 4 Electromagnetic torque comparison with the various value of J_A

In terms of demagnetisation, SmCo has a massive advantage since this rare earth magnet material is very corrosion-resistant, and it can withstand high temperatures compared to NdFeB. Therefore, in this study, Recoma33E has been chosen, and Figure 5.5 below shows the demagnetisation characteristics of the magnets. It is noted that only after 350°C are the magnets predicted to start to demagnetise. Thus, the lower limit of its permanent magnet flux density is 0.2T at 350°C.

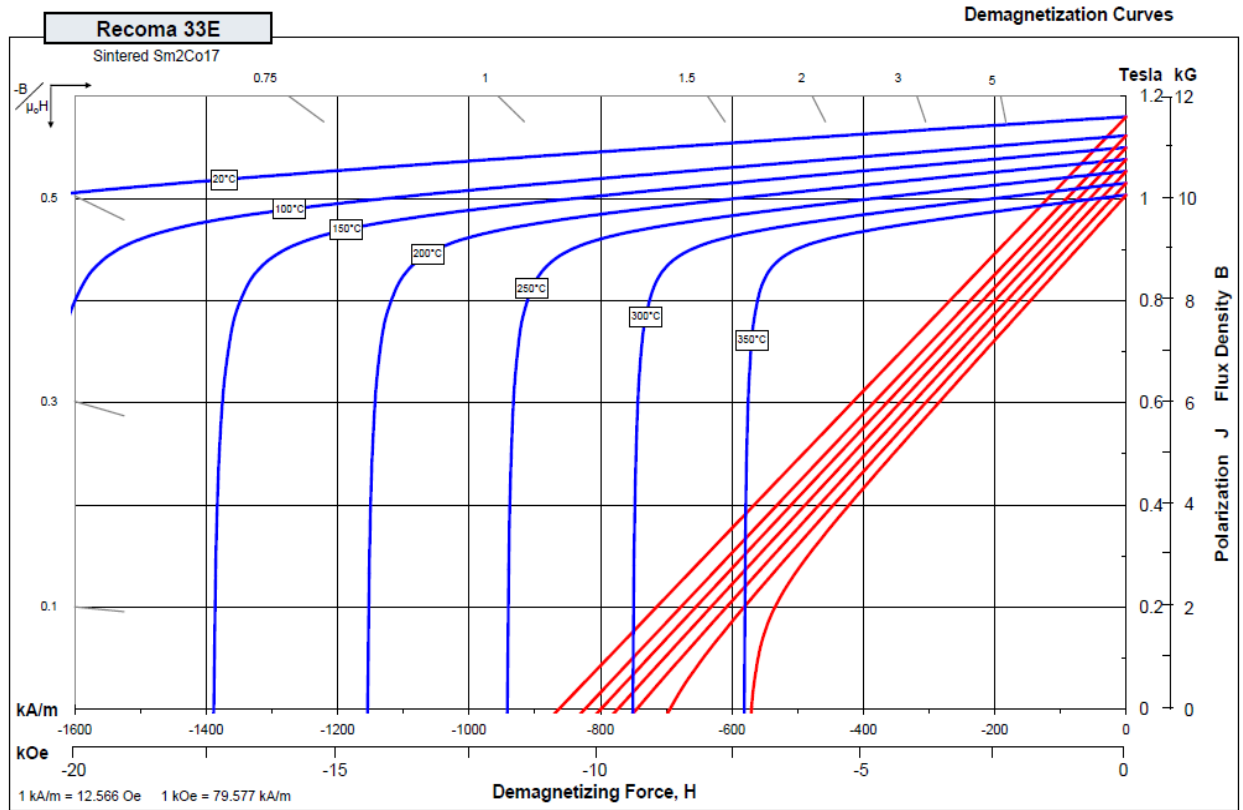


Figure 5. 5 Magnet characterisation B-H curve for SmCo[48]

5.2.3 Coils insulation

Table 5.4 shows the maximum allowable temperature rise for the armature windings of electric motors, according to the International Electrotechnical Commission (IEC) standard. Therefore, it is crucial to find a suitable insulation class for the prototype motor's winding. For a high-temperature motor, insulation class H would be the right choice. The maximum temperature rise is achieved based on an ambient temperature of 20°C, and it is determined by the temperature limit of the insulating materials. The temperature of the cooling medium is assumed to be $\vartheta_c \leq 20^\circ\text{C}$. However, for the Nissan LEAF, the coolant temperature is 65°C.

Thus, with $\Delta\vartheta$ being the maximum allowable temperature rise according to Table 5.4, the actual maximum temperature of the winding is:

$$\vartheta_{max} = \vartheta_c + \Delta\vartheta \quad (5.1)$$

Table 5. 4 Maximum Temperature Rise, $\Delta\vartheta$, for different winding classes [83]

Machine rated power	Insulation class				
	A (°C)	E (°C)	B (°C)	F (°C)	H (°C)
< 5000 kVA	60	75	80	100	125
\geq 5000 kVA	60	70	80	100	125

Even for H insulation, there are few available types of copper wire, which could be chosen. Table 5.5 presents a list of possible wires that can be used for the stator winding with the appropriate temperature ranges.

Due to practical limitations and the resources available, some changes had to be made when the prototype was being built. At first, Kulgrid HT Magnet Wire was chosen as a suitable wire for the high-temperature machine. However, it was too difficult to wind the stator since this magnet wire kink easily and cannot be straightened up as with standard enamel wire. Consequently, Magnetemp Y-240 has been chosen for the higher temperature machine as this was the most top temperature wire available at the time of this research.

Table 5. 5 List of wires with ranges of temperature

Types	Description	Temperature index
Kulgrid HT Magnet Wire [84]	High-temperature magnet wire insulated with a fully cured vitreous enamel film that is firmly bonded to the wire conductor	-450°F to +1000°F @ -267°C to +537°C
Polyester 200 Dual Coat Enamel Round Wire[85]	High performance modified multi-coat polyester-based enamel with a polyamide-imide topcoat	212 °C
Magnetemp C-180	A polyestermide enamelled copper wire	192°C
Magnetemp CA200	A polyestermide enamelled copper wire, overcoated with polyamide-imide.	210°C
Magnetemp Y-240 [86]	A polyamide enamelled copper wire	240°C
Ultrashield Plus[87]	Magnet wire on the copper conductor is UL listed at Class 200 and recommended for NEMA MW 35-C and MW 73-C wire applications with higher burner burnout requirements.	Thermal aging 215°C Thermoplastic flow 390°C

Figure 5.6 presents the coil temperatures for motor A, B, and C. The thermal analysis shows that, when the size of the machine is reduced, the temperature distribution in the motor will increase gradually. Either failure of the stator winding insulation or demagnetisation of the magnets can be caused damage to an automobile. The figure reveals that the temperature slowly reaches an equilibrium state. End-winding is the hottest area in the motor. Therefore, the temperature for the coils is measured at the end-winding. As expected, the temperature at the coils for motor C is the highest at above 200°C. Meanwhile, the temperature at the coils for motor A and B remains under 150°C. There are considerable differences in temperature between motor B and C due to the higher MMF applied to motor C to gain the same output performance as for motor A and B.

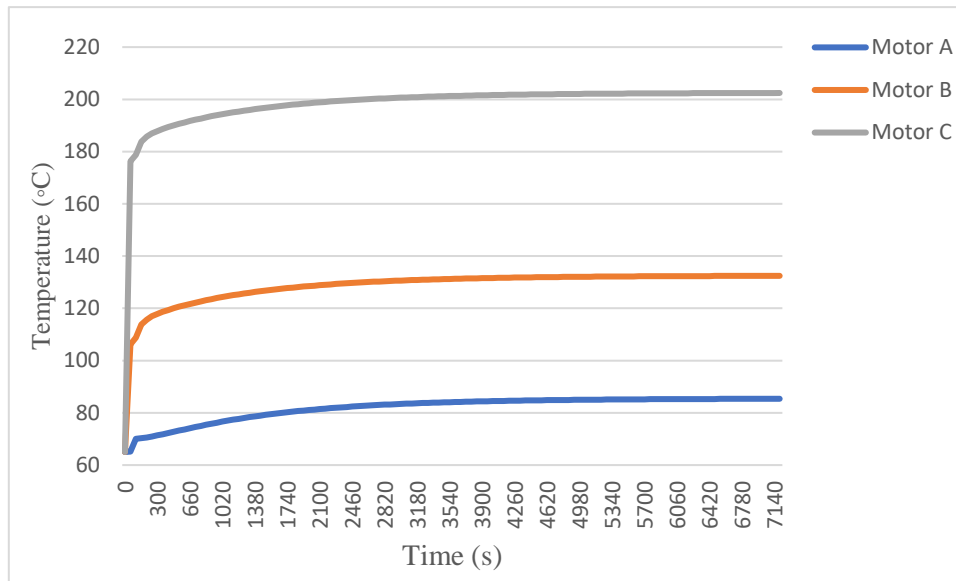


Figure 5. 6 End-winding temperatures for Motor A, B, and C

5.3 Comparative study of the IPM motors

5.3.1 *Samarium Cobalt as permanent magnets*

As mentioned, the size of permanent magnets is different for each other. However, magnet 1 and magnet 2 have the same size and weight. Meanwhile, magnet 3 has a different weight and size. The location of the permanent magnets is, as shown in Figure 5.7. Also, Figure 5.8 presents the weight of the SmCo and NdFeB in IPM motors. The weight of SmCo in motors A, B, and C is slightly higher compared to the NdFeB. The amount of magnet density is 8300 kg/m^3 and 7550 kg/m^3 for SmCo and NdFeB, respectively. Thus, the weight of permanent magnets for motor C is reduced by approximately 20% from that of the original motor.

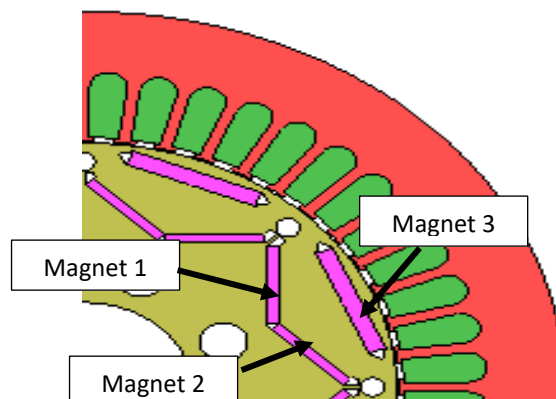


Figure 5. 7 Permanent magnets in IPM motor

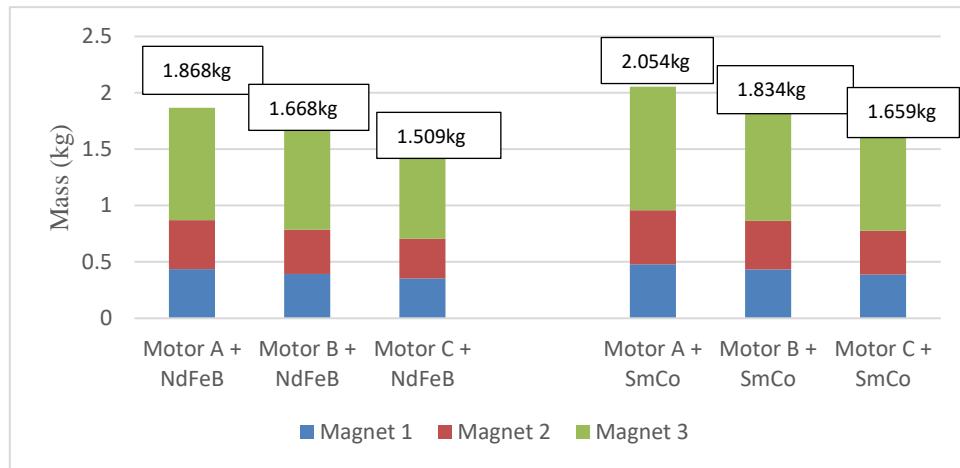
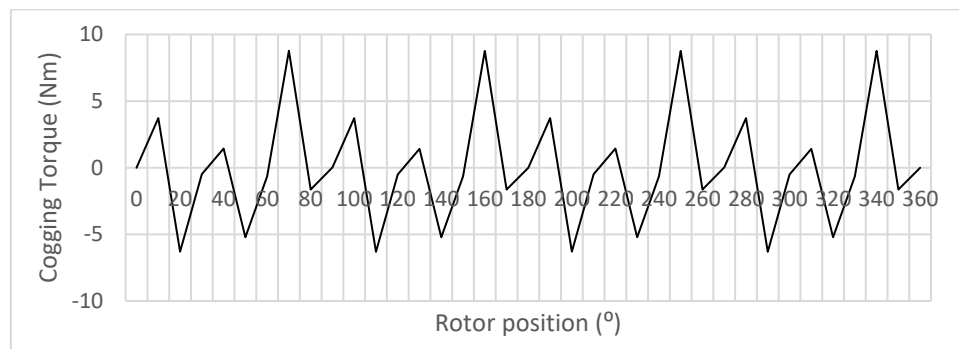
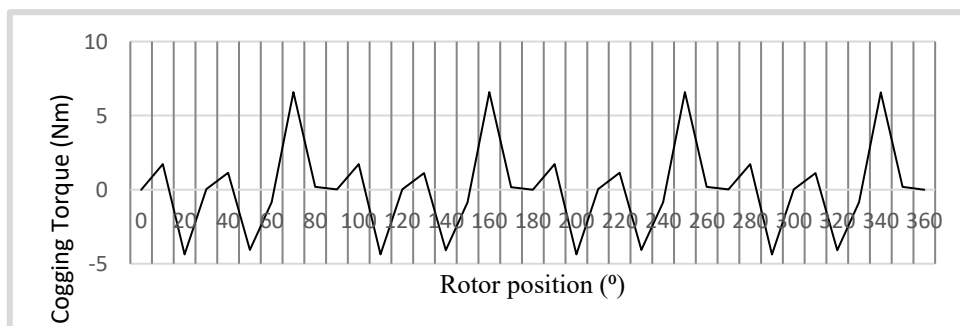


Figure 5. 8 Magnet mass of permanent magnets

With lower flux linkage and back-EMF, IPM motor with SmCo as the permanent magnet material needs higher MMF to achieve the required output performance for electric vehicle applications. Therefore, by increasing the number of turns in the winding slot from 6 to 10 turns, the motor will produce more than 280 Nm rated torque at 25 J_A. However, the value of cogging torque for the motor with SmCo is less 25% than the motor with NdFeB, as shown in Figure 5.9.



(a)



(b)

Figure 5. 9 Cogging torque: (a) Motor A with NdFeB, (b) Motor A with SmCo

5.3.2 Effect of using different rotor and stator laminations

The stator and rotor are built up from stacks of magnetic-alloy lamination. The materials used to build the machine should be able to survive in high temperatures to make sure that the IPM motor can run at high temperature. Hiperco50 has been chosen as lamination material for the stator and rotor because it can withstand high temperatures up to 937 °C. The same IPM motor topologies and parameters as before have been used with SmCo as magnet material and Hiperco50 for the rotor and stator lamination. As seen below, to achieve the 280 Nm rated torque, the MMF needed is less than that for the motor with M270-25A lamination. Figure 5.10 shows the torque value for various J_A . The blue line is the torque value for the motor using M270-35A as the rotor and stator lamination.

On the other hand, the red line is the torque value for the motor with Hiperco50 as rotor and stator lamination. It is showing that by using Hiperco50 as rotor lamination, the motor will give higher torque value at the same J_A . Motor C with Hiperco50 will need approximately 30 J_A to achieve the desired output torque. Indirectly, the choice of Hiperco50 as rotor and stator lamination means an increase in the flux density of the machine.

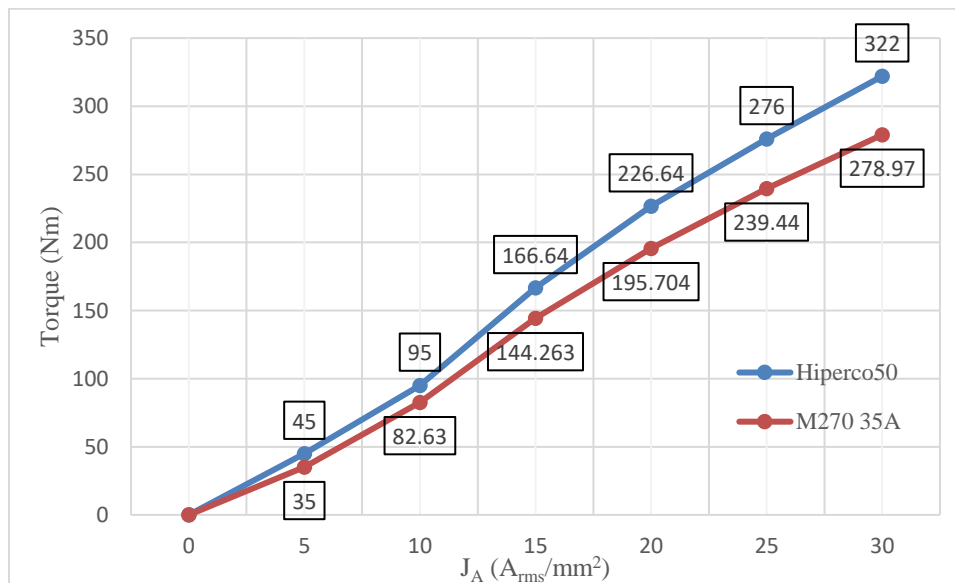


Figure 5.10 Torque for various J_A

Flux line figures can be used as an indicator of whether the flux created by the permanent magnet and armature coil stray from its magnetisation pattern. Strayed flux will result in higher back EMF and will damage the design of the motor. Figure 5.11 shows the flux line for the IPM motors. Meanwhile, Figure 5.12 shows the magnetic flux density for both motors. The motor

with Hiperco50 as rotor and stator lamination produces a higher value of magnetic flux than the motor with M270-35A rotor and stator lamination.

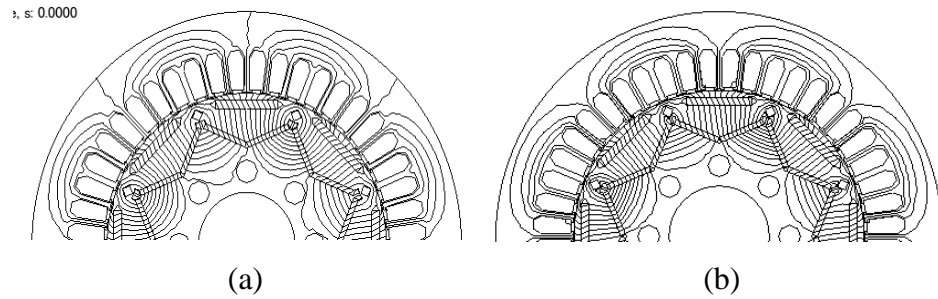


Figure 5. 11 Flux line : (a) Motor C with M270-35A, (b) Motor C with Hiperco50

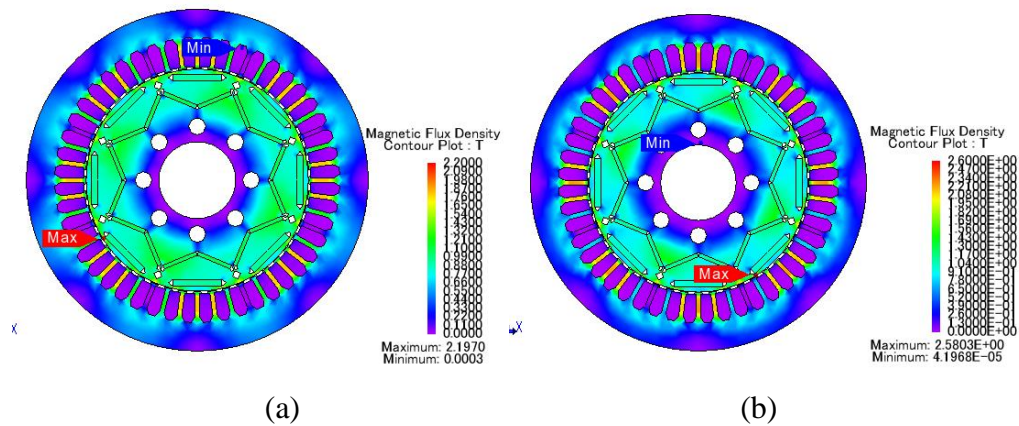
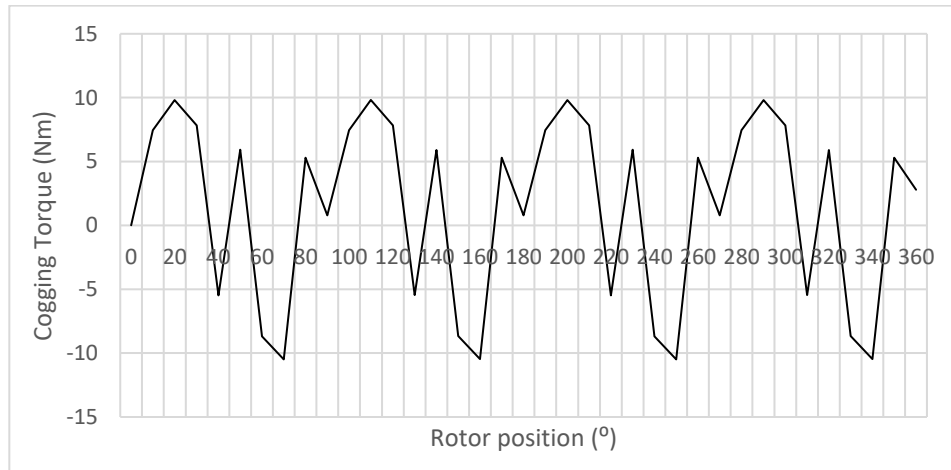
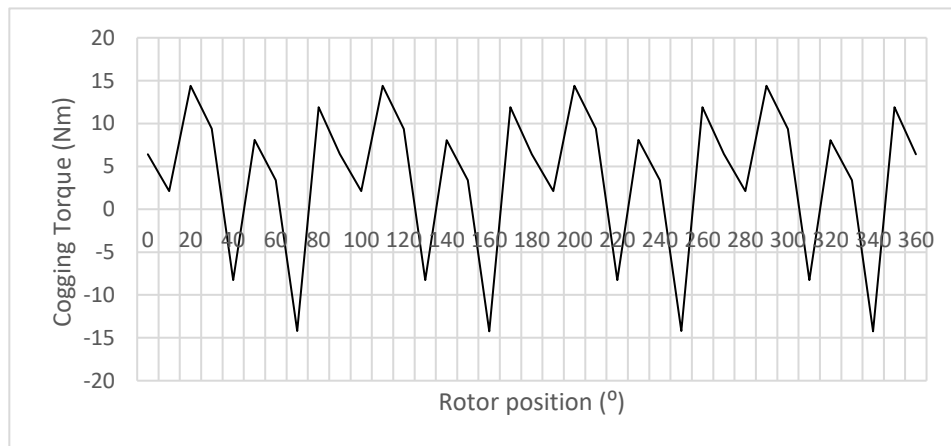


Figure 5. 12 Magnetic flux density: (a) Motor C with M270-35A, (b) Motor C with Hiperco50

The cogging torque graph is plotted during no current is injected into the armature coils. Figure 5.13 presents the cogging torque for both motor C. The graphs show that the value of cogging torque for the motor with Hiperco50 as rotor and stator lamination is higher than the motor use M270-35A as rotor and stator lamination. Higher cogging torque will cause noise and motor vibration. As a drawback, optimisation has been done in the next section to reduce the value of the cogging torque.



(a)



(b)

Figure 5. 13 Cogging torque: (a) Motor C with M270-35A, (b) Motor C with Hiperco50

5.3.5 Thermal analysis on motor C with Hiperco50

Two probes have been located at the end-winding as point 1 and inside the slot as point 2, as shown in Figure 5.14. The purpose is to differentiate the temperature value. Figure 5.15 presents the thermal analysis in 7200s interval time for motor C with Hiperco50 for the rotor and stator lamination. It is clearly showing that the end-winding produces the highest temperature in the motor. It can be concluded that the motor C is safe to be designed and run for vehicle applications. The temperature for the permanent magnet is still under the demagnetisation limitation. Also, the temperature at the coils did not exceed 230°C.

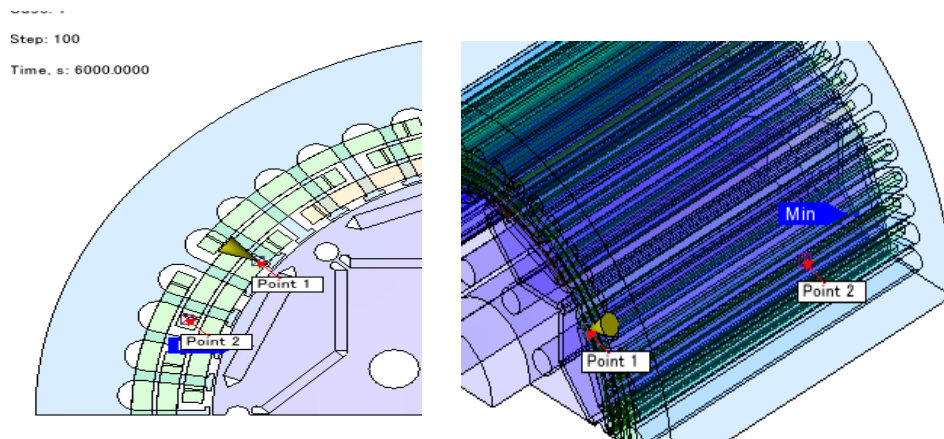


Figure 5. 14 Location of the probes

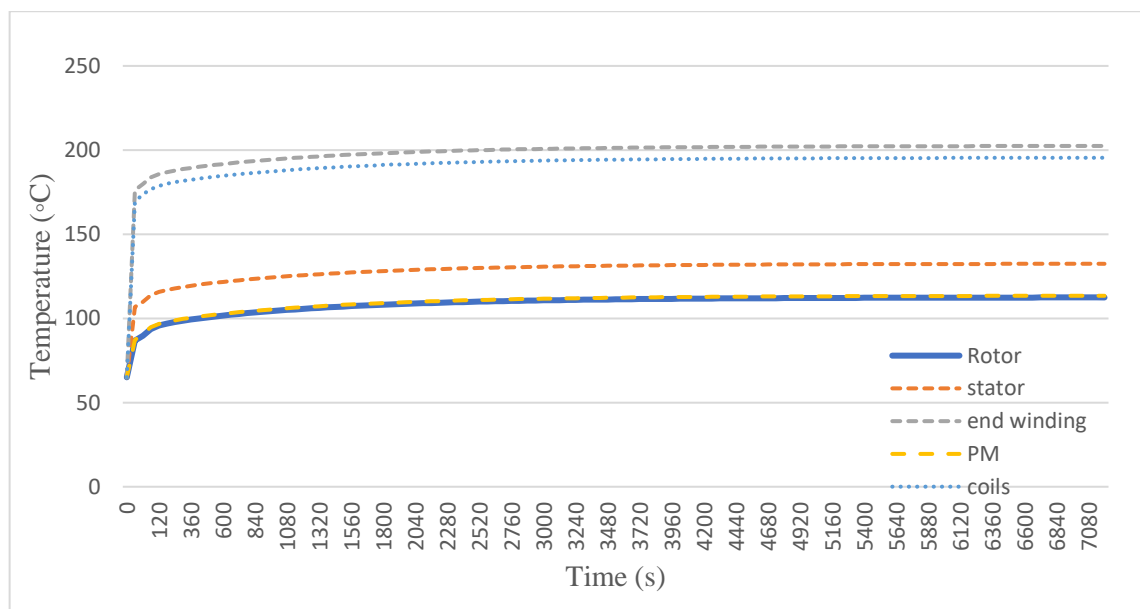


Figure 5. 15 Temperature variations in motor C with Hiperco50

The hottest area in the motor is at the end-winding. Meanwhile, the shaft has a minimum temperature rise, as shown in figure 5.16.

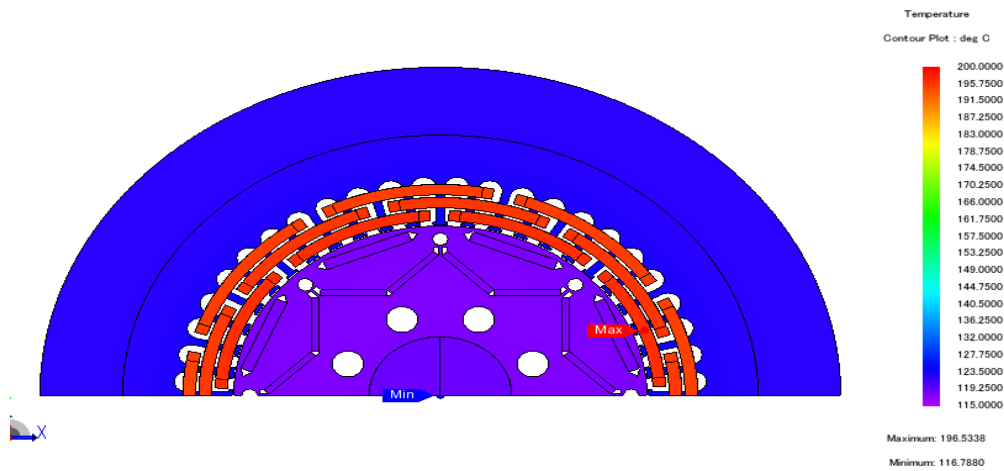


Figure 5. 16 Temperature variations in motor C.

Figure 5.17 shows the magnetic flux density in the motor C during full load analysis. The maximum flux density was 2.4T and located at the end-winding.

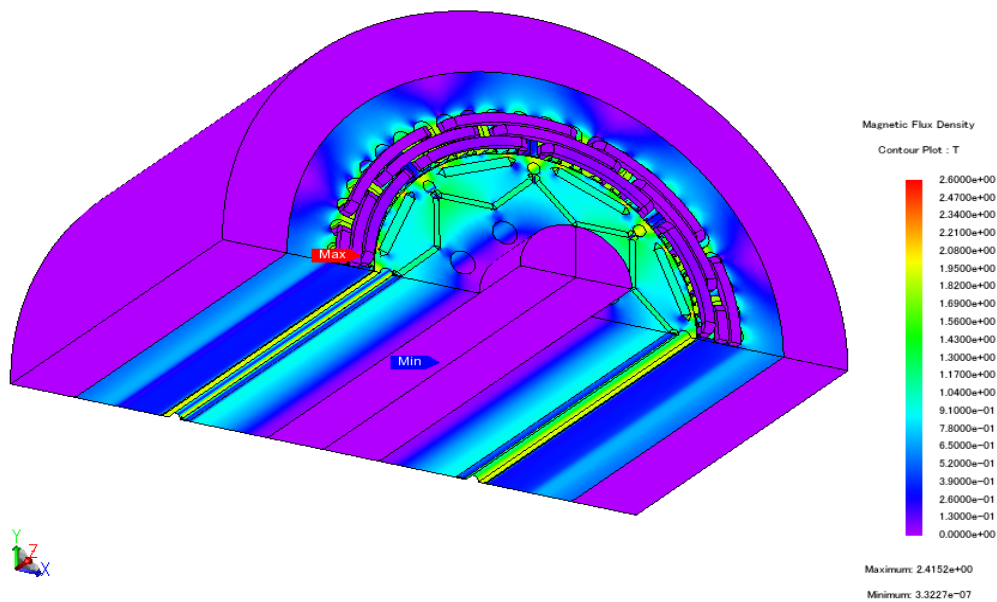


Figure 5. 17 Magnetic flux density in motor C with Hiperco50

5.4 Cogging torque reduction

It can be concluded that motor C with Hiperco50 as rotor and stator lamination gave the better output performance compared to the motor C with M270-35A. However, the value of the cogging torque is approximately 50% higher than the motor C with the original rotor and stator lamination. The cogging torque is one of the significant concerns in IPM motor design. Cogging torque is an unwanted characteristic of some permanent magnet motor design. The interaction between the permanent magnet rotor and stator slots of the machine will produce cogging torque. The shape of the rotor and stator involves the feature of high cogging torque. Besides, the motor with high cogging torque will cause noise and vibration. Modification needs to be done either on the rotor or the stator to minimise the cogging torque. Figure 5.18 shows the original features of the stator tooth for motor C.

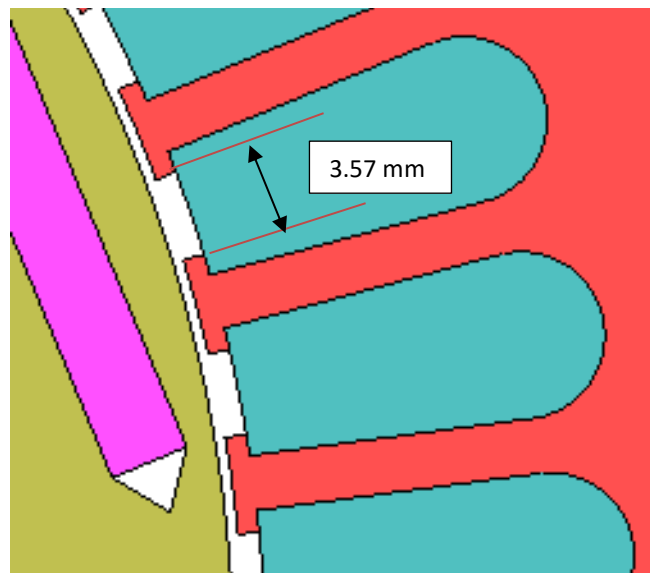


Figure 5. 18 Slot opening width for motor C

The effect of slot opening width on cogging torque is analysed using finite element analysis. In this study, the tooth gap width is reduced. The new slot opening width is, as shown in Figure 5.19. Both sides of the tooth are added with 0.5mm length. Therefore, the new slot opening width is 2.57mm.

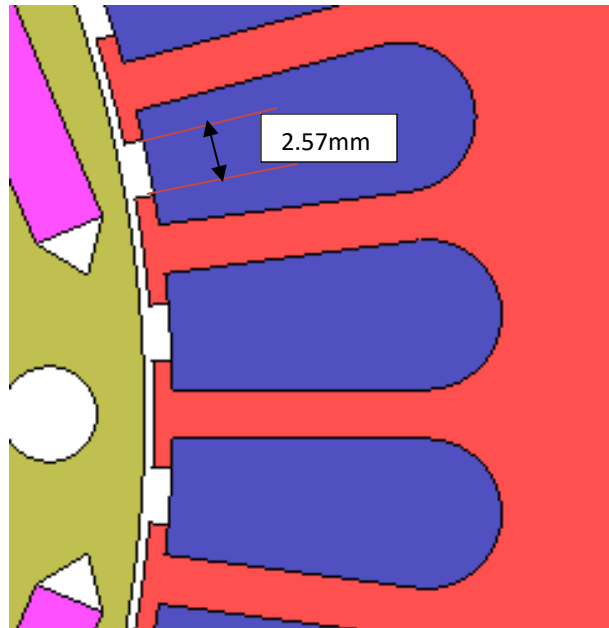


Figure 5. 19 New slot opening width

By reducing the slot opening width also has improved the back-emf waveform. The comparison has been made between before and after the stator modification. Figure 5.20 presents the back emf waveform before and after slot opening width modification.

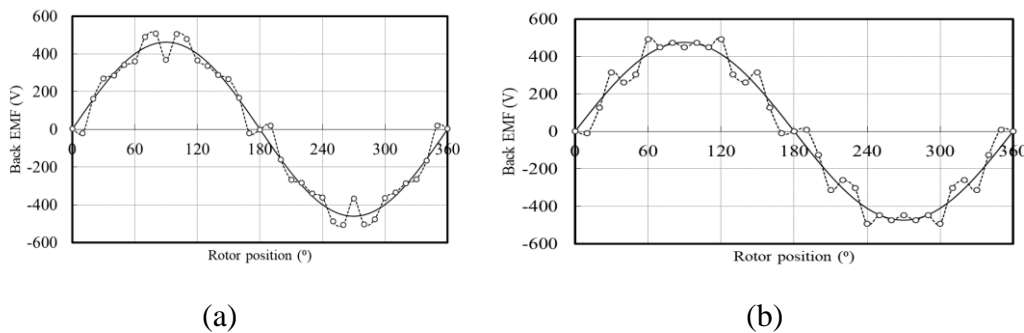


Figure 5. 20 Back EMF waveform: (a) before the slot opening width modification, (b) after the slot opening width modification

The cogging torque for the new slot opening width motor is, as shown in Figure 5.21. Before the modification, the cogging torque is 15Nm. However, with the reduction in slot opening width, the cogging torque decreases approximately 30% from the previous motor.

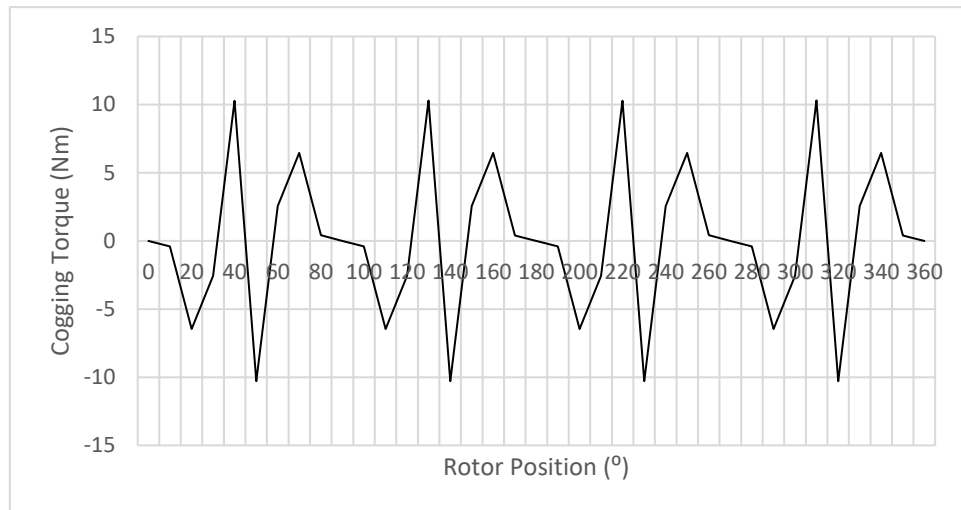


Figure 5. 21 The cogging torque after the slot opening width modification

Figure 5.22 presents the torque value for various J_A before and after the modification of the motor. After the adjustment of the slot opening width, the torque value is decreased by approximately 9% from the previous motor. Though the torque value is lower than the previous motor, the value is still in the range of IPM motor's desired torque.

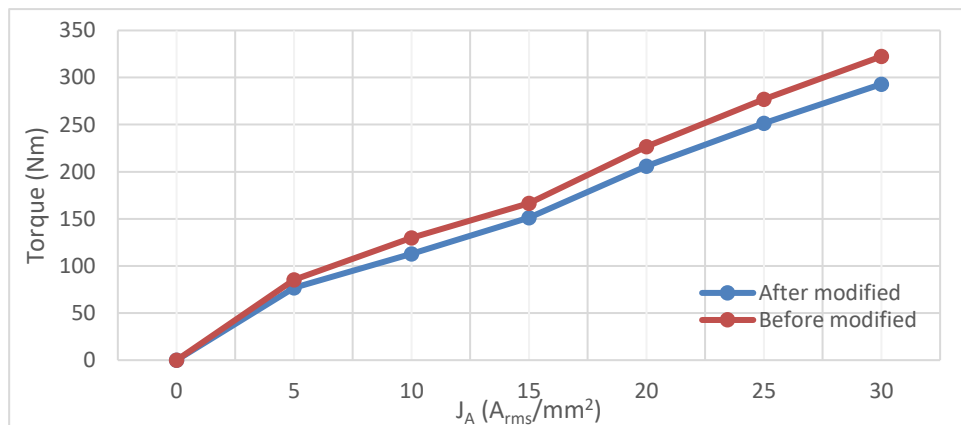


Figure 5. 22 Torque value with various J_A

Analysis of torque versus speed and power versus speed is conducted to observe the maximum torque and speed of the motor. Figure 5.23 represents the torque and power versus speed characteristics for modified motor C with Hiperco50 as stator and rotor lamination. The maximum torque and power for the motor are 293Nm and 71,628W, respectively. However, after 6000 rpm, the torque value started to be decreased slightly.

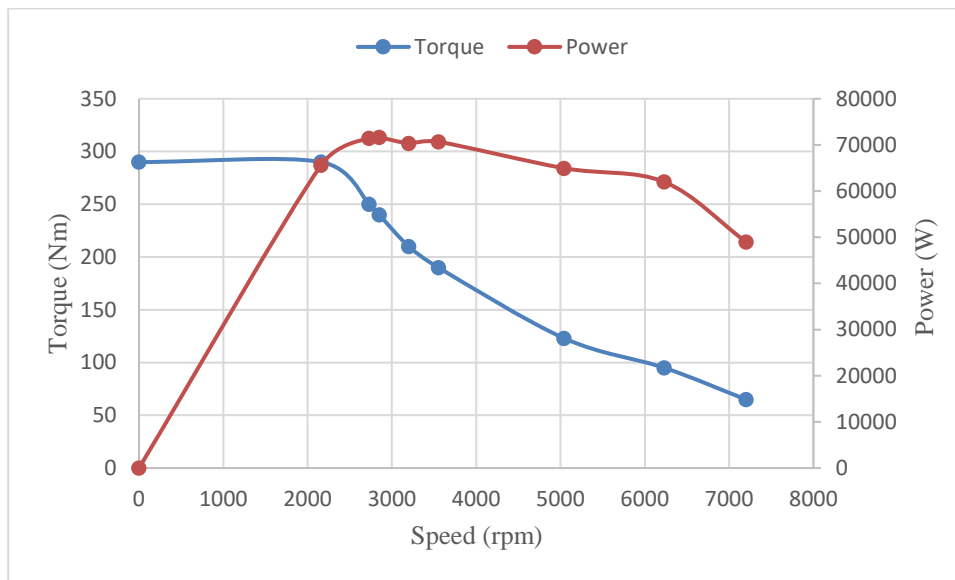


Figure 5. 23 Torque and power versus speed

5.5 Material cost

Reducing the size and weight of a motor means the material cost will decrease too. Table 5.6 present the price of a permanent magnet for IPM motors by referring to the current value of permanent magnet, 70USD per kg [45]. Consequently, the cost of other parts in the motor, such as rotor and stator laminations, will be reduced too.

Table 5. 6 Cost of permanent magnet

	Magnet Mass (kg)	Magnet price (USD)
Motor A	1.86	130.2
Motor B	1.68	117.6
Motor C	1.509	105.63

5.6 Summary

Based on the simulation results that have been conducted, few conclusions can be made to choose a better machine to be build and the challenges that have to be faced. To produce a smaller higher temperature motor with the desired output required as Nissan LEAF as the benchmark machine, motor C with high-temperature materials such as SmCo as the permanent magnets and Hiperco50 as the rotor and stator laminations is the best choice. Instead, the motor can run safely at a higher temperature, and also reduces the usage of the permanent magnet. However, the cogging torque is higher. Therefore, design modification has been done on the slot opening width to improve the cogging torque. The next chapter will discuss the conclusions that will be taken into account to build a smaller motor with better electromagnetic performance. However, only the smaller size of the prototype motor will be built and tested due to the cost and material availability.

Chapter 6 Machine Construction and Test Rig Description

To validate the FEA results for the model of the IPM motors that have been designed, two prototype machines have been developed. One of these prototype IPM machines is developed using the same materials as in the existing IPM machine, while the other one uses different materials. However, the size and power output have to be reduced. It is due to the high cost if the same size and power output of the machine were to be used. The first step of building the prototype machine is started by transferring the machine design parameters from Infolytica Magnet software into a technical drawing using AutoCAD software. Then, the most crucial part of the process is finding suitable materials and suppliers. Sometimes, the materials needed are not available, and therefore it is possible to conduct a redesign and reanalysis to find appropriate materials for the prototype machines. Therefore, a lot of work needs to be done to find an alternative.

6.1 Introduction

Both prototype machines have the same stator and rotor configurations. Each machine has eight poles with 48 slots, and the rotor and stator lamination was laser cut. Table 6.1 shows the main parameter of the machines. Machine II is smaller than machine I. The reason for this is that, from the simulation results, machine II can achieve the same performance as a machine I even though it is smaller. Machine II is designed to run at high temperatures, and thus some of the materials used are different from those in machine I.

Table 6. 1 Main Parameter of Prototype Machines

	Unit	Machine I	Machine II
Stator Outer Diameter	mm	147.8	129.1
Rotor Outer Diameter	mm	95.98	83.76
Stator Inner Diameter	mm	96.9	84.62
Rotor Inner Diameter	mm	32.6	28.64
Air gap	mm	0.5	0.432
Rotor Radius	mm	48	41.9
Machine Length	mm	45.92	10.08

Machine I was constructed with precisely the same materials used to build the existing Nissan LEAF motor. Meanwhile, Machine II was constructed using high-temperature materials. The purpose of building two different machines is to compare both machines and to make sure that one of the machines can run at higher temperatures. The materials used in constructing both machines are as stated in Table 6.2. Other parts, such as the shaft, end cap, and water jacket, used the same materials in both machines. Meanwhile, table 6.3 presents the electrical and magnetic properties of the materials employed.

Table 6. 2 Materials Used for Prototype Machines

	Machine I	Machine II
Rotor Lamination	M270-35A	Hiperco50 Alloy
Stator Lamination	M270-35A	Hiperco50 Alloy
Permanent Magnet	NdFeB N42UH	Recoma Sm ₂ Co ₁₇
Wire	0.9mm Magnetemp CA200 Grade 2	0.725mm Magnetemp Y240 Grade 2
Shaft, end cap, water jacket	Aluminum alloy	

Table 6. 3 Material Properties

Electricity conductivity Aluminum (cage)	3e+7 S/m
Residual flux density, B _r , of NdFeB	1.2T
Residual flux density, B _r , of Recoma 33E	1.16T
Coercive force, H _c , of NdFeB	915 kA/m
Coercive force, H _c , of Recoma 33E	865 kA/m
Stator core, rotor core, and tube	Non-oriented steel

6.2 Stator construction

Standard 0.35mm lamination steel M270-35A was used for the stator construction in the existing Nissan LEAF motor. Therefore, the same material is used for the stator lamination for machine I. A stator tooth of length 147.8 mm requires around 422 laminations, each nominally 0.35mm thick. Hiperco50 has been chosen for machine II [83], which needs 368 laminations for a stator tooth length of 129.1 mm. The lamination packing factor is assumed to be 97% because the other 3% is accounted for glue, air, and the iron lamination coating.

The rotor and stator lamination for Machine II is built up from a stack of laminations made of a high-temperature rare-earth permanent magnetic alloy to reduce eddy current losses during operation. The magnetic properties of Hiperco50 alloy have been measured up to temperatures of 800°C. It has been determined that the upper-temperature limit for the reliable operation of this material is 580°C [82]. Figure 6.1 shows the rotor construction before winding. The housing of the stator for both machines I and II is made of aluminium alloy.

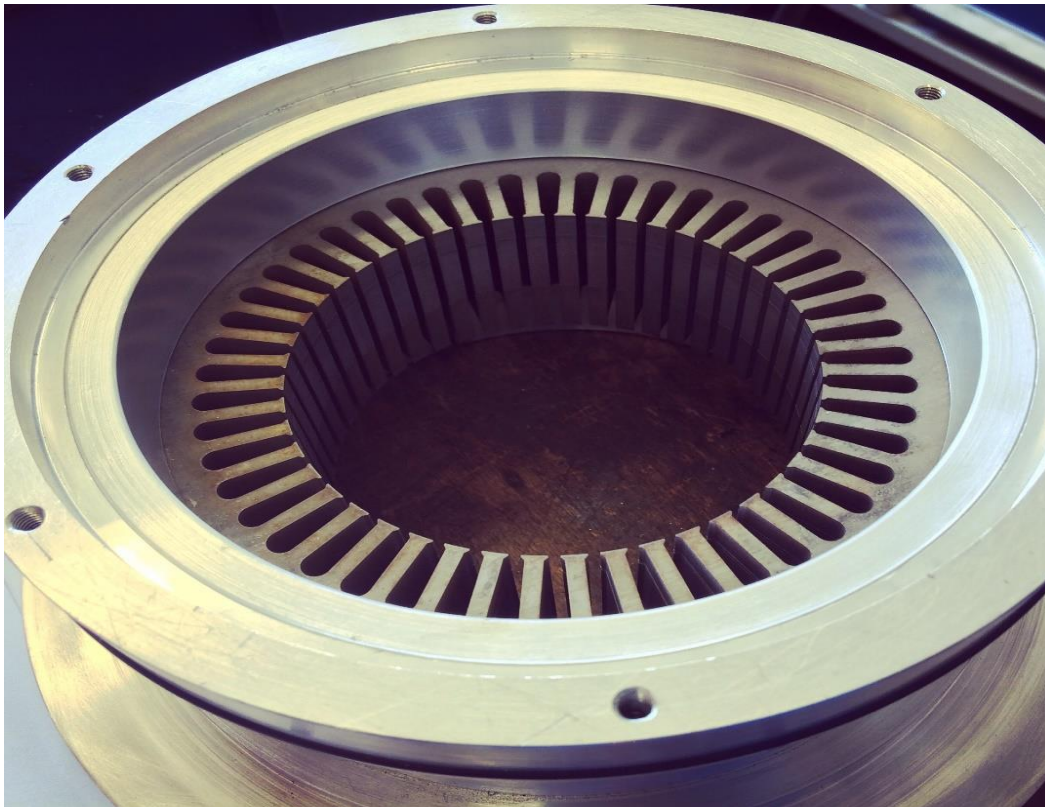


Figure 6. 1 Stator construction

6.3 Rotor Construction

The rotor construction process was carried out in the same way as for stator construction. The segment laminations were mounted on a steel shaft, which was non-magnetic to ensure that no magnetic flux path formed between the rotor segment that could adversely affect the flux linkage characteristics and hence the performance of the machine. The same material used in the stator is used to build up the rotor in both machines I and II. The two machines use different types of permanent magnets, where machine II is required to run at higher temperatures. Therefore, $\text{Sm}_2\text{Co}_{17}$ is used as the magnet material, whereas machine I use N42UH as magnet material.

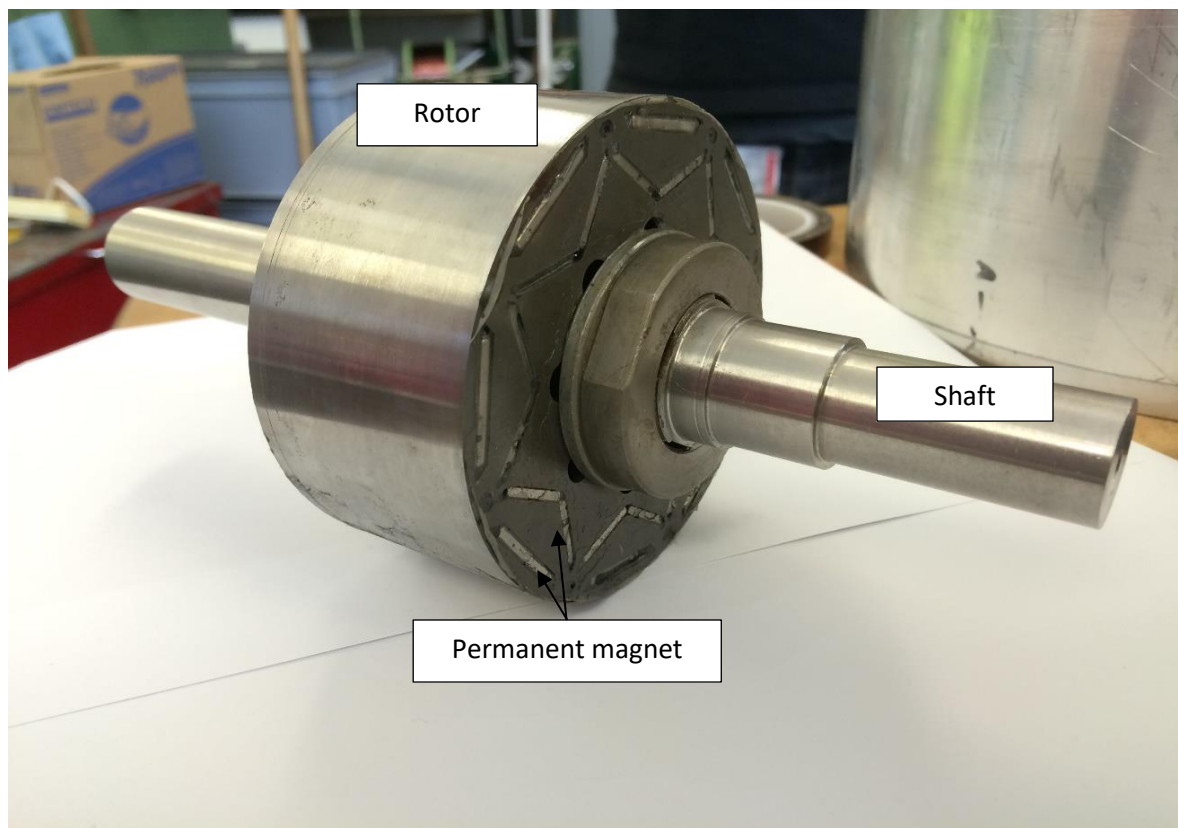


Figure 6. 2 Rotor with shaft

6.3.1 *Permanent Magnet Materials*

Even without the dissipation of electric power, a permanent magnet can still produce magnetic flux in the air gap. Compared to ferrites and Alnico, rare-earth permanent magnets enable a considerable reduction volume of excitation in the system, with higher air gap magnetic flux densities and better dynamic performance of electric motors. Neodymium-iron-boron (NdFeB) magnets have better magnetic performance than those of Samarium cobalt (SmCo). The demagnetisation curves, especially for the coercive force, are strongly temperature-dependent. Since the temperature coefficients of NdFeB are high, this material cannot be used at temperatures exceeding 150°C.

Meanwhile, SmCo, with a slightly lower B_r value, is used in harsh environments. Therefore, N42UH is used as permanent magnet material for machine I, while $\text{Sm}_2\text{Co}_{17}$ has been chosen for machine II. Arnold Magnetic Technologies produced both.

Each magnet segment is glued onto the rotor using Araldite AV138. The permanent magnet width, length, and thickness differ for the two machines and are specified in table 6.4. The remanence flux density, B_r of N42UH, is 1.2T at 150°C, and it is 1.16T for $\text{Sm}_2\text{Co}_{17}$ at 350°C. Figure 6.3 shows the permanent magnets, and their dimensions are as stated in table 6.4. The weight and size of the $\text{Sm}_2\text{Co}_{17}$ magnet are slightly smaller than the N42UH.

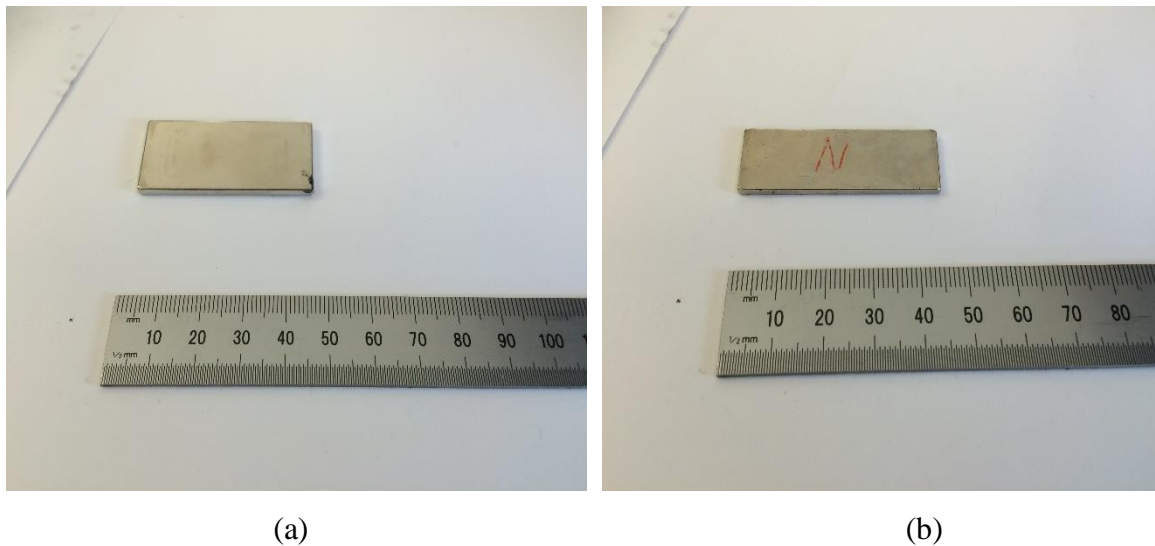


Figure 6. 3 Permanent magnets: (a) N42UH, (b) $\text{Sm}_2\text{Co}_{17}$

Table 6. 4 Dimensions of the permanent magnets

Permanent Magnet		Wide (mm)	Thickness (mm)	Length (mm)	Weight (g)
N42UH	Magnet 1 & 2	21.35	2.73	46	10.52
	Magnet 3	15.27	1.99	46	19.92
Sm ₂ Co ₁₇	Magnet 1 & 2	18.53	2.31	40.12	7.29
	Magnet 3	13.31	1.61	40.12	14.49

6.4 Windings

A 0.43 slot fill factor was chosen to calculate the initial conductor diameter. The maximum permissible current density was determined to be 25 A/mm². With a peak current of 14 amps, a wire of diameter 0.9mm was required corresponding to 25 turns per coil in a slot area of 76 mm² for machine I. Before the winding operation, the inside surfaces of each stator tooth were covered with slot liners to avoid shorting between the stator winding and stator core. Meanwhile, for machine II, the slot area is 58 mm². Thus, a 0.725mm diameter of wire has been used with 31 turns per slot. In both machines, single layer distributed winding is applied.

Polyester, epoxy, or silicone resins are used most often as impregnating materials for the treatment of stator windings. In this case, silicone resin of high thermal endurance able to withstand $\vartheta_{max} > 225^{\circ}\text{C}$ is used for machine II. The winding diagram of the stator is, as shown in figure 6.4. Three thermocouples are embedded in the stator winding in each machine, two in the phase winding, and one at the end winding.

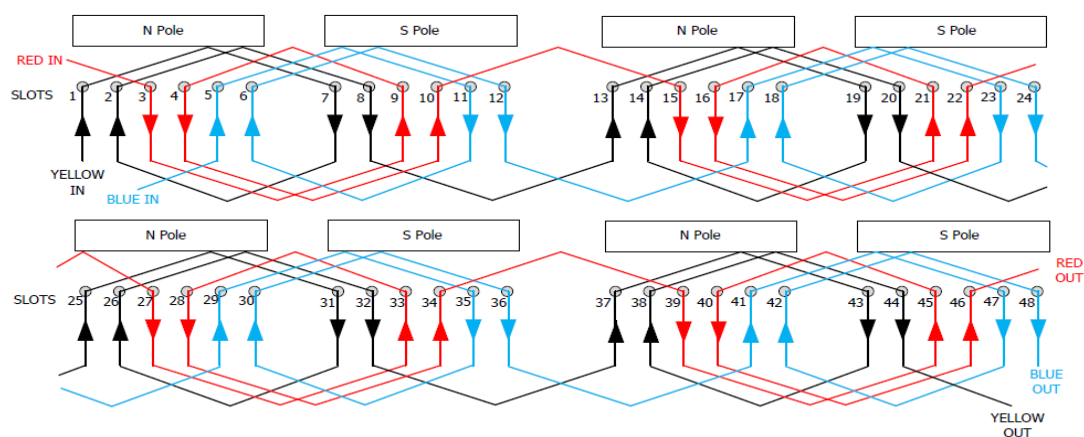


Figure 6. 4 Winding diagram

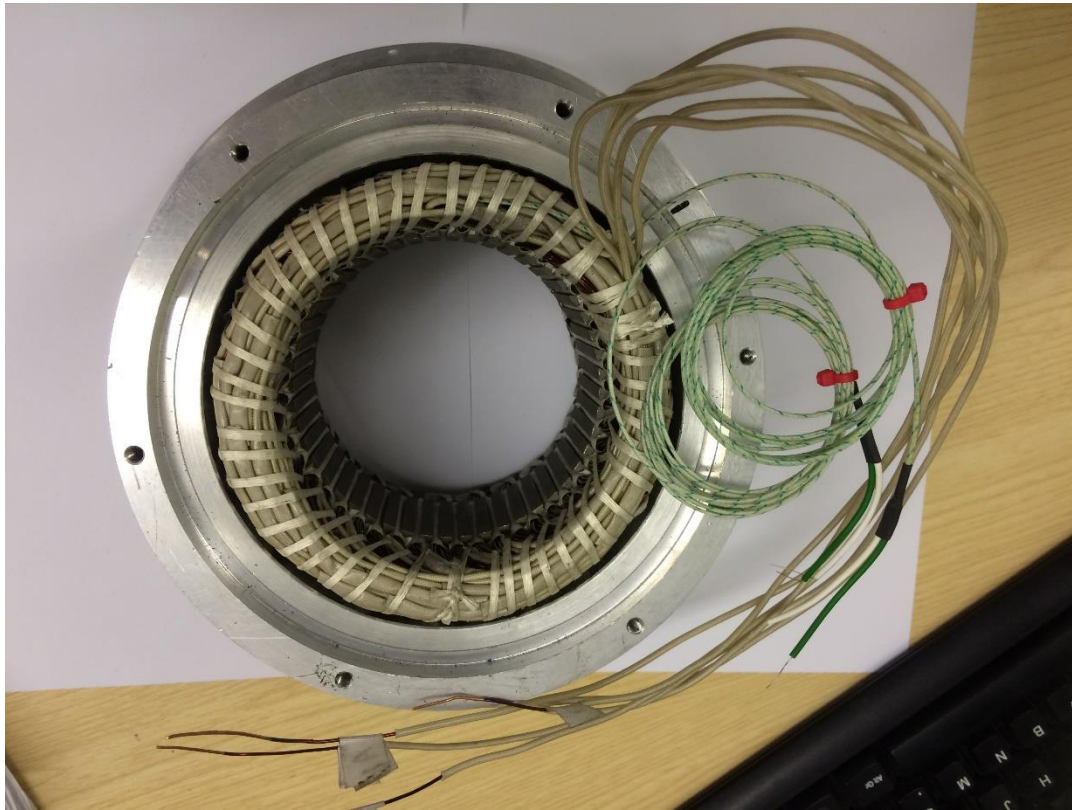


Figure 6. 5 Stator winding for machine I

6.4.1 *Insulation life expectancy*

There are two sources of failure in a motor: either electrical or mechanical failure. Electrical failure happens due to the weakening of the insulation, which occurs typically due to stator coil and slot liner insulation degradation. This problem will lead to an inter-coil or a coil to ground-wall short. Therefore, to overcome this problem, it is essential to choose suitable stator slot wall insulation, and the motor's operating temperature and voltage should be taken into consideration.

Both machines use Nomex type 410 for slot liner. For machine II, Nomex 5 is used with a thickness of 0.13mm. The temperature range for the experiments will be between 220°C to 320°C. The Nomex insulation liner can maintain 12kV/mm dielectric strength for several hours, and the expected life of the insulation can be estimated by referring to figure 6.6. Thinner Nomex will have slightly lower conductivity compared to thicker insulation.

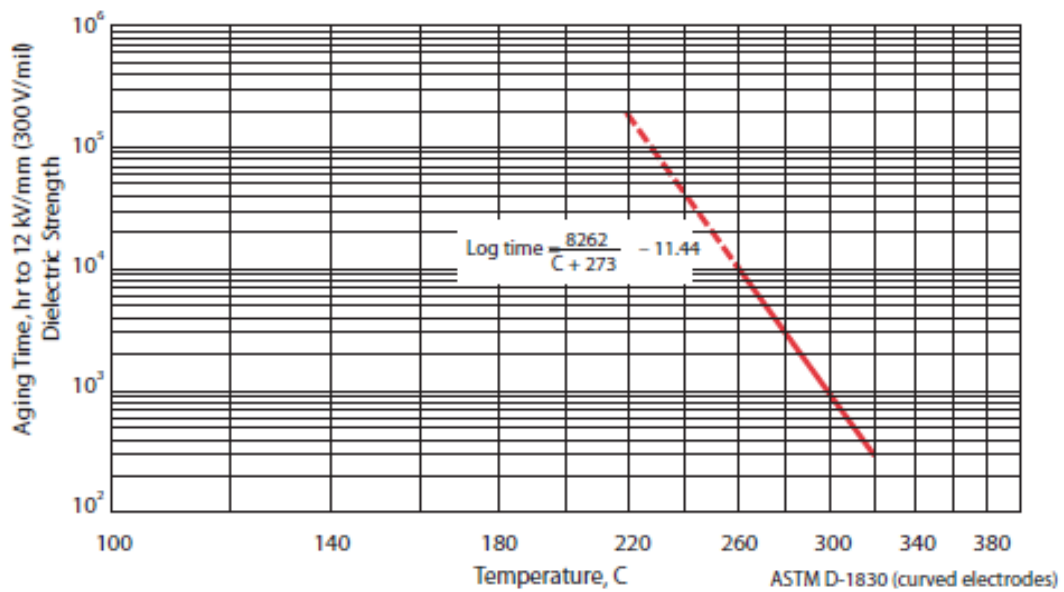


Figure 6. 6 Nomex type 410

6.4.2 Thermocouple

A type K thermocouples have been used to measure the temperature of parts of the machine. The temperature range is between -75°C to $+250^{\circ}\text{C}$. The thermocouples are connected to a data logger that can display and save the temperature data of each essential part. During the testing of the machine, the temperature needs to be monitored to make sure that the machine is not running over the temperature limit, especially at the stator winding. Thermocouples have been located at the end winding, end slot, middle of the slot, stator laminations, and housing. Figure 6.7 shows the thermocouple at the end winding.



Figure 6. 7 Location of thermocouple sensor

6.5 Water cooling jacket

Cooling jackets embedded in the housing have become common in medium-power electrical motors. This type of cooling is designed to remove the heat lost at the stator copper winding and the stator iron, thereby preventing the propagation of heat towards the rotor. Liquid cooling enhances heat transfer, thus enabling higher current density and total loss to achieve higher power and torque density.

A water-based cooling system has several benefits over air-based cooling systems, such as high efficiency due to the high heat capacity of water and its high heat transfer coefficient [69]. Figure 6.8 shows the water jacket that has been designed for the prototype machines. It is crucial to make sure that the water jacket can work properly to avoid water leaking, especially at the water inlet and outlet area.

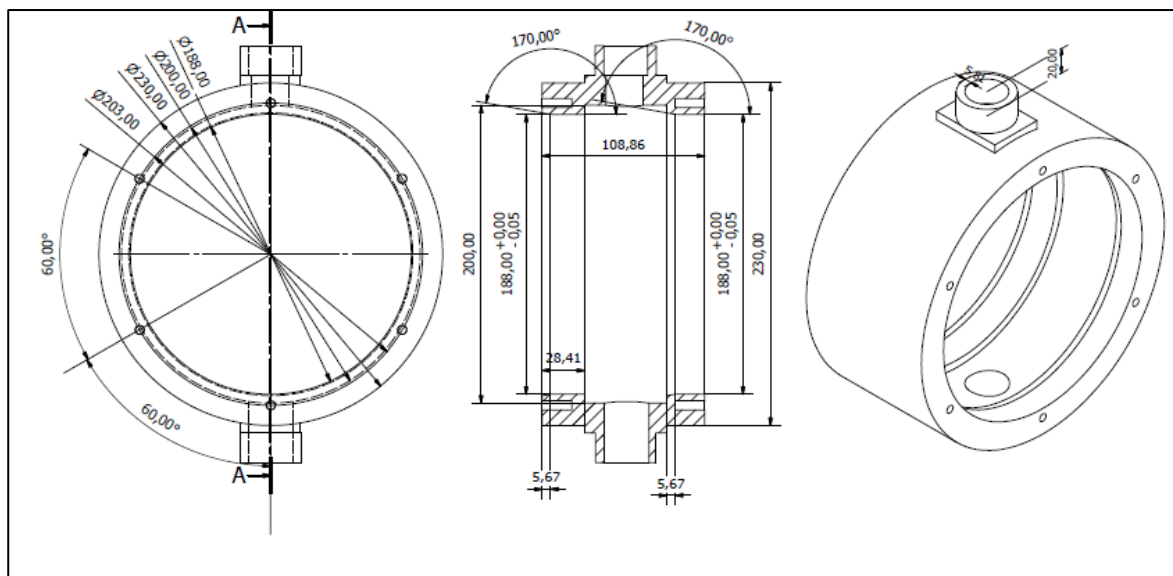


Figure 6. 8 Water Jacket

6.6 Test rig description

The test-rig used for the prototype machines comprises the following main components: DC power supply, data logger, torque transducer, power analyser, and chiller.

Static torque measurements were carried out on the machine by using the test rig, as shown in figure 6.9. The torque transducer is used to measure the torque value and to change the mechanical angle of the rotor. Then, the data logger records and displays the torque value. Meanwhile, the Magtrol torque transducer is placed on the shaft. The thermocouples were connected to the data analyser and connected to the software to record the temperature of the machine during testing.

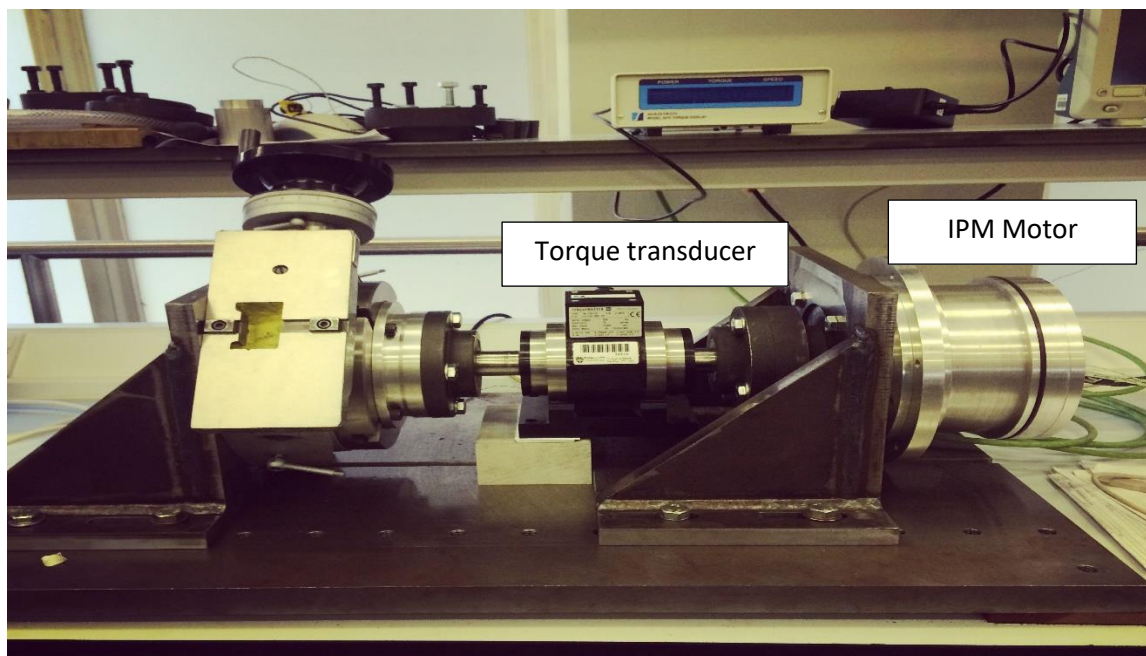


Figure 6. 9 Test rig

Figure 6.10 shows the full test rig includes a programmable power supply that used to supply the DC and voltage to the prototype machines. The maximum DC voltage is 100V with 45 Amps. The input current needs to be programmed first before connecting to the prototype machine. A suitable torque transducer was chosen to achieve the torque for the machine. Transducers with different values of torque will have a different diameter of the shaft connector. Therefore, it is essential to specify the type of torque transducer to be used before design the shaft of the prototype machine. The position of the rotor can be determined by spinning it at the end of the shaft transducer. The static torque value is taken with different angles of the rotor.

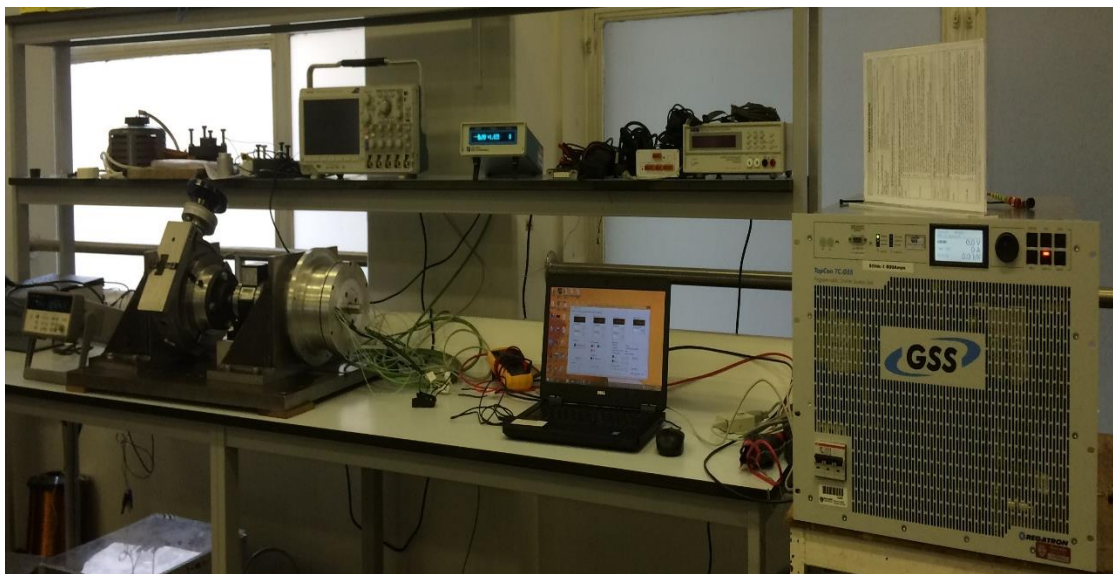


Figure 6. 10 Full test rig of static torque test

Thermal testing of the prototype motors has also been conducted. A chiller has been used to supply the water coolant into the water jacket. A digital flow meter is used to measure and adjust the flow rate of the water coolant from 1litres/min to 15 litres/min, as shown in figure 6.11. The meter was installed between the chiller and the water inlet on the prototype machine. Meanwhile, figure 6.12 shows the thermal testing rig. However, the coolant flow rate for the Nissan LEAF is 8 litres/min.



Figure 6. 11 Digital flow meter

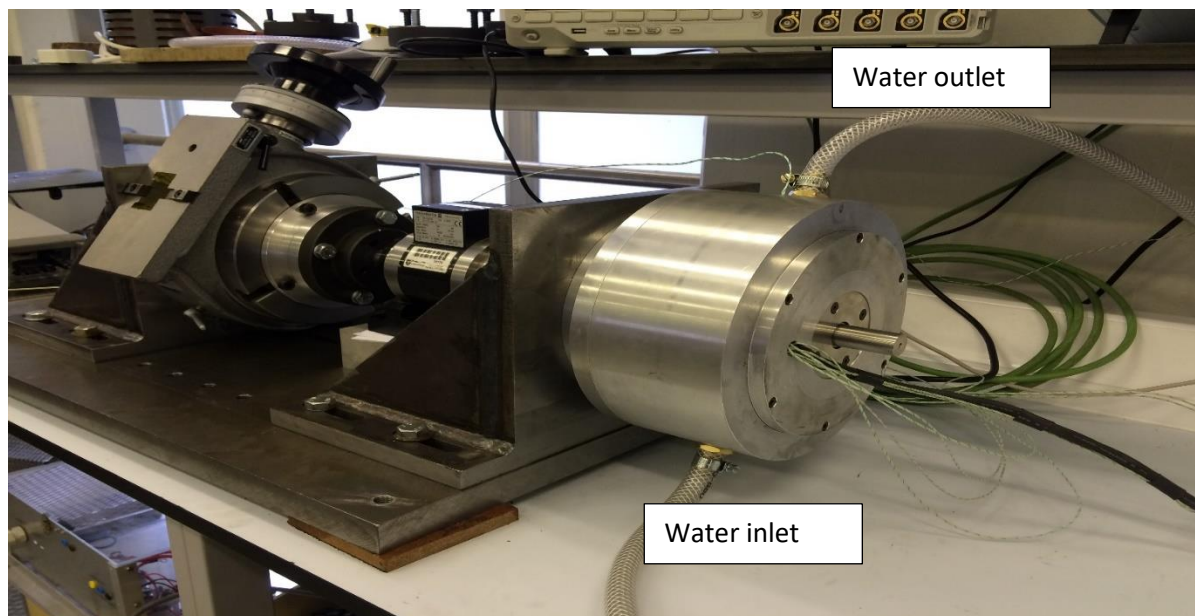


Figure 6. 12 Test rig for thermal testing

6.7 Summary

The materials used to build the prototype motors and the components of the test rig have been briefly described in this chapter. The prototypes of both machines have been developed, and the static torque measurements will be verified against those predicted using 2D FE analysis. The thermal characteristics of the prototype machines are determined and presented in the next chapter.

Chapter 7

Testing and Performance Analysis of Prototype Machines

The proposed smaller IPM motor, which is suitable for electric vehicle demand, was developed, as described in Chapter 4. The effect of using different types of permanent magnet, rotor, and stator lamination has also been analysed in Chapter 5. Meanwhile, the construction of the prototype machine has been discussed in Chapter 6. Therefore, in this chapter, the experimental setup and a comparison between FEA simulations and experimental results are presented. Also, by comparing the FEA simulation and experimental results, the torque value, resistance, and thermal characteristics are validated.

As mentioned in Chapter 6, two prototype machines have been developed and tested. Both machines have the same topology but are of different sizes. The machine I was constructed with the same materials used to build the existing Nissan LEAF; meanwhile, machine II was constructed using high-temperature materials to allow the machine to run safely at higher temperatures. Machine II was designed to be smaller than the machine I to show the capability of machine II to achieve the same output as the machine I and at the same time to run safely at high temperature.

7.1 Static at no load

Both machines were constructed with three-phase single-layer distributed winding at the stator with eight poles and 48 slots. The stator core for the machine I was built from M270-35A lamination sheets, and each tooth was wound with 50 turns, while machine II was constructed from Hiperco50 and had 62 turns per slot. After the coils were inserted into the stator of the tooth, a test was conducted to detect if any faults such as a short-circuit or an open-circuit of the coils occurred. This method is also crucial to identify the phase connection. Therefore, before the rotor was put in its place, the measurement was usually taken first. Measurement was also conducted to check the polarity and phase of the coils.

The resistance of the coils for each phase can also be measured directly by using a multimeter. However, resistance can be estimated first using a calculation. To calculate the resistance of the coils, the equation below is used:

$$R_{DC} = \frac{2 \times N \times l_a \times \rho_c}{A} \quad (7.1)$$

where A is the conductor cross-sectional area, N is the number of turns, ρ_c is electrical resistivity of copper and l_a is the length of the wire.

The values of resistance are shown in table 7.1. The measurements were conducted at room temperature, 25°C. The predicted resistances were 6% to 10% higher than that measured. The estimation of the total length of wire attributed the difference in measured and calculated. Resistance for machine B is higher than machine A. Meanwhile, the difference in resistance between phases was only 1%. Higher temperatures will increase the value of resistance.

Table 7. 1 Predicted and measured resistance values in different phases

	Machine I (Ω)	Machine II (Ω)
Predicted resistance (Ω)	3.2	5.41
Measured resistance (Phase A) (Ω)	2.9	5.1
Measured resistance (Phase B) (Ω)	2.85	5.0
Measured resistance (Phase C) (Ω)	2.91	5.0

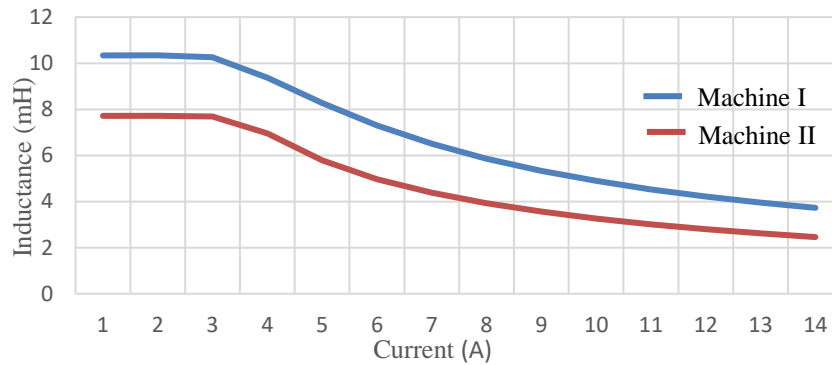
Meanwhile, from the 2D FE model, the calculated inductance can be defined without taking into account end effects. The inductance can also be measured from the coils by putting a DC source in one of the phases and then locking the aligned rotor mechanically. Then, a variable frequency voltage source is fed into the winding for measurement. To measure q-axis inductance, the same approach is used, but the rotor is rotated by 45 (or 180/p) mechanical degrees from the d-direction. The apparent power (S) and power factor ($\cos \delta$) are measured directly, and the equations below are used to calculate d- and q- axis inductances at different frequencies:

$$L_d(f) = \left[\frac{S_d \sqrt{1 - (\cos \delta)_d^2}}{(2\pi \cdot f) I_d^2} \right] \text{ (H)} \quad (7.2)$$

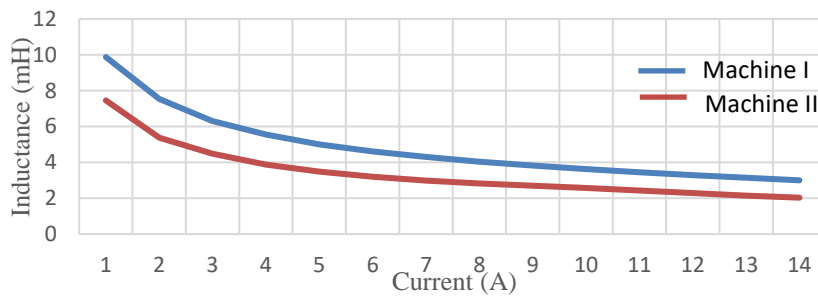
$$L_q(f) = \left[\frac{\sqrt{1 - (\cos \delta)_q^2}}{(2\pi \cdot f) I_d^2} \right] \text{ (H)} \quad (7.3)$$

where S_d and S_q are the apparent power measured in the d- and q- directions, $(\cos \delta)_d$ and $(\cos \delta)_q$ are the power factors measured in the d- and q- directions, and wf is the winding factor.

The calculated inductances, L_d , and L_q for both machines at a frequency of 166.7 Hz are shown in figure 7.1 (a) and (b). Both figures show that the value of inductance for the machine I is higher than machine II.



(a)



(b)

Figure 7. 1: (a) Inductance, L_q for the machine I and II, (b) Inductance, L_d for the machine I and II

7.2 Static torque for the machine I

A static torque experiment was conducted to compare measured torque with finite element predicted torque accurately. The torque was measured by varying the value of the current. The static torque of the prototype machine I was tested with a voltage of 63 V and a current density of 25 A/mm². For safety reasons, the current was injected from small to larger values. The connection of the coils was as shown in figure 7.2 to measure the phase current. Current applied to the winding varied from 1 amp to 14 amps.

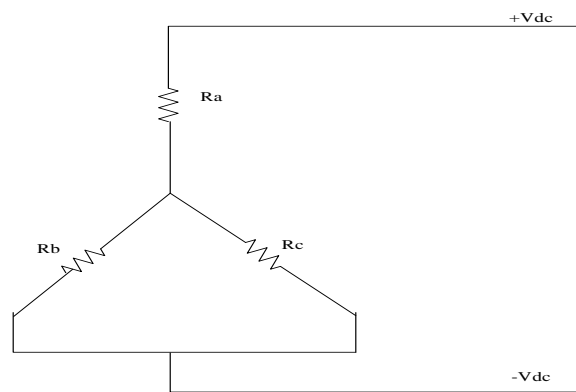


Figure 7. 2 Connection of the power supply to the winding

Figure 7.3 presents the static torque produced by FEA, while the measured static torque is as shown in figure 7.4. When a higher current was injected, the torque increased gradually. The results show that the measured torque is more elevated than torque produced from FEA. Besides, at an electrical angle of 58°, the values of torque from the experiment are the highest. However, a different phenomenon occurred in the simulation result. The highest value of torque was produced at the electrical angle of 32°. The torque then decreased at an electrical angle of 58° and increased again after that. It is assumed that simulations involved numerical model with the aid of computer software. At the same time, experiment analysis represents the real-life measurement of materials and sometimes have errors due to measurement and faulty equipment. Therefore, obtaining the correct results from an experimental set up is a challenge. The rotor needs to be turned around following the degree position to get the torque value from the experimental. Maybe the faults occur during this process.

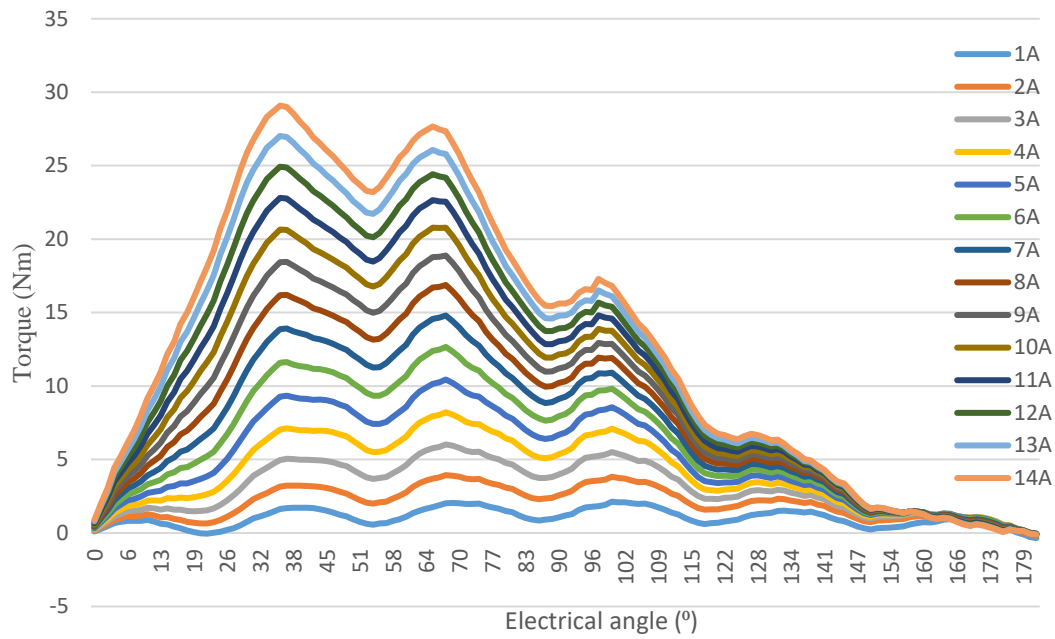


Figure 7.3 Static torque for machine I (FEA)

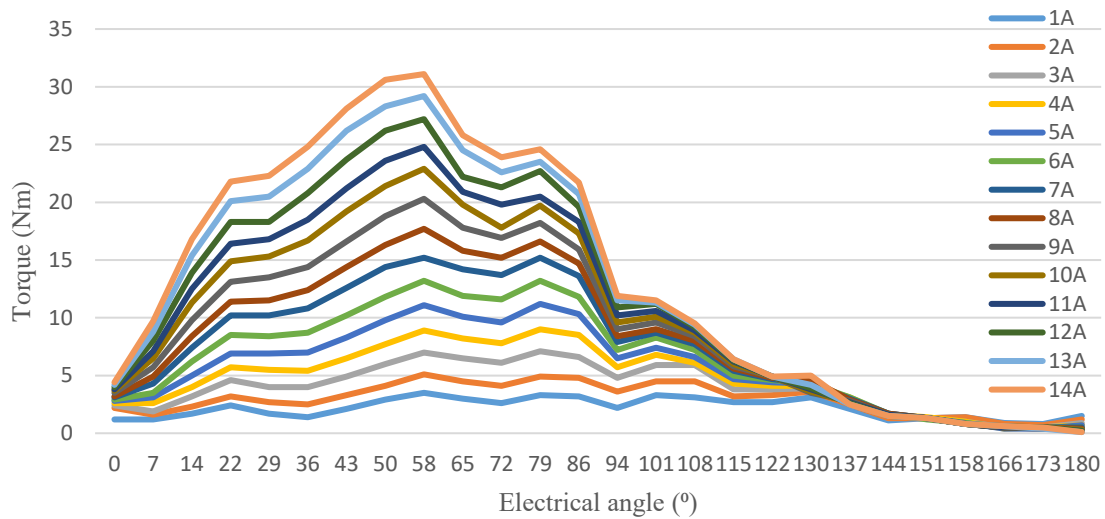


Figure 7.4 Static torque for machine I (measured)

As mentioned before, the torque produced by the machine increased significantly with the current. Figure 7.5 shows that the torque value from the simulation results is higher than those from the experimental. The difference in torque between the experimental and simulation results is between 1.31Nm to 2.02Nm.

Table 7. 2 Torque value for the machine I

DC current (Amps)	Torque (Nm)	
	Simulation	Experimental
1	1.63	3.4
2	3.15	4.9
3	4.96	6.7
4	7.03	8.7
5	9.28	10.6
6	11.59	12.9
7	13.89	15.9
8	16.18	17.9
9	18.44	20.5
10	20.65	22.9
11	22.81	24.9
12	24.93	26.7
13	27.02	28.5
14	29.08	31.2

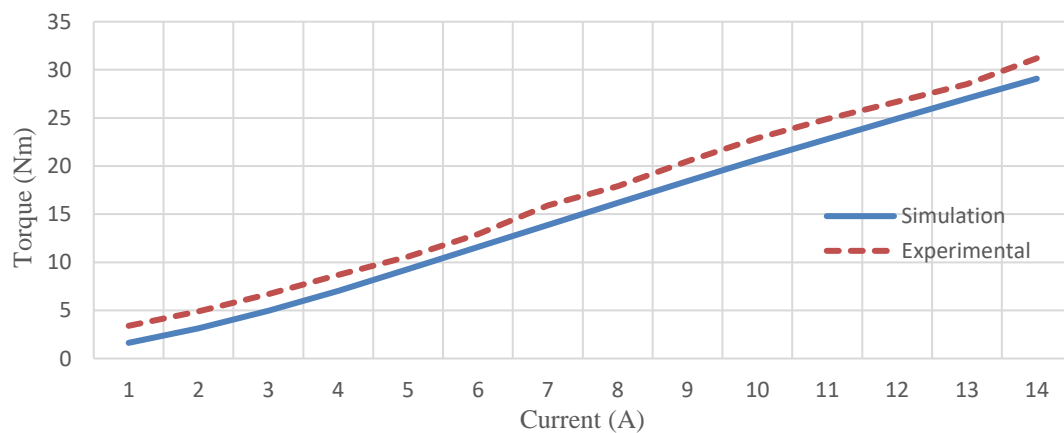


Figure 7. 5 Maximum torque for the machine I at electrical angle 32°.

Figure 7.6 presents a comparison between the simulation and experimental results of the torque values. The static torque can be produced directly by simulation. Meanwhile, for the experiment, 14 amps DC current was injected, and measurements were taken with different electrical angles of the machine. The results show that, even though the amplitude discrepancy between the result from the simulation and experiment is about 7.3%, the results for simulated and measured torque show good agreement in terms of both amplitude and waveform.

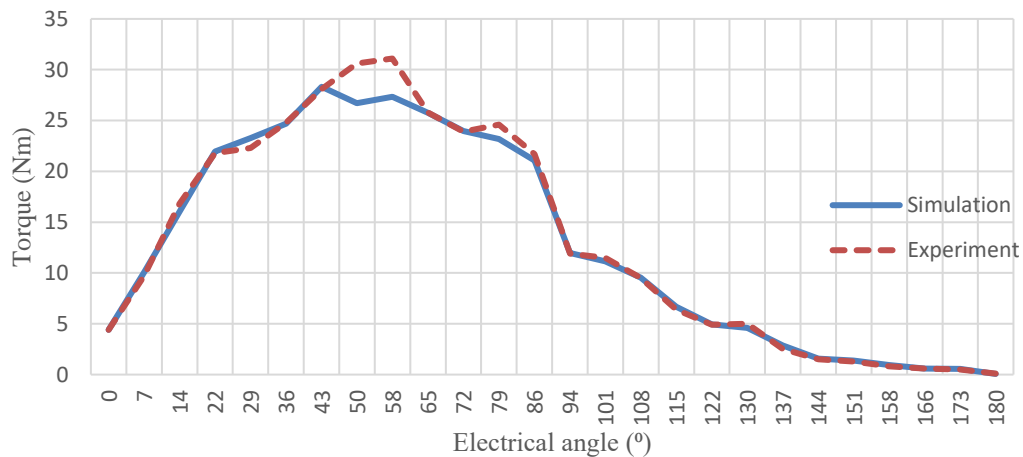


Figure 7. 6 Static torque for the machine I at 14A DC current.

7.3 Static torque for the machine II

The same method was applied to machine II to measure torque. The current was injected starting from 1 amp until the maximum current density reached was 25 A/mm². The maximum torque values are as shown in table 7.3. By comparing the torque results between the simulation and experiment, again, the experimental value is higher. The smallest difference in torque produced between these two methods of measurement was 0.2Nm; meanwhile, the most significant difference was 2.1Nm.

Table 7. 3 Torque value for machine II

DC current (Amps)	Torque (Nm)	
	Simulation	Experimental
1	0.54	2
2	1.29	3.4
3	2.303	4.2
4	3.55	5.1
5	4.95	6.2
6	6.48	7.2
7	8.06	8.5
8	9.6	9.8
9	10.96	11.2
10	12.18	12.5
11	13.39	14.1
12	14.52	15.3
13	15.47	16.2

The static torque comparison for machine II is illustrated in figure 7.7. The same phenomenon as in the previous case was found. The highest torque for the results from both simulation and experimental values was at an electrical angle of 44° , and the experimental machine produces slightly higher torque output than the simulation.

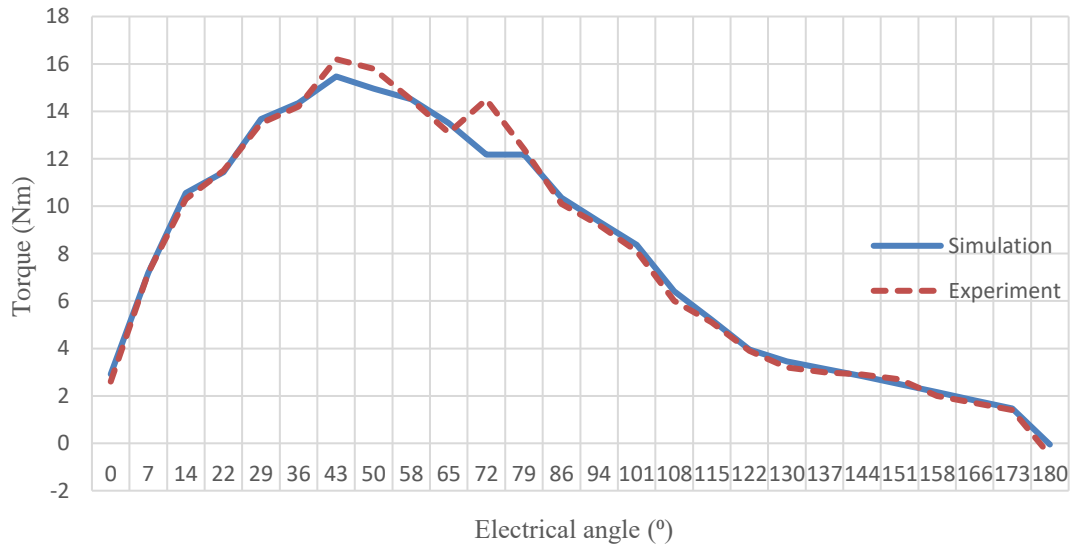


Figure 7. 7 Static torque for machine II

The permanent magnets used for machine II were made from samarium cobalt (Recomm 33E) produced by Arnold Magnetic Technologies. As with the simulation results, with the same current value the torque produced by machine II was lower than that in machine I. This result also proves that with the equal amount of DC current injected in different machines, the machine I will produce higher torque than machine II because, technically, neodymium-iron-boron has a better magnetic performance than samarium cobalt. The comparison is shown in table 7.4. For this prototype machine, machine II needs approximately 66% higher DC current to get the same output torque. However, prototype machine II was built smaller to show that this machine can run at high temperatures. To produce 12.5 Nm of torque, the machine I needs at least six amps DC current while machine II needs approximately ten amps. Therefore, for the machine that has been developed, the maximum torque that machine I can produce is 30 Nm. However, for machine II, the maximum torque that the machine can provide with the maximum current density of 25 A/mm^2 is 16.2 Nm. This is almost half the torque value of that for machine I. Machine II would need a bigger diameter and a different type of wire to make sure that a higher current density can be applied to the winding and that it can work safely even at high

temperatures. However, from the simulation results, with 20 amps DC current injected, machine II will produce 30 Nm.

Table 7. 4 Torque value for both machines

DC current (A)		Torque (Nm)
Machine I	Machine II	
3	5	6.2
6	10	12.5
7	12.5	16.2
14	20	30

7.4 Thermal characteristics

The prototype machine was tested without load at room temperature, 25°C. However, the initial temperature for existing Nissan LEAF is 65°C. There will be some conflicts occur due to the different initial temperature. Still, all the simulation results will use 65°C as initial temperature. The machine was operated with different current values and powered by a fixed voltage. The machine was also tested at different temperatures. Coil resistance was found to increase when the temperature rose. The value of coil resistance at high temperature was almost three times than that at room temperature. To get the desired output, the voltage was changed, and the current values were found to increase with temperature.

This testing was carried out to observe the thermal behaviour of the prototype machines. Thermocouples were used to measure the temperature at different locations on the machine such as stator housing, coils, end winding and stator laminations. The thermocouples used were type K with a temperature operating range from -40°C to 300°C with a +/- 5% tolerance. A data logger interfaced the thermocouples with the computer to record the measurements. The temperature data was logged and stored with a specific incremental logging time of the 20s. Both machines were impregnated using varnish, which commonly used for stator slot filing and end-winding bodies.

Figure 7.8 shows the temperature rise for machine II at different locations. Testing has been conducted for almost 1120s with ten amps DC current. Without coolant being applied, the temperature continuously increased. The experimental results show that the end-winding produced the highest temperatures compared to other regions and the lowest temperature was at the housing. The temperature at the end-winding area is higher than in the slot region because the end-windings are surrounded by air instead of stator steel, and the atmosphere is an inferior heat-conducting medium compared to steel. In the beginning, the temperature at stator lamination was lower than the temperature at the winding. However, after 240s, the temperature here started to increase and reached temperature as the winding.

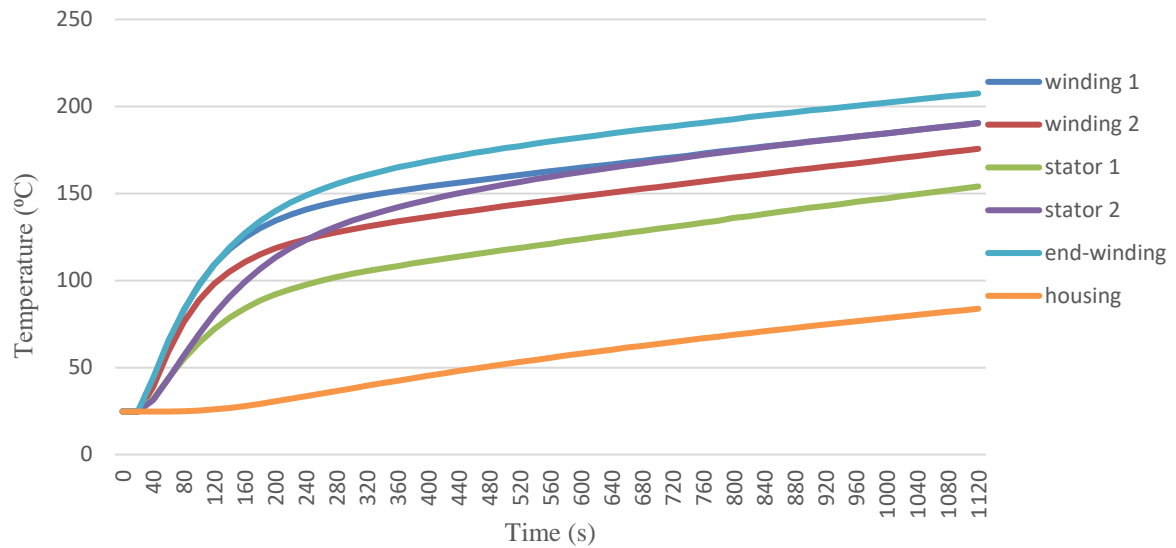


Figure 7. 8 Temperature rise for machine II without coolant

The same pattern of thermal behaviour occurred on the machine when the water coolant was applied, as shown in figure 7.9. However, after the 360s, the temperature started to become saturated and remained the same. The temperature at the end-winding was reduced by approximately 48% when 15 litres/min water was pumped through the water jacket around the outer stator. The temperature at the housing was maintained at 20 to 22°C because the temperature of coolant was set at 22°C. As a result, at the 1080s, the temperatures had decreased by almost 50%.

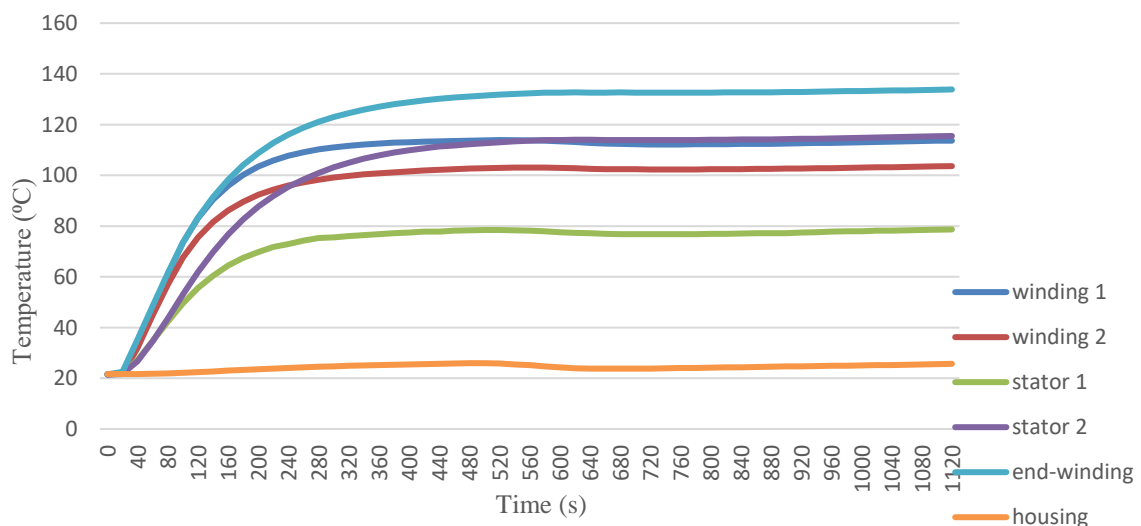


Figure 7. 9 Temperature rise for machine II with coolant

7.4.1 Thermal behaviour of machine I

The testing of thermal characteristics was conducted by applying various current values. However, the amount of current used should not exceed the maximum current density of 25 A/mm². Therefore, for a machine with an injected current of 6 amps, the torque value was 12.5 Nm, and for 7 amps the torque was 16.2 Nm as shown in table 7.3. Figure 7.10 below shows the temperature rises at the end-winding for the machine I without coolant. For safety reasons, the test was stopped if the end-winding temperature rose close to 200°C to prevent the coil from damage because the maximum operating temperature for the coil is 200°C. It was also to avoid irreversible demagnetisation of the magnet. It can be seen that the end-winding temperature for 7 amps kept increasing until the 2160s and did not show any sign that it would decrease.

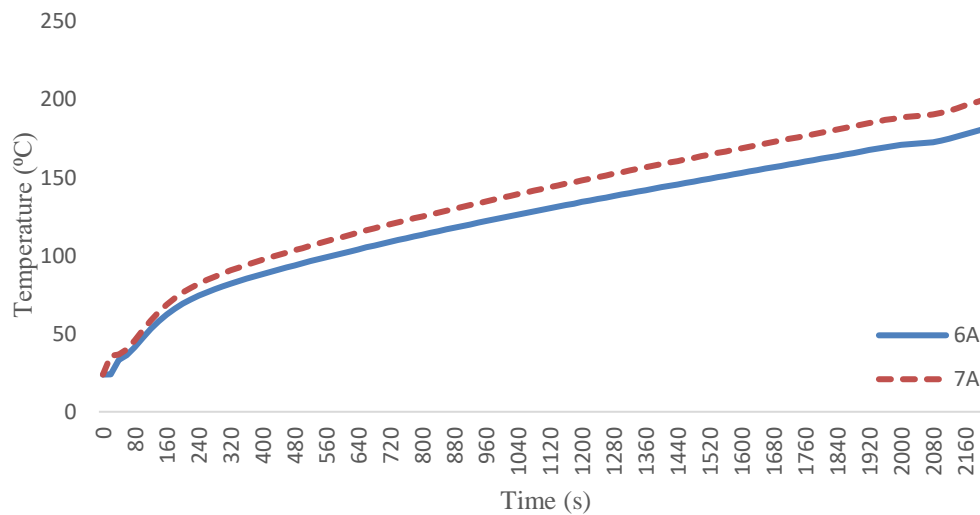


Figure 7. 10 Temperature at end-winding for machine I

Therefore, to overcome this problem and in order to prevent the failure of the machine and irreversible demagnetisation of the magnet, the next test was conducted with coolant applied to the outer stator of the machine. For this test, tap water was chosen as the coolant. The coolant was pumped at different flow rates of 10 and 15 litres/min and maintaining an inlet temperature of 22°C. Figure 7.11 shows the effect of injecting the coolant in the water jacket. No significant difference in temperature resulted from changing the flow rate of machine cooling from 10 litres/min to 15 litres/min. Therefore, this machine can use either flow rate.

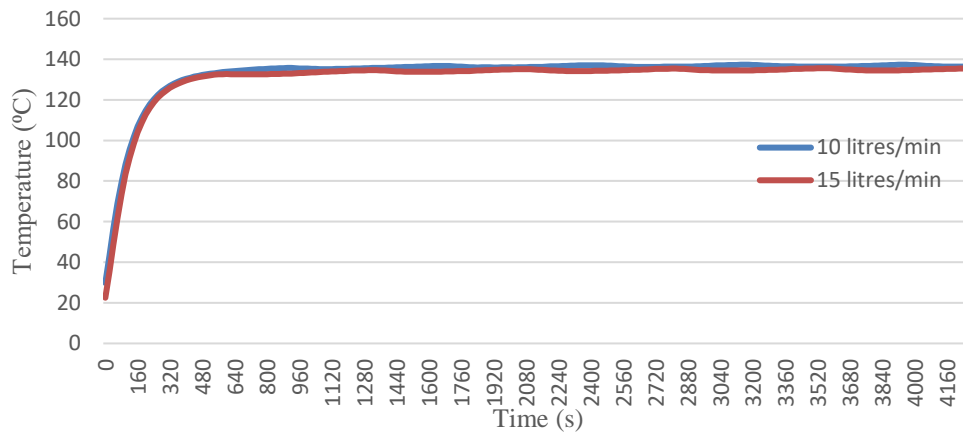


Figure 7. 11 Effect of pumping different flow rate of water coolant

A significant difference was found in the thermal behaviour on the machine I after the coolant was applied. In the beginning, the temperature kept increasing, and only after 300s, the temperature starts to become saturated and then remained stable even after 2 hours. Figure 7.12 shows that the temperature for 7 amps applied current did not even exceed 120°C, and for 6 amps used current, the temperature stays below 60°C.

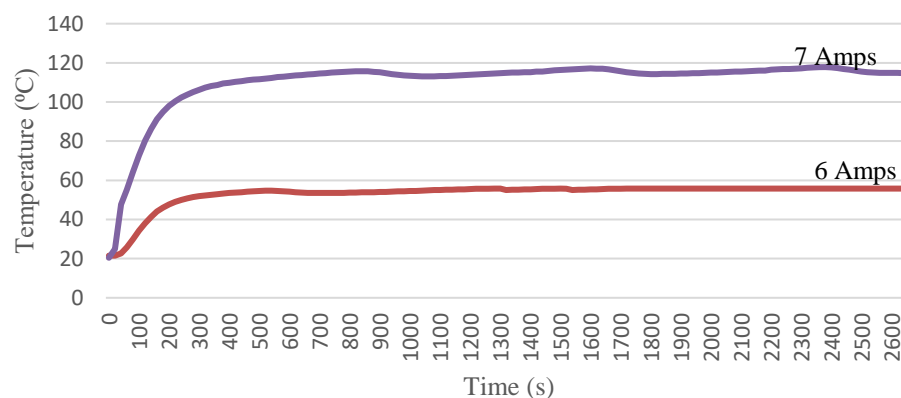


Figure 7. 12 Temperature at end-winding for the machine I with water coolant

7.4.2 Thermal behaviour for machine II

The same test has also been conducted on machine II, where various current values were applied to the machine. Machine II was built with high-temperature materials, and the rotor and stator laminations are made of Hiperco50 alloy, which exhibits high magnetic saturation, maximum permeability, and low AC core loss and can be used in high temperatures up to 1720°F. Meanwhile, for the permanent magnet, Recomma 33E was used to make sure that the machine can run safely at high temperatures. Samarium cobalt is very well known for its capability to operate at higher temperatures, and it is the best choice to replace neodymium-iron-boron as permanent magnet material. Even though the electromagnetic simulation results showed that, in comparison, neodymium-iron-boron has better performance than samarium cobalt, in terms of temperature, samarium cobalt is the better choice.

As mentioned above, machine II was built to be smaller than the machine I to show that it can still run safely even at high temperature. Therefore, machine B needs more DC current to achieve the same output as a machine I, as shown in table 7.3. The smaller size and higher DC current mean that machine II becomes warmer than the machine I.

Figure 7.13 presents the temperature rise at end-winding for machine II with and without coolant. With a DC current of 10 amps applied to the machine, it can be seen that, without coolant, the temperature at the end-winding keeps increasing until it reaches the temperature limit. The highest temperature allowed for the winding is 240°C. When the coolant was applied to the machine, the temperature was reduced and maintained at 120°C. However, when only 5 amps DC current applied to the machine, the temperature only increased slightly and took much longer to reach the temperature limit.

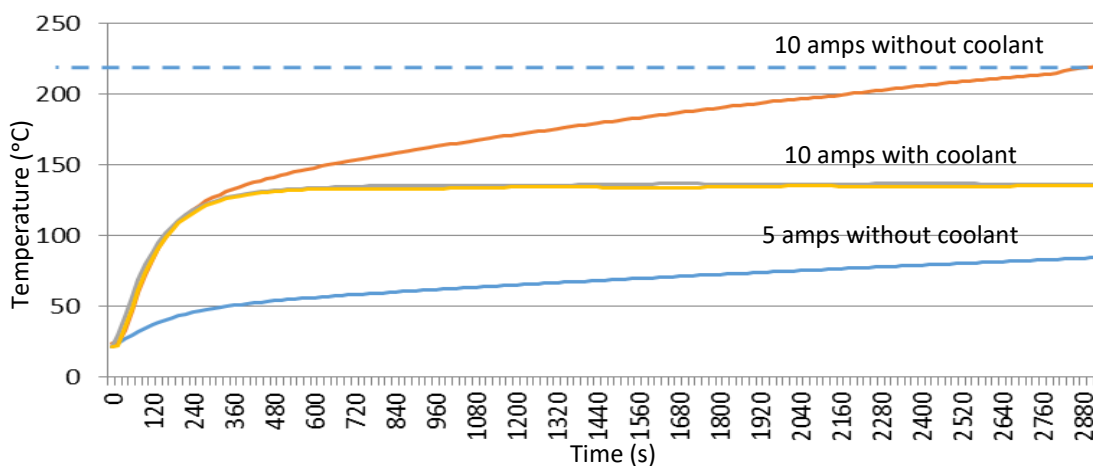


Figure 7. 13 Temperature rise at end-winding for machine II

Figure 7.14 also shows the temperature rise at the end-winding for machine II with and without coolant. Testing was conducted with the DC current at 12.5 amps and a voltage of 120V. Without any coolant applied to the machine, the temperature continues to rise. After the 1500s, the temperature at the end-winding was almost 250°C. In the beginning, Kulgrid HT Magnet wire was chosen because this wire can stand temperatures up to 537°C. However, due to problems that occurred during the winding process, Magnetemp Y-240 was decided instead to replace the coil. Magnetemp Y-240 can only stand temperatures up to 240°C. Therefore, the testing needed to stop if the temperature reached that limit. In this case, higher DC current could be applied to machine II if the correct diameter and type of wire were chosen.

The testing was repeated with the same DC current applied, but this time with coolant. A rate of 15 litres/min of water coolant was pumped through the water jacket, and as a result, at 420s the temperature at the end-winding stopped increasing and stayed at the same temperature even after the 1500s. The temperature was reduced to 160°C, which is less 20% than the temperature without coolant. It can be concluded that the water coolant is essential for this machine and changes its thermal behaviour, especially at the end-winding.

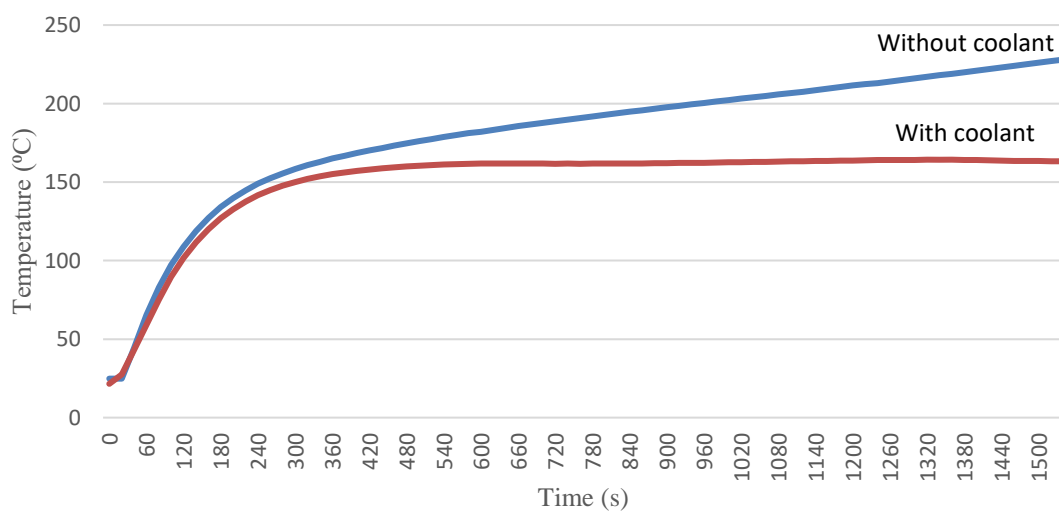


Figure 7. 14 Temperature rise at the end-winding for machine II at 12.5 amps

Figure 7.15 shows the predicted temperature at the coil and permanent magnet from the simulation result for machine II with the initial temperature 65°C. When 12.5 amps DC current was applied to the machine, the torque was 16.2 Nm. The predicted temperature at the end-winding did not exceed 210°C. Meanwhile, the expected temperature at the permanent magnet remained below 120°C. The predicted temperature was higher than the real measured temperature. However, to prevent failure and the demagnetisation of the machine, it is wise to make that kind of assumption.

Even though the experiment could not be conducted with 20 amps applied, because the maximum current density would be exceeded, a simulation was conducted to predict the temperature rise, as shown in figure 7.15. The results show that machine II could produce 30 Nm of torque with a predicted temperature at the end-winding of 260°C, while the temperature at the permanent magnet would stay below 150°C. Therefore, if wire that can stand high temperatures up to 537°C was wound, machine II could still produce higher torque than the machine I because the temperature at the permanent magnet would be far away from the temperature limit of Recomma 33E.

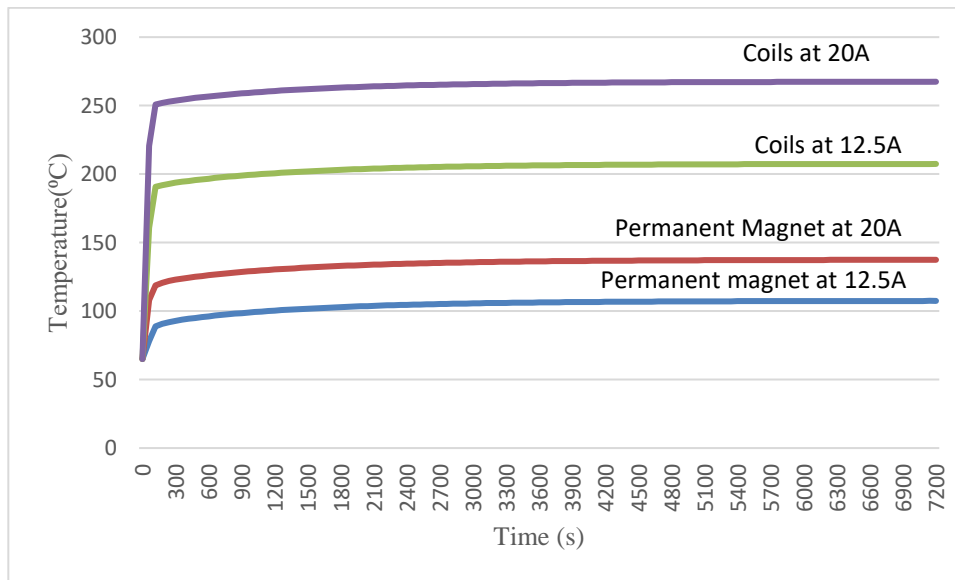


Figure 7. 15 Simulation results for machine II

Besides improving the thermal behaviour when the machine is running, the water coolant can also improve the cooling time when the machine stops running. It can be seen in figure 7.16

that the temperature decreased when the machine stopped running. Without coolant, a longer time was needed for the machine to reach room temperature. However, with coolant, the machine reaches room temperature faster.

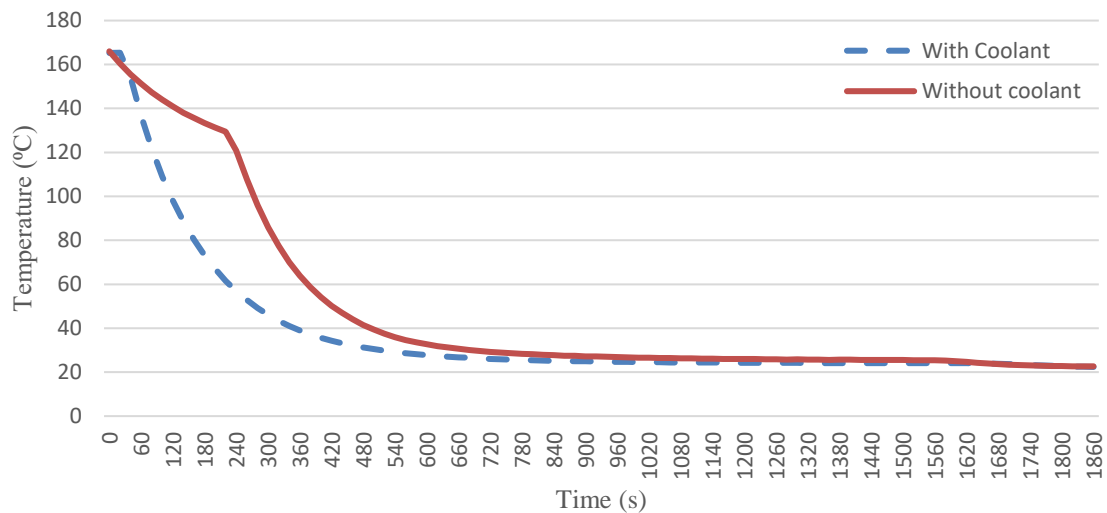


Figure 7. 16 Temperature cooldown at the end-winding for machine II

7.5 Summary

The calculated phase resistances for both machines are up to 10% smaller than the phase resistances measured directly from the machines. The prototype machines operated at no-load conditions at various currents. It was very challenging to measure the thermal behaviour accurately in different parts of the machine. The differences between the simplified simulation model and the real-world motor are the key factors explaining the minor error compared to the experimental results. The predicted temperatures were higher than the measured temperatures.

From the simulation results, machine II could produce higher torque if a suitable diameter and type of wire were used. Unfortunately, the wire chosen to replace Kulgrid HT Magnet wire could only stand temperatures up to 240°C. Therefore, this circumstance makes a limitation on practical measurement. If the wire can stand up to 570°C or more, the machine II can achieve the same output torque as the machine I.

Chapter 8

Conclusions and Recommendations for Future Research

Two competing permanent magnet motors have been studied in this thesis through simulation, prototyping, and testing. Different materials were used for both motors. The first motor was built using the same materials used in the existing Nissan LEAF, while the second motor was built using materials better suited to a higher temperature. The second motor is smaller than the first.

To come out with the smaller size that suits the electric vehicle applications, a review of the design of the existing Nissan LEAF permanent magnet motor has been carried out. The output of the motor has been studied. The effect on the performance of a reduction in size investigated. The smaller motor maintained the same topology (pole number, magnet, and tooth angular span and arrangement) with reduced dimensions. The aim being a smaller, hotter running motor that can achieve the same performance; 280 Nm and 80 kW. Simulation has been done on a few sizes of the machine with the same machine's topologies and materials. JMAG software has been used to analyse the electromagnetic output of each motor.

A new smaller size of IPM motor with a combination of high-temperature materials has been determined in this study. The scale has been shrunk to 10% from the existing one. With high-temperature materials applied on the motor and temperature predicted, the motor met the entire requirements and therefore is an excellent alternative to the existing motor, which are widely used nowadays.

However, to achieve the same performance as the existing Nissan LEAF, a smaller motor will need a greater MMF. In general, a smaller motor will produce higher losses. Therefore, the temperature rise will be higher too. This study has shown that a smaller motor needs more attention to thermal management to prevent failure. Thermal modelling was applied to both motors to determine the temperature rise in the critical components of the motor.

Therefore, a one-way coupled analysis from 3D transient with motion magnetic analysis to thermal analysis is conducted to calculate the transient temperature to predict the temperature

rise on the few essential parts in the motor. In this case, the limitation of the design can be determined. It is crucial to predict the temperature to make sure that the temperature rise on the motor is still under the limitation before reducing the size of the motor. There is a difference in the predicted and measured temperatures. Typically, the measured temperature rises are lower, indicating that further research could be carried out to close the gap, which would then allow for an even smaller motor design running even closer to the motor's windings permanent magnet thermal limits. This approach would benefit potential manufacturers. The difference between the calculation and measurement is mainly due to the error between the position of the calculated point and measured point, the imprecise calculation of some thermal convection resistances, the simplified thermal model, and others.

The original Nissan LEAF applied 8 litres/min for the flow rate of the coolant. However, in this study, a water jacket contains the coolant, and the flow rate of the coolant is 10 litres/min is applied on the motor because by reducing the inlet coolant temperature and increasing its flow rate, the efficiency of a machine with liquid cooling can be improved. With the water jacket applied, the temperature in the motor is reduced to 40% compared to the motor without any coolant.

Besides, to avoid the demagnetisation of the permanent magnet, samarium cobalt has been chosen to replace neodymium-iron-cobalt. The reason is the existing permanent magnet will start to demagnetise at 140°C. Meanwhile, samarium cobalt can stand up to 350°C before starting to demagnetise. Therefore, permanent magnet motors with the same topologies were designed and analysed in terms of electromagnetic performance and thermal behaviour. In terms of both cost and flux density, a PM with NdFeB will perform better than one with SmCo. However, when it comes to temperature distribution, especially for smaller motors, as proposed in this study, NdFeB has limitations. Therefore, to avoid the demagnetisation of the magnets in a PM motor, SmCo has more advantages. For the stator and rotor lamination, Hiperco50 is used to replace M270-35A lamination. The purpose of choosing different materials for lamination was to improve electromagnetic performance. To allow a motor to run safely at a higher temperature, the materials used to build it should be able to survive in high temperatures. Therefore, Hiperco50 was chosen as the lamination material for the stator and rotor, because it can withstand high temperatures up to 937 °C.

There are two types of winding for permanent magnet motor such as distributed- winding and concentrated-winding. Most interior PM motors are designed with distributed winding because this generally results in a more sinusoidal MMF distribution and EMF waveform. This type of winding has stator coils that span more than one tooth. Distributed winding is better than concentrated winding because it can offer higher peak electromagnetic torque with lower torque ripple. It can also provide a more reliable flux-weakening capability. Also, compared to concentrated winding, motors with distributed winding have lower power losses.

In this study, two types of concentrated winding (CW) have been implemented and analysed to find the most suitable winding for the motors designed. All motors have the same rotor topologies, the same material for the stator and rotor laminations, and they use the same type of permanent magnet material, neodymium-iron-boron. One motor was constructed with open slot CW, while another adopted semi-closed concentrated winding.

To validate the thermal modelling that has been applied, and the FEA output performance for the permanent magnet motor, two prototype machines were built. The first prototype machine, machine I, was built using the same material as the existing Nissan LEAF. M250-35A for stator and rotor lamination and neodymium-iron-boron for the rare-earth magnet. Meanwhile, the second machine, machine II, was developed with high-temperature material including Hiperco50 for the stator and rotor lamination and samarium-cobalt for the permanent magnet. The rotor and stator topologies for both machines are the same; however, machine II was designed to be smaller than machine I. Both machines adopted distributed winding for the stator coils. Testing was carried out to observe the thermal behaviour of the prototype machines. The testing was conducted with and without water cooling. Without the water-cooling, the temperature continued to rise and almost reached limits. However, when 10 litres/min water was pumped through the water jacket, the temperature after a certain time stopped rising and was maintained at the same level for about two hours.

8.1 Effects of size reduction

Three different scales of motor have been constructed and simulated. There were motor A, B, and C. The same materials as the existing Nissan LEAF were used for the designed motor. M270-35A was used for the rotor and stator lamination, while neodymium-iron-boron was used for the permanent magnet. When thermal modelling was applied to the motors, the temperature of some parts in the motor could be predicted. The smallest motor needed higher MMF, motor

C. As expected, the temperature at the coils for this machine was the highest at about 210°C. There are vast differences between them because the temperature at the coils in motor A and B stayed just below 150°C. The cost of the permanent magnet also has been presented. With the current value of NdFeB, the price for the permanent magnets is reduced by 19%.

8.2 Effect with a different permanent magnet material

The results of this study indicate that, with the same value of MMF, a motor that uses samarium cobalt as a rare-earth magnet shows lower flux density in the stator yoke and rotor laminations than a motor with neodymium-iron-boron. Three different sizes of the motor, motor A, B, and C, were analysed and the temperature was predicted. As a result, the motor with SmCo produced lower values of back-EMF and core loss. Therefore, a higher current was needed to achieve the required torque. Higher MMF means higher power losses, and especially copper losses. However, there is a reduction in iron loss due to the size of the motor becoming smaller. Since copper loss is the major type of loss in the motor; therefore, the total loss for a smaller motor is still higher.

8.3 Effects of using different lamination materials

Comparisons have been conducted of the electromagnetic performance of motors with M270-35A and with Hiperco50 as rotor and stator lamination. With the same parameters, the smallest motor, which was motor C with Hiperco50, needs less than the value of MMF that a motor with the existing stator and rotor lamination. It can be concluded that, by replacing M270-35A with Hiperco50, the flux density and back-EMF of the machine will be improved.

When thermal modelling was applied to motor C with Hiperco50 as stator and rotor lamination, the results show that the predicted temperature of the essential parts of the motor remained under 200°C. For other parts, such as rotor lamination, permanent magnet, and housing, the predicted temperatures still under limitation. This result means that motor C with Hiperco50 can run safely without failure. On the other hand, if the motor is using Hiperco50 as stator and rotor lamination, the parameters of the motor can be reduced to 10% of the original size, and, at the same time, the usage of the rare-earth magnet material can be decreased.

8.4 Effect of different winding configuration

Motor with concentrated winding needs a higher current to be applied compared to a motor with distributed winding to achieve the same output performance as required. However, when the concentrated winding was adopted, the consumption of copper decreased significantly. Motors with concentrated winding need higher MMF than machines with distributed winding. Two types of CW have been constructed, open slot and semi-closed. With the same current density, the motor with semi-closed slot winding can offer higher peak electromagnetic torque than the motor with open slot winding. The cogging torque for semi-closed winding is larger than the cogging torque for open slot winding.

It can be concluded that a careful evaluation of performance requirements is needed to select the best candidate for the winding to be used. The choice depends on the requirements of specific applications. If the key performance metric is to maximize motor efficiency during high-speed operation, the concentrated winding has the advantage compared with all other design configurations considered in this study. However, if minimising rotor core losses is considered to be a more important criterion in specific applications, the net advantage shifts to the distributed winding machine.

8.5 Performance comparison of the prototype machines

The testing results that have been conducted show that machines with high-temperature materials (machine II) had higher resistance than a machine with the same material with the existing one (the machine I). The machine II was wound with 62 turns per slot while machine I was wound with 50 turns per slot. Meanwhile, the value of the inductance for the machine I was higher than that of machine II. The static torque for both machines shows good agreement between the simulation results and measured values. As expected, machine II needed higher MMF since it used samarium cobalt as magnet material and was smaller than machine I. Therefore, to achieve the same torque output, machine B needs an MMF value approximately to 66% more than that of the machine I.

A comparison was also conducted of the predicted temperature using thermal modelling (FEA) and the temperature measured on the prototype machine using thermocouples interfaced with a data logger. The expected temperature from the simulation was higher than the measured value. One of the reasons for this was the locations of that the thermocouples in the prototype machine did not precisely correspond with the thermal model using FEA. The initial temperature for the

Nissan LEAF is 65°C. Therefore, the simulation temperature a bit higher because it started from 65°C. The hottest part was at the end-winding due to stator copper losses, which depend on the stator current. The coldest part was at the shaft.

The stator winding for the machine I was injected with 7 amps to produce a value of torque of 16.2 Nm. With 10 litres/min flow rate of water coolant, the temperature at the end-winding remained below 120°C. To achieve the same torque output, 12.5 amps were injected at the stator winding of machine II. With the same flow rate of coolant applied, the temperature at the end-winding remained below 160°C. It can be concluded that the water coolant is significant for this machine and changes its thermal behaviour, especially at the end-winding. As mentioned in the previous chapter, due to technical problems, Magnetemp Y-240 was chosen as the winding to replace Kulgrid HT Magnet wire that can stand temperatures up to 537°C. Therefore, the temperature limit for the end-winding was 240°C. Testing for higher current could not be set up for safety reasons. Therefore, FEA was conducted to predict the temperature for machine II with 20 amps injected into the stator winding. The output torque was 30 Nm. From the simulation results, the predicted temperature at the end-winding was 230°C while it was 180°C at the permanent magnet. If suitable coils were wound on the stator, the machine could run safely without failure at the stator winding, and no demagnetisation would occur in the permanent magnet.

8.6 Recommendations for future research

Based on the result of the analysis of the small high-temperature permanent magnet motor that has been designed and built, work can be done in the future to improve the performance of the motor.

8.6.1 Rotor and stator topologies

To improve electromagnetic performance and thermal behaviour, research should focus more on the permanent magnet machine with concentrated winding rather than distributed winding. Suitable combinations of poles and slots need to be investigated to achieve the maximum output performance required. Since core loss is the significant losses in permanent magnet motor; therefore, it is crucial to find an alternative to reduce the core loss to make sure the temperature rise at the coils is reduced. Apart from that, thermal modelling needs to be applied to the machine to predict the temperature rise in the essential parts of the machine. As found here, the

concentrated winding produced lower copper losses than the distributed winding; therefore, the temperature rise should be lower too.

Applying other rotor topologies would also be one of the methods to reduce the usage of the permanent magnet. Besides that, it is possible to design a segmented magnet to reduce the eddy current loss produced in a permanent magnet. Different permanent magnet arrangements will provide different values of flux density. A study should be conducted on a few permanent magnet arrangements to find the most suitable arrangement to get the required output performance. Besides choosing samarium-cobalt to replace neodymium-iron-boron, other types of permanent magnet such as alnico and ceramics can also be considered depending on the requirements of specific applications of the machine.

8.6.2 Possible Emerging High-Temperature Materials

To make sure that a motor can run safely at high temperatures without failure, the materials used to develop the motor must be in the category of high-temperature materials, especially for the coils. It was challenging to find suitable coil available for the motor that has been designed in this study. To overcome this problem, an appropriate diameter of wire should be chosen first, and then the motor could be redesigned according to this diameter. Apart from that, high-temperature wires and their insulating coating must be thermally stable at high temperatures and be mechanically reliable yet flexible for handling. Inorganic materials such as glasses and ceramics are useful at higher temperatures but lack the mechanical performance required by the coil winding process. Therefore, new kinds of composite materials containing inorganic-organic nano-hybrids, and particulate ceramics, have been proposed [2]. The characterisation of coated wires by way of bend, dielectric strength and thermal resistance tests have shown that this type of tailored insulation coating can be used in service temperatures up to 500°C. Besides that, coils based on a wire insulated by a thin ceramic coating protected by a high temperature could be an alternative choice to fulfil the functions required by a permanent magnet machine able to work permanently at a high internal temperature [88].

8.6.3 Improve the cooling method

The water jacket is the most popular cooling method. However, there is another option of a cooling method that can be applied to the motor, as mention in Chapter 2, to determine the most

efficient one, such as spray and evaporative cooling. Instead of water as a coolant, other fluids can be used as a coolant. Apart from that, the cooling method also can be improved by applying appropriate design techniques and choose suitable materials.

References:

- [1] N. Gaurav and C. K. Narayan, "A survey and comparison of characteristics of motor drives used in electric vehicles," in *Electrical and Computer Engineering, 2006. CCECE '06. Canadian Conference on*, 2006, pp. 811-814.
- [2] C. C. Chan, K. T. Chau, J. Z. Jiang, W. Xia, M. Zhu, and R. Zhang, "Novel permanent magnet motor drives for electric vehicles," *Industrial Electronics, IEEE Transactions on*, vol. 43, pp. 331-339, 1996.
- [3] W. L. Soong, S. Han, and T. M. Jahns, "Design of interior PM machines for field-weakening applications," in *Electrical Machines and Systems*, Seoul, Korea, 2007.
- [4] X. Yinglei, L. Qunzhan, Z. Liyan, and M. Qingan, "Development of permanent magnet synchronous motor for electric vehicle," in *Sustainable Power Generation and Supply, 2009. SUPERGEN '09. International Conference on*, 2009, pp. 1-5.
- [5] D. Fodorean and A. Miraoui, "Permanent magnets thermal operation limits in a hybrid excited synchronous machine used on wide speed applications," in *Optimization of Electrical and Electronic Equipment, 2008. OPTIM 2008. 11th International Conference on*, 2008, pp. 21-26.
- [6] Z. Wu and G. J. Su, "High-performance permanent magnet machine drive for electric vehicle applications using a current source inverter," presented at the IEEE, 2008.
- [7] A. Kumar, S. Marwaha, A. Singh, and A. Marwaha, "Performance investigation of a permanent magnet generator," *Simulation Modelling Practice and Theory* 17, pp. 1548-1554, 2009.
- [8] T. Shizanto, S. Arakawa, H. Oyama, H. Saka, and T. Hayasaki, "Development of high temperature superconducting motor for automobiles," ed: SEI Technical Review, 2012.
- [9] N. Mohan, *Electric machines and drives*. USA: Wiley, 2012.
- [10] X. D. Xue, K. W. E. Cheng, and N. C. Cheung, "Selection of electric motor for electric vehicles," in *Australasian Universities Power Engineering Conference (AUPEC'08)*, 2008.
- [11] R. Madhavan and B. G. Fernandes, "A novel axial flux segmented SRM for electric vehicle application," in *Electrical Machines (ICEM), 2010 XIX International Conference on*, 2010, pp. 1-6.
- [12] K. Taechyung, L. Hyung-Woo, and M. Ehsani, "High performance brushless permanent magnet motor/generator drives in electric and hybrid electric vehicles," in *Power Electronics Specialists Conference, 2006. PESC '06. 37th IEEE*, 2006, pp. 1-5.
- [13] I. Edward, S. Wahsh, and M. a. Badr, "Analysis of PMSM drives for electric vehicles," in *SICE '98. Proceedings of the 37th SICE Annual Conference. International Session Papers*, 1998, pp. 979-984.
- [14] N. Schofield and C. Giraud-Audine, "Design procedure for brushless PM traction machines for electric vehicle applications," in *Electric Machines and Drives, 2005 IEEE International Conference on*, 2005, pp. 1788-1792.
- [15] S. I. Y. Sato, T. Okubo, M. Abe, and K. Tamai, "Development of high response motor and inverter system for the nissan LEAF electric vehicle," in *SAE International*, 2011.
- [16] https://estore.ricardo.com/wp-content/uploads/2015/11/2014MY-BMW-i3-Benchmarking-Overview_-v1.2-PREVIEW.pdf
- [17] https://estore.ricardo.com/wp-content/uploads/2015/09/Tesla-Model-S-60_Benchmarking-Overview_v2-Preview.pdf.
- [18] www.ornl.gov.
- [19] T. Gund, "Design of permanent magnet machine with different rotor type," presented at the World Academy of Science, Engineering and Technology, 2010.
- [20] R. Krishnan, *Permanent Magnet Synchronous and Brushless DC Motor Drives*. Blacksburg, Virginia, USA: CRC Press, 2010.

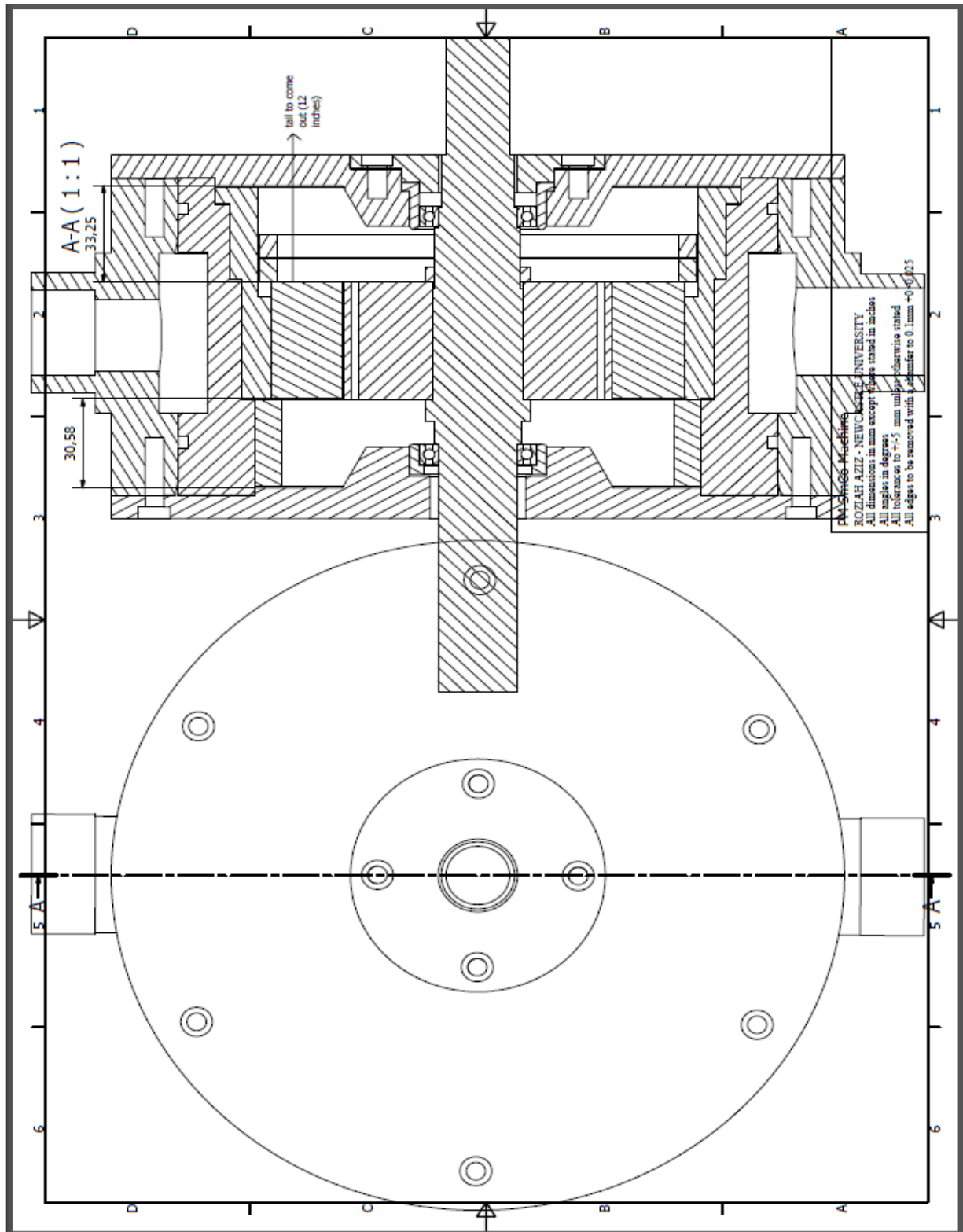
-
- [21] P. Zheng, S. Yu, J. Bai, and Y. Sui, "Design and analysis of compound-structure permanent magnet synchronous machine used for hybrid electric vehicles," presented at the First International Conference on Pervasive Computing, Signal Processing and Applications, 2010.
 - [22] Y. Liu, C. Tong, R. Liu, J. Zhao, J. Bai, and P. Zheng, "Comprehensive research on compound-structure permanent magnet synchronous machine system used for HEVs," presented at the First International Conference on Pervasive Computing, Signal Processing and Applications, 2010.
 - [23] L. N. Tulelea, S. I. Deaconu, I. Boldea, and F. Marigretti, "Design and control of single stator dual PM rotor axial synchronous machine for hybrid electric vehicles," in *12th International Conference and Optimization of Electrical and Electronic Equipment Romania*, 2010.
 - [24] J. Goss, D. Staton, R. Wrobel, and P. Mellor, "Brushless AC interior-permanent magnet motor design: Comparison of slot/pole combinations and distributed vs. concentrated windings," in *Energy Conversion Congress and Exposition (ECCE), 2013 IEEE*, 2013, pp. 1213-1219.
 - [25] L. Jae Jun, K. Won Ho, Y. Jin Seung, Y. Si Yeong, K. Sang Min, L. Jin Ju, *et al.*, "Comparison between concentrated and distributed winding in IPMSM for traction application," in *Electrical Machines and Systems (ICEMS), 2010 International Conference on*, 2010, pp. 1172-1174.
 - [26] J. K. Tangudu and T. M. Jahns, "Comparison of interior PM machines with concentrated and distributed stator windings for traction applications," in *Vehicle Power and Propulsion Conference (VPPC), 2011 IEEE*, 2011, pp. 1-8.
 - [27] O. K. Soon, K. Sung-Il, Z. Peng, and H. Jung-Pyo, "Performance comparison of IPMSM with distributed and concentrated windings," in *Industry Applications Conference, 2006. 41st IAS Annual Meeting. Conference Record of the 2006 IEEE*, 2006, pp. 1984-1988.
 - [28] A. R. Munoz, F. Liang, and M. W. Degner, "Evaluation of Interior PM and Surface PM Synchronous machines with distributed and concentrated windings," in *Industrial Electronics, 2008. IECON 2008. 34th Annual Conference of IEEE*, 2008, pp. 1189-1193.
 - [29] W. Aimeng, W. Chunmei, and W. L. Soong, "Design and optimization of interior PM machines with distributed and fractional-slot concentrated-windings for hybrid electric vehicles," in *Transportation Electrification Asia-Pacific (ITEC Asia-Pacific), 2014 IEEE Conference and Expo*, 2014, pp. 1-5.
 - [30] L. Chong, R. Dutta, and M. F. Rahman, "Performance comparison between concentrated and distributed wound IPM machines used for field weakening applications," in *Electrical Machines and Power Electronics and 2011 Electromotion Joint Conference (ACEMP), 2011 International Aegean Conference on*, 2011, pp. 616-619.
 - [31] W. Aimeng, W. Chunmei, and W. Yi, "Performance analysis and comparison of interior permanent magnet machine with FSCW and distributed windings for a hybrid electric vehicle," in *Electrical Machines and Systems (ICEMS), 2013 International Conference on*, 2013, pp. 1044-1047.
 - [32] Z. Deming, Q. Xin, Z. Nan, and Y. Yangguang, "A comparative study of winding factors between distributed windings and non-overlapping concentrated windings," in *Electric Utility Deregulation and Restructuring and Power Technologies, 2008. DRPT 2008. Third International Conference on*, 2008, pp. 2725-2729.
 - [33] A. B. A. Ali, "Low speed permanent magnet synchronous motor comparison - concentrated and distributed winding," *Jahresbericht*, 2006.
 - [34] A. Rasekh, P. Sergeant, and J. Vierendeels, "Convective heat transfer prediction in disk-type electrical machines," *Applied Thermal Engineering*, vol. 91, pp. 778-790, 2015.
 - [35] H. VuXuan, D. Lahaye, S. O. Ani, H. Polinder, and J. A. Ferreira, "Effect of design parameters on electromagnetic torque of PM machines with concentrated windings using nonlinear dynamic FEM," in *Electric Machines & Drives Conference (IEMDC), 2011 IEEE International*, 2011, pp. 383-388.
-

-
- [36] K. Nakamura, J. Yoshida, and O. Ichinokura, "A novel high power permanent magnet reluctance generator using ferrite magnet," in *Power Electronics and Applications, 2009. EPE '09. 13th European Conference on*, 2009, pp. 1-8.
 - [37] T. Miura, S. Chino, M. Takemoto, S. Ogasawara, A. Chiba, and N. Hoshi, "A ferrite permanent magnet axial gap motor with segmented rotor structure for the next generation hybrid vehicle," in *Electrical Machines (ICEM), 2010 XIX International Conference on*, 2010, pp. 1-6.
 - [38] W. Aimeng, L. Heming, and L. Cheng-Tsung, "On the material and temperature impacts of interior permanent magnet machine for electric vehicle applications," *Magnetics, IEEE Transactions on*, vol. 44, pp. 4329-4332, 2008.
 - [39] N. A. Demerdash, T. A. Nyamusa, and T. W. Nehl, "Comparison of effects of overload on parameters and performance of samarium-cobalt and strontium-ferrite radially oriented permanent magnet brushless dc motors," *Power Apparatus and Systems, IEEE Transactions on*, vol. PAS-104, pp. 2223-2231, 1985.
 - [40] S. K. Pal, "Comparative study of the design and development of direct drive brushed and brushless DC motors with samarium cobalt, neodymium-iron-boron and ceramic magnets," in *Permanent Magnet Machines and Drives, IEE Colloquium on*, 1993, pp. 7/1-7/7.
 - [41] A. R. Tariq, C. E. Nino-Baron, and E. G. Strangas, "Consideration of magnet materials in the design of PMSMs for HEVs application," in *Power and Energy Society General Meeting, 2011 IEEE*, 2011, pp. 1-6.
 - [42] N. Bianchi, D. Durello, and A. Fasolo, "Relationship between rotor losses and size of permanent magnet machines," in *Diagnostics for Electric Machines, Power Electronics & Drives (SDEMPED), 2011 IEEE International Symposium on*, 2011, pp. 251-257.
 - [43] A. Williams. (2009) Permanent Magnets for High Temperature Applications. *Magnews*.
 - [44] K. Dinga. (2014, The Rare Earth Magnet Industry and Rare Earth Price in China. Available: <http://www.epi-conferences.org> or <http://dx.doi.org/10.1051/epiconf/20147504005>
 - [45] J. M. D. Coey, "Perspective and Prospects for Rare Earth Permanent Magnets," *Engineering*, 2018.
 - [46] <https://www.statista.com/statistics/450152/global-reo-neodymium-oxide-price-forecast/>.
 - [47] A. M. Technologies. *Neodymium-iron-boron magnet catalogs- N42M*. Available: http://www.arnoldmagnetics.com/Neodymium_Literature.aspx
 - [48] A. M. Technologies. *Samarium cobalt magnet catalogs-Recoma 33E*. Available: http://www.arnoldmagnetics.com/uploadedFiles/Arnold_DS_RECOM.pdf
 - [49] C. Ruschetti, C. Verucchi, G. Bossio, C. De Angelo, and G. García, "Rotor demagnetization effects on permanent magnet synchronous machines," *Energy Conversion and Management*, vol. 74, pp. 1-8, 2013.
 - [50] L. M. T. Seong Taek Lee, "Analytical Method of Torque Calculation for Interior Permanent Magnet Synchronous Machine."
 - [51] K. Yamazaki, "Torque and Efficiency Calculation of an Interior Permanent Magnet Motor Considering Harmonic Iron Losses of Both the Stator and Rotor," presented at the IEEE Transaction on Magnetics, 2002.
 - [52] P. C. K. L. W. Fei, "Torque Ripple Reduction of Axial Flux Permanent Magnet Synchronous Machine with Segmented and Laminated Stator," 2009.
 - [53] P. P. Peter Vrtic, Miralem Hadziselimovic, Tine Marcic and Bojan Stumberger, "Torque Analysis of an Axial Flux Permanent Magnet Synchronous Machine by Using Analytical Magnetic Field Calculation," 2009.
 - [54] G. Cvetkovski and L. Petkovska, "Performance Improvement of PM Synchronous Motor by Using Soft Magnetic Composite Material," *Magnetics, IEEE Transactions on*, vol. 44, pp. 3812-3815, 2008.
 - [55] A. M. I. J. A. Guemes, M. P. Donsion and J. I. Del Hoyo, "Analysis of Torque in Permanent Magnet Synchronous Motors with Fractional Slot Windings," presented at the International Conference on Electrical Machines, 2008.
-

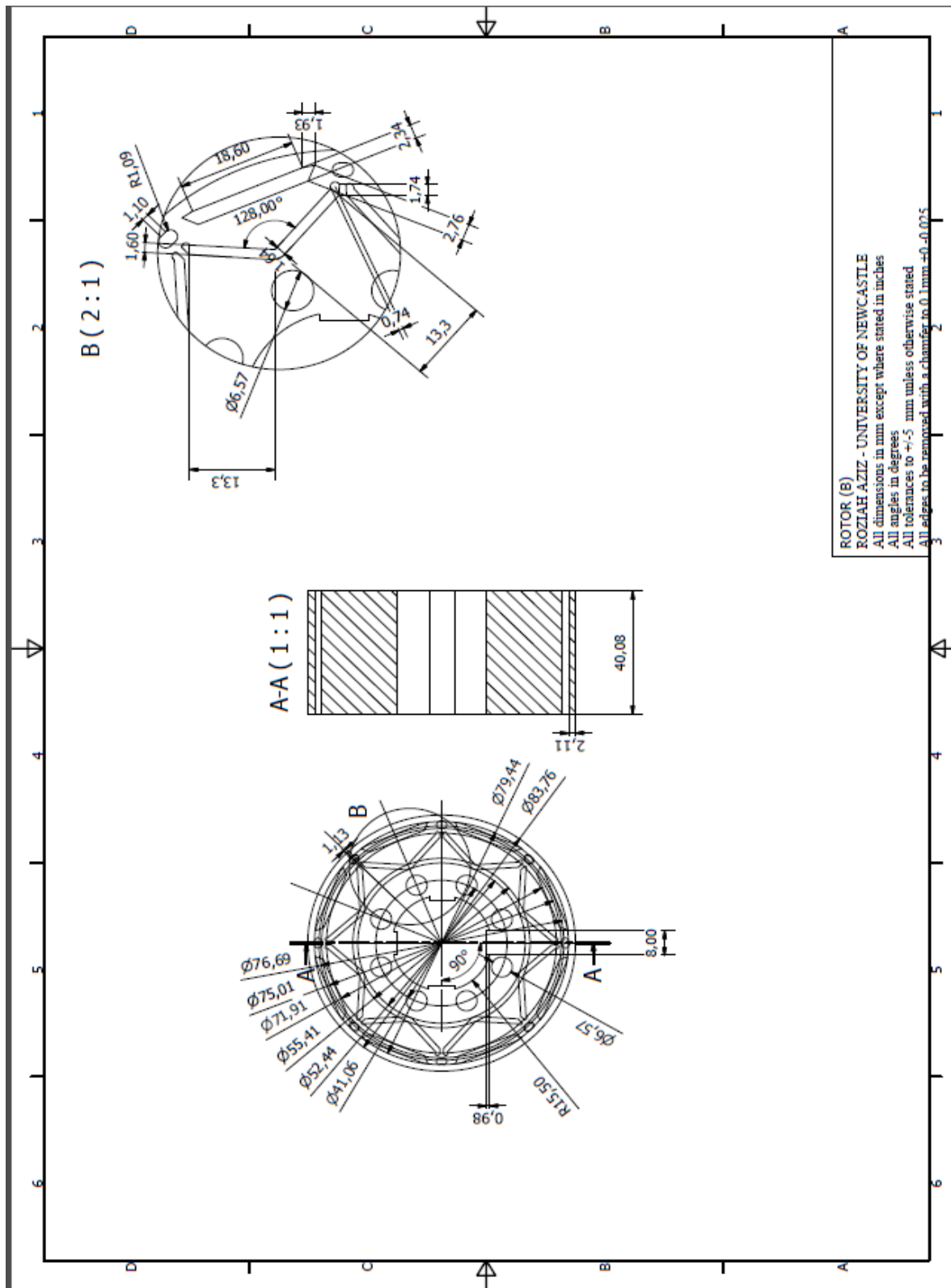
-
- [56] P. S. H. Jussila, J. Pyrhonen, "Losses of a Permanent Magnet Synchronous Motor with Concentrated Winding," 2010.
 - [57] L. Z. Co Huynh, Dipjyoti Acharya, "Losses in High Speed Permanent Magnet Machines Used in Microturbine Applications," *Journal of Engineering for Gas Turbine and Power*, 2008.
 - [58] S. M. Sharkh, A. A. Qazalbash, N. T. Irenji, and R. G. Wills, "Effect of slot configuration and airgap and magnet thicknesses on rotor electromagnetic loss in surface PM synchronous machines," in *Electrical Machines and Systems (ICEMS), 2011 International Conference on*, 2011, pp. 1-6.
 - [59] C. J. T. Bauml, C. Kral, "An Innovative Parametrization Method for a Thermal Equivalent Circuit Model of an Interior Permanent Magnet Synchronous Machine."
 - [60] J. Seok-Myeong, C. Jang-Young, K. Kyoung-Jin, K. Il-Jung, and S. Ho-Kyung, "Performance analysis of permanent magnet machines considering magnetic losses based on analytical parameter estimation," in *Electrical Machines and Systems, 2008. ICEMS 2008. International Conference on*, 2008, pp. 3152-3157.
 - [61] M. Tursini, M. Villani, G. Fabri, and L. Di Leonardo, "A switched-reluctance motor for aerospace application: Design, analysis and results," *Electric Power Systems Research*, vol. 142, pp. 74-83, 2017/01/01/ 2017.
 - [62] K.-H. Lee, H.-R. Cha, and Y.-B. Kim, "Development of an interior permanent magnet motor through rotor cooling for electric vehicles," *Applied Thermal Engineering*, vol. 95, pp. 348-356, 2016/02/25/ 2016.
 - [63] N. Y. Roopnarine, NY (US), "Motor for high temperature applications," US Patent, 2013.
 - [64] R. Savino, L. Criscuolo, G. D. Di Martino, and S. Mungiguerra, "Aero-thermo-chemical characterization of ultra-high-temperature ceramics for aerospace applications," *Journal of the European Ceramic Society*, 2017/12/24/ 2017.
 - [65] S. Tang and C. Hu, "Design, Preparation and Properties of Carbon Fiber Reinforced Ultra-High Temperature Ceramic Composites for Aerospace Applications: A Review," *Journal of Materials Science & Technology*, vol. 33, pp. 117-130, 2017/02/01/ 2017.
 - [66] H. Su, H. Wen, X. Zheng, and J. Su, "Development of a Super High Efficiency Motor with Boron Aluminum Alloy Rotor," *Procedia Engineering*, vol. 174, pp. 1221-1228, 2017/01/01/ 2017.
 - [67] B. Hannon, P. Sergeant, and L. Dupré, "Torque and torque components in high-speed permanent-magnet synchronous machines with a shielding cylinder," *Mathematics and Computers in Simulation*.
 - [68] J. Pyrhonen, P. Lindh, M. Polikarpova, E. Kurvinen, and V. Naumanen, "Heat-transfer improvement in an axial-flux permanent-magnet synchronous machine," *Applied Thermal Engineering*, vol. 76, pp. 245-251, 2015.
 - [69] M. Polikarpova, P. Lindh, C. Gerada, M. Rilla, V. Naumanen, and J. Pyrhönen, "Thermal effects of stator potting in an axial-flux permanent magnet synchronous generator," *Applied Thermal Engineering*, vol. 75, pp. 421-429, 2015.
 - [70] D. A. Howey, P. R. N. Childs, and A. S. Holmes, "Air-gap convection in rotating electrical machines," *IEEE Transactions on Industrial Electronics*, vol. 59, pp. 1367-1375, 2012.
 - [71] G.F. Rogers and Y. R. Mayhew, *Engineering Thermodynamics Work and Heat Transfer*. Bristol: Longmans, 1959.
 - [72] P. Ponomarev, M. Polikarpova, and J. Pyrhonen, "Thermal modeling of directly-oil-cooled permanent magnet synchronous machine," in *Electrical Machines (ICEM), 2012 XXth International Conference on*, 2012, pp. 1882-1887.
 - [73] F. Jinxin, Z. Chengning, W. Zhifu, and E. G. Strangas, "Thermal analysis of water cooled surface mount permanent magnet electric motor for electric vehicle," in *Electrical Machines and Systems (ICEMS), 2010 International Conference on*, 2010, pp. 1024-1028.
 - [74] E. Odvarka, N. L. Brown, A. Mebarki, M. Shanel, S. Narayanan, and C. Ondrusek, "Thermal modelling of water-cooled axial flux permanent magnet machine," in *Power Electronics, Machines and Drives (PEMD 2010), 5th IET International Conference*, 2010.
-

-
- [75] X. Zhang, H. Wang, G. Zhang, and G. Gu, "Temperature characteristics in the stator model of a permanent magnet motor by water-cooling and evaporative cooling," in *2005 International Conference on Electrical Machines and Systems*, 2005, pp. 2408-2410 Vol. 3.
- [76] M. A. Fakhfakh, M. H. Kasem, S. Tounsi, and R. Neji, "Thermal analysis of permanent magnet synchronous motor for electric vehicles," *Journal of Asian Electric Vehicles*, 2008.
- [77] W. Li, J. Wang, X. Zhang, and B. Kou, "Loss calculation and thermal simulation analysis of high-speed PM synchronous generators with rotor topology," in *Computer Application and System Modeling (ICCASM), 2010 International Conference on*, 2010, pp. V14-612-V14-616.
- [78] S. Nategh, A. Krings, H. Zhe, O. Wallmark, M. Leksell, and M. Lindenmo, "Evaluation of stator and rotor lamination materials for thermal management of a PMaSRM," in *Electrical Machines (ICEM), 2012 XXth International Conference on*, 2012, pp. 1309-1314.
- [79] A. M. Gazdac, A. M. Mabwe, F. Betin, C. S. Martis, and K. Biro, "Investigation on the thermal behavior of the dual-rotor Permanent Magnet Induction Machine," in *IECON 2012 - 38th Annual Conference on IEEE Industrial Electronics Society*, 2012, pp. 1858-1863.
- [80] Z. Nannan, Z. Q. Zhu, and L. Weiguo, "Thermal analysis and comparison of permanent magnet motor and generator," in *Electrical Machines and Systems (ICEMS), 2011 International Conference on*, 2011, pp. 1-5.
- [81] X. Wang and L. Tiecai, "A 3-D Electromagnetic Thermal Coupled Analysis of Permanent Magnet Brushless DC Motor," in *Instrumentation, Measurement, Computer, Communication and Control, 2011 First International Conference on*, 2011, pp. 15-18.
- [82] N. Y. Roopnarine, US, "Motor for High Temperature Applications," US Patent, 2013.
- [83] J. F. Gieras, *Advancements in electric machine*. United States of America: Springer, 2008.
- [84] <http://www.ceramawire.com/technical-information/ceramaTechspec.pdf>.
- [85] <https://www.sterlingwires.net/enameled-copper-wires.html>.
- [86] <https://essexwire.com/products/magnetemp-y-240/>.
- [87] <https://essexwire.com/magnet-wire-global/ultrashield-plus/>.
- [88] V. Iosif, D. Roger, S. Duchesne, and D. Malec, "An insulation solution for coils of high temperature motors (500 degC)," in *2016 IEEE International Conference on Dielectrics (ICD)*, 2016, pp. 297-300.
-

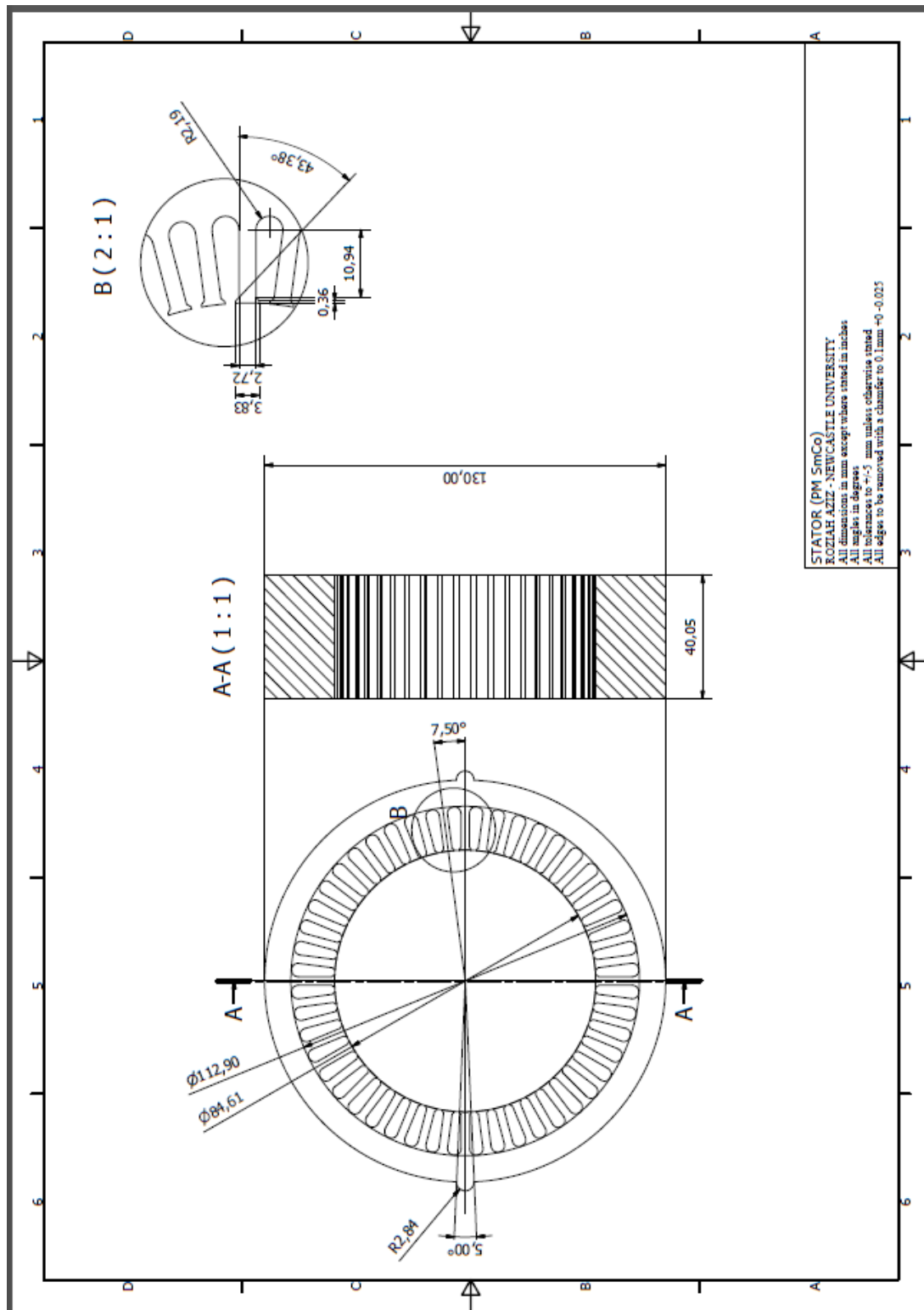
Appendix 1 PM machine drawings



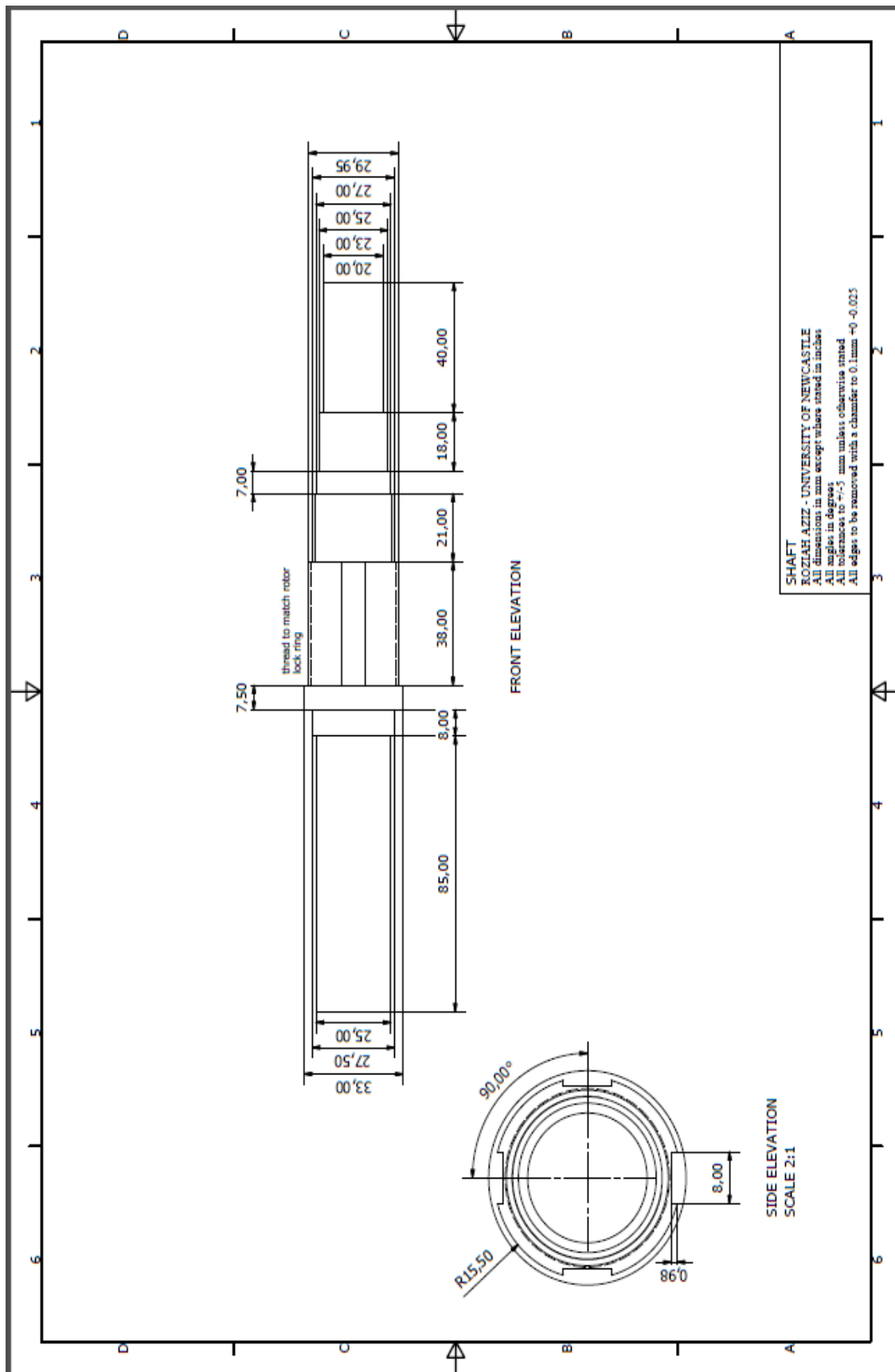
Full machine



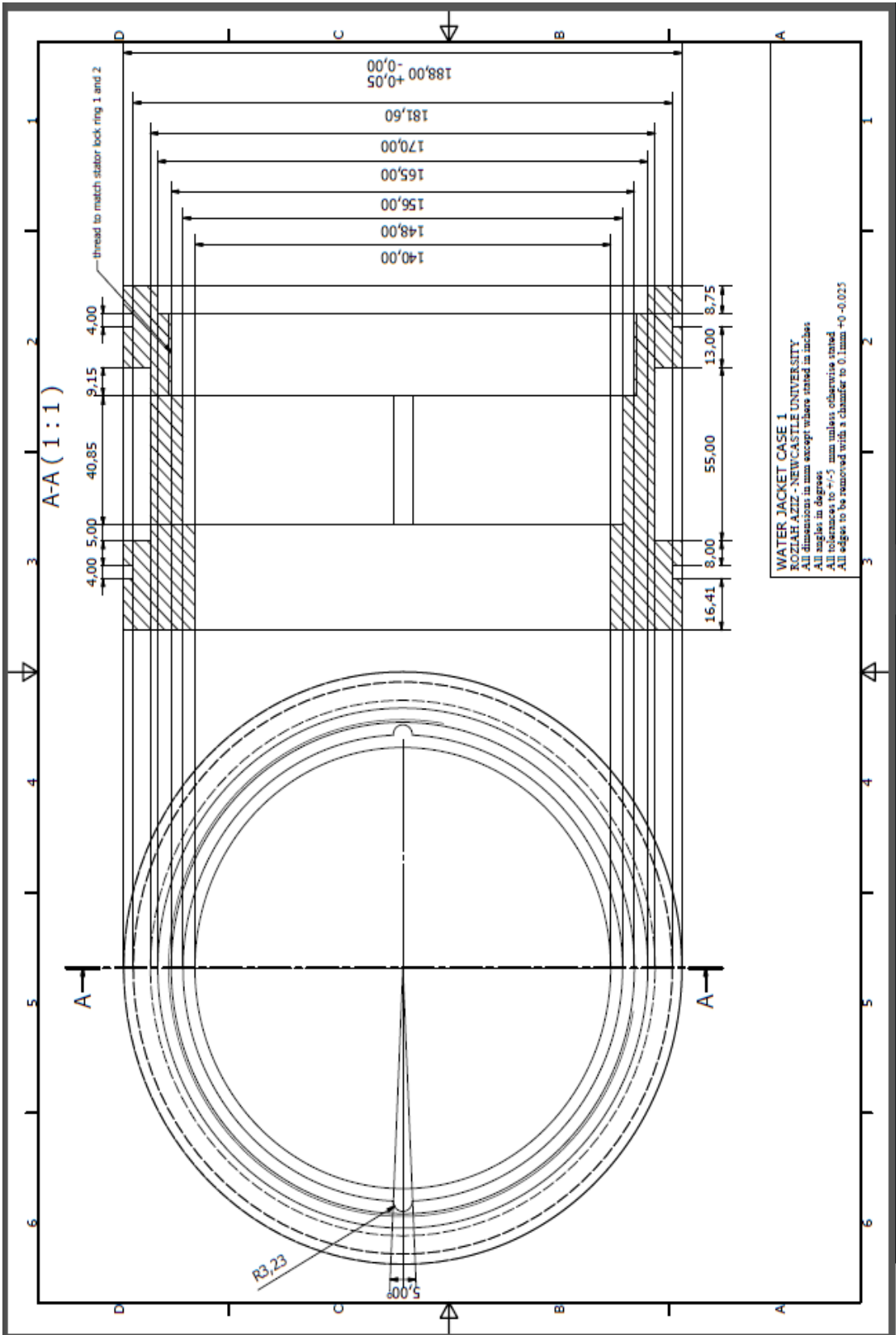
Rotor



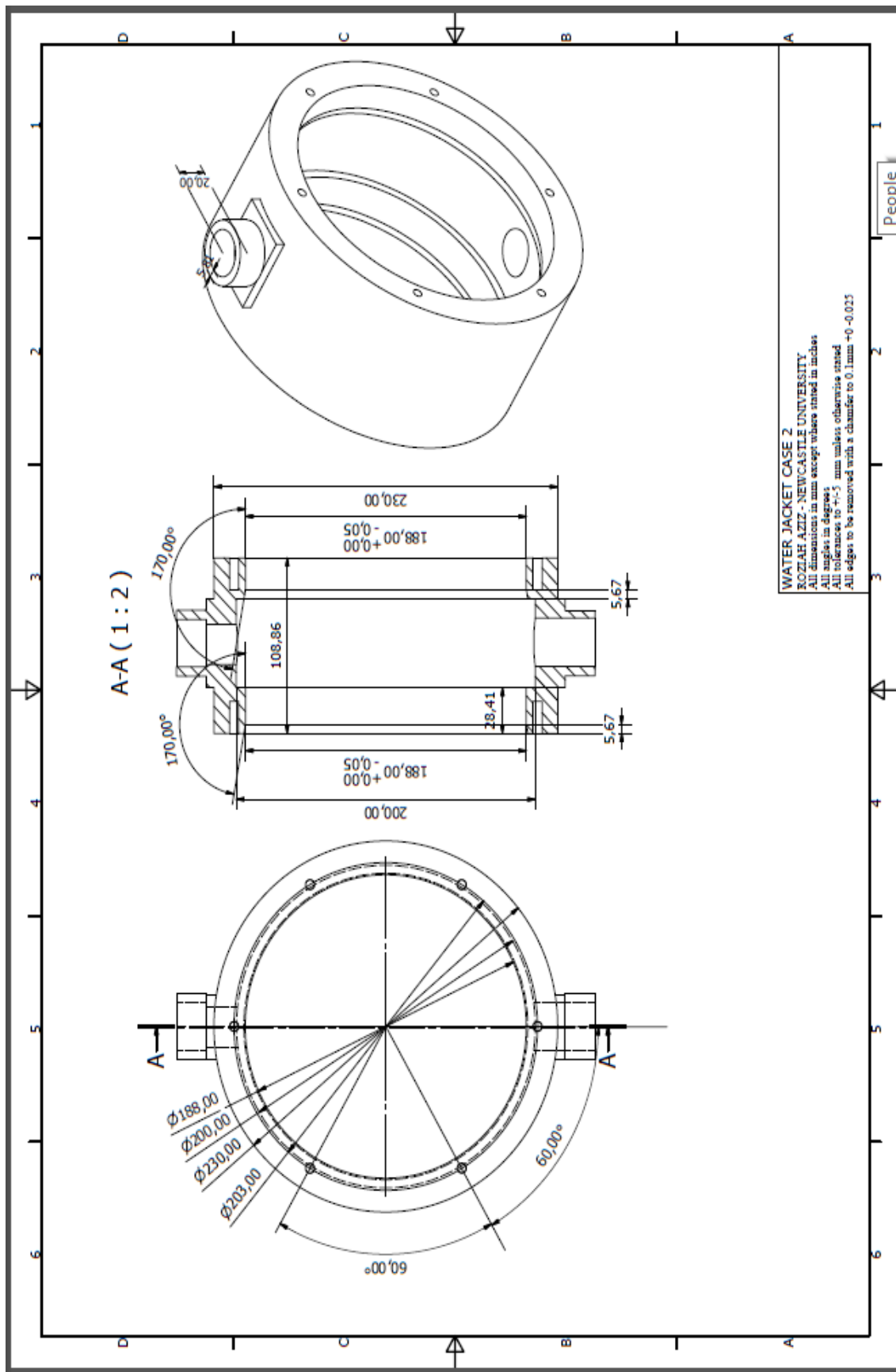
Stator



Shaft



Water Jacket Case 1



Water jacket case 2